

# Analysis of a three degree-of-freedom parallel mechanism

by

Juan Antonio Carretero G.

B. Eng., National University of Mexico (UNAM), 1996


A Thesis Submitted in Partial Fulfillment of the  
Requirements for the Degree of


MASTER OF APPLIED SCIENCE


in the Department of Mechanical Engineering.

We accept this thesis as conforming  
to the required standard

  
Dr. M. Nahon, Co-supervisor (Dept. of Mechanical Engineering)

  
Dr. R. Podhorodeski, Co-supervisor (Dept. of Mechanical Engineering)

  
Dr. W.-S. Lu, Outside Member (Dept. of Electrical and Computer Engineering)

  
D.M. Lokhorst, M.A.Sc., External Examiner (President, RSI Technologies)

© JUAN ANTONIO CARRETERO G., 1998  
University of Victoria

All rights reserved. This thesis may not be reproduced in whole or in part, by  
photocopy or other means, without permission of the author.

Co-supervisors: Dr. M. Nahon and Dr. R. Podhorodeski

## Abstract

A study of the kinematic characteristics of a three degree-of-freedom (dof) parallel mechanism is presented. The architecture of the mechanism is described. The inverse displacement and inverse velocity solutions are obtained. Since the mechanism has only three dof, constraint equations describing the inter-relationship between the six motion coordinates are derived. These constraints allow the definition of parasitic motions, i.e., motions in the three unspecified motion coordinates. When incorporated into the kinematics model, the constraints allow a constrained Jacobian matrix to be obtained. A dexterity analysis is undertaken, and an analysis of the dexterous workspace of the mechanism is also reported. Architecture optimization of the device is undertaken demonstrating that specific values of design variables allow minimization of parasitic motion and optimization of dexterity. Finally, static force solutions are formulated to allow required actuator and structural forces to be determined.

Examiners:

[Redacted]

---

Dr. M. Nahon, Co-supervisor (Dept. of Mechanical Engineering)

[Redacted]

---

Dr. R. Podhorodeski, Co-supervisor (Dept. of Mechanical Engineering)

[Redacted]

---

Dr. W.-S. Lu, Outside Member (Dept. of Electrical and Computer Engineering)

[Redacted]

---

D. M. Lokhorst, M.A.Sc., External Examiner (President, RSI Technologies)

# Table of Contents

Abstract	ii
Table of Contents	iii
List of Figures	vi
List of Tables	viii
Dedication	ix
Acknowledgements	x
<b>1 Introduction</b>	<b>1</b>
1.1 Telescope image correction . . . . .	1
1.2 Literature review . . . . .	3
1.2.1 Parallel mechanism design . . . . .	3
1.2.2 Reduced degree-of-freedom designs . . . . .	5
1.2.3 Architecture optimization . . . . .	7
1.2.4 Static force analysis . . . . .	8
1.3 Description of the mechanism . . . . .	8
1.3.1 Kinematic layout . . . . .	8
1.3.2 Potential applications . . . . .	11
1.3.3 Exploiting the mechanical advantage near an all-branch-singular configuration . . . . .	11
<b>2 Kinematic analysis</b>	<b>13</b>
2.1 Inverse kinematics . . . . .	13
2.1.1 Inverse Displacement Solution (IDS) . . . . .	13
2.1.2 Constraint equations . . . . .	18
2.1.3 Inverse Velocity Solution (IVS) . . . . .	21
2.1.4 Coupling of the constraint equations to the Jacobian matrix . . . . .	22
2.2 Forward kinematics . . . . .	24

2.3	Parasitic motion . . . . .	25
2.3.1	Definitions . . . . .	25
2.3.2	Algorithm . . . . .	26
2.3.3	Example results . . . . .	26
2.3.4	Behaviour of the parasitic motions . . . . .	28
<b>3</b>	<b>Dexterity analysis</b>	<b>32</b>
3.1	Definitions . . . . .	32
3.2	$\psi$ and $\theta$ mappings . . . . .	34
3.2.1	Algorithm . . . . .	34
3.2.2	Example results . . . . .	34
3.3	Frame and scale dependency . . . . .	36
3.4	Behaviour of $\text{cond}(\mathbf{J}')$ . . . . .	36
3.5	Dexterous workspace . . . . .	38
3.5.1	Definitions . . . . .	38
3.5.2	Algorithm . . . . .	40
3.5.3	Examples . . . . .	43
3.5.4	Discussion of results . . . . .	43
3.6	Singular values analysis . . . . .	47
<b>4</b>	<b>Optimization</b>	<b>54</b>
4.1	Goals of the optimization . . . . .	54
4.2	Available variables . . . . .	54
4.3	Available functions . . . . .	56
4.3.1	Parasitic Motion . . . . .	56
4.3.2	Dexterity . . . . .	59
4.4	Optimization methods and procedures . . . . .	60
4.5	Graphical method results . . . . .	60
4.6	Numerical method results . . . . .	67
4.6.1	Parasitic Motion . . . . .	67
4.6.2	Dexterity . . . . .	71
<b>5</b>	<b>Static Force Analysis</b>	<b>74</b>
5.1	Definitions . . . . .	74
5.2	Solution of the joint forces through power considerations . . . . .	75
5.3	Solution of the joint and structural forces via screw formulation . . . . .	77
5.3.1	Obtaining the associated reciprocal screws . . . . .	82
5.3.2	Expressing the screw quantities in the inertial frame . . . . .	83
5.3.3	Solving the inverse force problem . . . . .	85
5.4	Solution of the joint and structural forces . . . . .	86
5.4.1	Algorithm . . . . .	86

5.4.2	Sample results and comparison . . . . .	87
5.5	Stiffness analysis . . . . .	89
<b>6</b>	<b>Conclusions</b>	<b>93</b>
6.1	Kinematic analysis . . . . .	93
6.2	Parasitic motion analysis . . . . .	94
6.3	Dexterity and Dexterous workspace analysis . . . . .	94
6.4	Optimization . . . . .	95
6.5	Static force analysis . . . . .	96
6.6	Future work . . . . .	97
<b>A</b>	<b>Jacobian Matrix</b>	<b>98</b>
<b>B</b>	<b>Constraints Matrix</b>	<b>101</b>
	<b>References</b>	<b>103</b>

# List of Figures

1.1	Cassegrain type optical telescope ( <i>California Association for Research in Astronomy</i> ). . . . .	2
1.2	Secondary mirror motion directions . . . . .	4
1.3	Manipulator topologies: a) serial kinematic chain and b) parallel kinematic chain (the basic layout of the Gough-Stewart platform). . . . .	6
1.4	Proposed architecture: the HVRam mechanism. . . . .	10
2.1	Vector representation one kinematic chain (leg). . . . .	15
2.2	Ratio of actuator to platform velocity <i>vs.</i> $z$ position of the upper platform ( $\psi = \theta = 0$ , $l_i = 1$ and $r_p = 1$ ). . . . .	23
2.3	Flow diagram of the algorithm to obtain the parasitic motions mappings <i>vs.</i> $\psi$ and $\theta$ . . . . .	27
2.4	Parasitic motions for the MICRO case, (a) along $X$ -axis and (b) along $Y$ -axis (c) around $Z$ -axis, at $z = 0.999$ , $\alpha = -\beta = 120^\circ$ , $l_i = 1$ and $r_p = 1$ . . . . .	30
2.5	Parasitic motions for the MACRO case, (a) along $X$ -axis and (b) along $Y$ -axis (c) around $Z$ -axis, at $z = 1/\sqrt{2}$ , $\alpha = -\beta = 120^\circ$ , $l_i = 1$ and $r_p = 1$ . . . . .	31
3.1	Condition number ( $\kappa$ ) <i>vs.</i> $l_i$ , with $z = 0.999 \cdot l_i$ , $r_p = 1$ and $\alpha = -\beta = 120^\circ$ . . . . .	33
3.2	Mappings of the condition number <i>vs.</i> $\psi$ and $\theta$ . . . . .	35
3.3	Condition number for two different $Z$ positions. . . . .	37
3.4	Flow diagram of the procedure used to obtain the workspace plots. . . . .	41
3.5	Search direction. . . . .	42
3.6	Workspace plots for $r_p = 1$ , $\alpha = -\beta = 120^\circ$ , $l_i = 1$ ( $i = 1, 2, 3$ ) and $cond_{\max} = 10$ . The $z$ position is plotted as a percentage of the leg length ( $l_i$ ). . . . .	44
3.7	Contour plots of the workspace plots for $r_p = 1$ , $\alpha = -\beta = 120^\circ$ , $l_i = 1$ ( $i = 1, 2, 3$ ) and $cond_{\max} = 10$ . . . . .	45
3.8	Maximum angles <i>vs.</i> $l_i$ . . . . .	48

3.9	Comparison of the shape and size of the workspace when varying the platform radius ( $r_p$ ). The remaining parameters were set to: $\alpha = -\beta = 120^\circ$ , $l_i = 1$ ( $i = 1, 2, 3$ ) and $cond_{max} = 5$ . . . . .	49
3.10	Comparison of the shape and size of the workspace when varying the leg length ( $l_i$ ). The remaining parameters were set to: $\alpha = -\beta = 120^\circ$ , $r_p = 1$ and $cond_{max} = 5$ . . . . .	50
3.11	Comparison of the dexterous workspace for four different values of $cond_{max}$ . $r_p = 1$ , $\alpha = -\beta = 120^\circ$ and $l_i = 1$ ( $i = 1, 2, 3$ ). . . . .	51
3.12	Contour plots of the comparison of the workspace for varying $\alpha$ and $\beta$ , for symmetrical configurations ( <i>i.e.</i> $\alpha = -\beta$ ). $r_p = 1$ , $l_i = 1$ ( $i = 1, 2, 3$ ) and $cond_{max} = 5$ . . . . .	52
4.1	Total translational parasitic motion at $z = 0.999$ , $\alpha = -\beta = 120^\circ$ and $l_i = r_p = 1$ . . . . .	57
4.2	Flow diagram for the maps over the $\alpha$ - $\beta$ plane. . . . .	62
4.3	Average of the $x$ parasitic motion ( $x_{ave}$ ) <i>vs.</i> $\alpha$ and $\beta$ . . . . .	63
4.4	Average of the total translational parasitic motion ( $\delta_{ave}$ ) <i>vs.</i> $\alpha$ and $\beta$ . . . . .	64
4.5	Contour plot of the average of the total parasitic motion ( $\delta_{ave}$ ) <i>vs.</i> $\alpha$ and $\beta$ . . . . .	65
4.6	Dexterity measure, $\kappa_{ave}$ <i>vs.</i> $\alpha$ and $\beta$ . . . . .	66
4.7	T configuration: $\alpha = 90^\circ$ and $\beta = -90^\circ$ . . . . .	68
4.8	Condition number ( $\kappa$ ) <i>vs.</i> $r_p$ , with $z = 0.999 \cdot l_i$ and $\alpha = -\beta = 120^\circ$ . . . . .	72
5.1	Frames, screws and forces represented for branch $i$ . . . . .	78
5.2	Flow diagram of the static force analysis . . . . .	88
5.3	Variation of stiffness with $z$ ( $\psi = \theta = 0$ ). The lower curve corresponds to $k_\psi$ and $k_\theta$ ( $k_\psi = k_\theta$ when $\psi = \theta = 0$ ). . . . .	91
5.4	Stiffness maps ( $z = 0.999$ ) a) $k_z$ , b) $k_\psi$ and c) $k_\theta$ . . . . .	92

# List of Tables

1.1	Requirements of the telescope image correction task using the secondary mirror. . . . .	3
2.1	Variable values for the micro and macro examples. . . . .	28
4.1	Parasitic motion optimization (MICRO case). . . . .	69
4.2	Parasitic motion optimization (MACRO case). . . . .	69
4.3	Dexterity measure optimization (MICRO case). . . . .	70
5.1	Comparison of the static force solution for the two methods (MICRO case). . . . .	89
5.2	Comparison of the static force solution for the two methods (MACRO case). . . . .	90

# Dedication

To Mónica, who has given me all her unconditional love.

To my Mother.

To my Brothers, Ricardo and Luis.

To my Grandparents, Juan Antonio, Ofelia, Josefina and specially Anselmo and Pilar.

To my Uncles and Cousins.

To my Father, Jimena, Jimenita, Mary and Bruni.

To all my friends scatter all over the world, the old ones and the new ones.

¡ No me bajo, No me bajo ... Y no me bajé !

# Acknowledgements

I would like to express my deepest gratitude to Professors Meyer Nahon and Ron Podhorodeski for their excellent guidance and invaluable help that many times extended outside academic matters.

I want to extend my gratitude to Professor Clément Gosselin for his great help on the development of the constraint equations and for the helpful discussions regarding that particular topic. I also want to thank Brad Buckham for his contributions on the research on telescope image correction and the first ideas about the HVRam mechanism developed before I started on the project.

I also want to thank all my fellow students, specially Burke Pond, John Van Vliet and Doug Perrault for the numerous helpful discussions regarding Matlab, Maple V and L<sup>A</sup>T<sub>E</sub>X.

Among the same lines, I greatly thank Doug Perrault, Georgina Hackett, Gary Wang and their respective families for letting Monica and I feel more than welcome.

These acknowledgments would never be complete without including the biggest thanks of all to my wife, Mónica, for all her love and support, specially throughout the last two years.

# Chapter 1

## Introduction

### 1.1 Telescope image correction

When looking at stars or galaxies through optical telescopes, the images can appear distorted due to atmospheric perturbations (turbulence), structural vibrations or wind-induced motions. In order to correct the image, modern large telescopes (*e.g.* Cassegrain type, see Figure 1.1) are equipped with devices to move and/or change the shape of their primary and/or secondary mirrors. This will correct most of the aberrations including the ones due to local turbulence (also known as. dome seeing), image motion and atmospheric turbulence. When the secondary mirror is used to correct the image it is necessary to translate and rotate the secondary mirror of the telescope, as seen in Figure 1.2. Recently, there has been interest in using parallel mechanisms to move either the primary or the secondary mirror as a rigid body at high frequencies to correct for the most important aberrations (Buckham, 1995 [5]; Pitz, 1993 [38]; Close and McCarthy, 1994 [12]; Smith, 1994 [41]; Smith and Parziale, 1996 [42]).

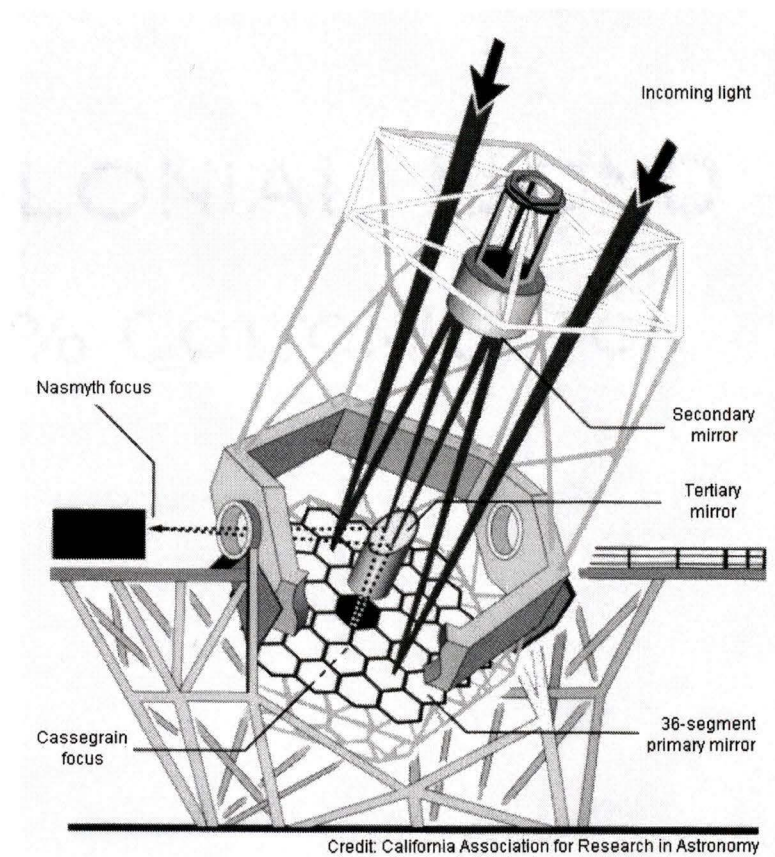


Figure 1.1: Cassegrain type optical telescope (*California Association for Research in Astronomy*).

Variable	Value/Range	Resolution
tip and tilt	$\pm 0.5$ degrees	$0.03 \times 10^{-3}$ degrees
focus	12 mm	$2 \times 10^{-6}$ m
mirror diameter	300 mm	
working frequency	70 Hz	
max. allowable disp. (along $x$ and $y$ )	$1 \times 10^{-6}$ m	

Table 1.1: Requirements of the telescope image correction task using the secondary mirror.

The requirements of the mechanism for the telescope application are shown in Table 1.1. The information presented in Table 1.1 was taken from a survey of several large telescopes (*e.g.* Keck 10m Telescope [28], UH/IfA [10], UKIRT [30][38]) compiled by Buckham [5]. Since the data varies considerably from one telescope to another, the worst case scenario was considered.

## 1.2 Literature review

### 1.2.1 Parallel mechanism design

Serial kinematic chains are those mechanisms that have a succession of links with an actuated joint between each one of the links, just like a human limb (see Figure 1.3.a). Parallel mechanisms are those that have two or more branches connected to a common payload, thus forming closed-loop kinematic chains (see Figure 1.3.b). With a parallel layout not all joints need to be actuated.

The advantages of parallel-architecture mechanisms, relative to serial architectures

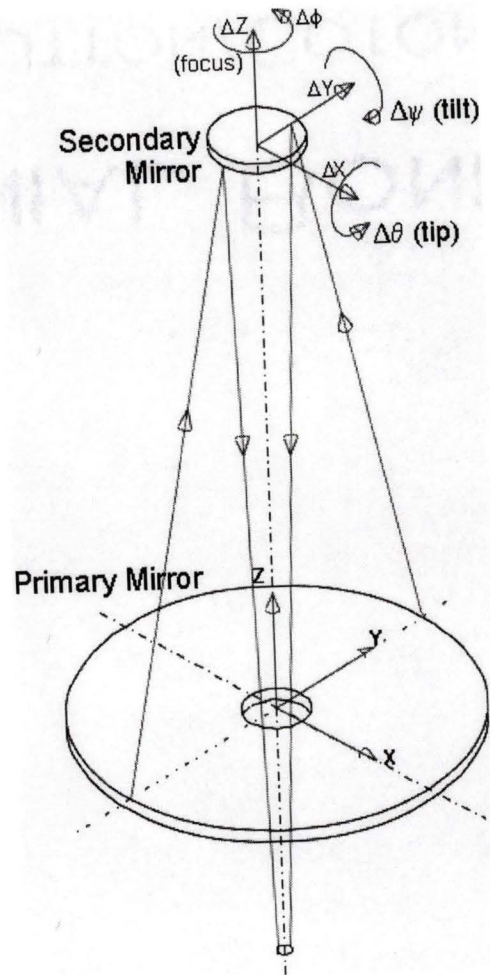


Figure 1.2: Secondary mirror motion directions

are well known: they can carry heavier payloads (high stiffness to weight ratio), move those payloads with greater accuracy (parallel mechanisms do not accumulate error when used in position control) and with a greater bandwidth [2]. These advantages come at the cost of a much more complicated dynamics model and a smaller reachable space. However, in telescope focussing applications, this last disadvantage is not problematic since the range of motions of interest for a typical secondary mirror is on the order of microns and milliradians (see Table 1.1). An extensive comparison of serial and parallel manipulator layouts can be seen in the work by Arai *et al.* [2] and by Ma [29].

Parallel mechanisms are becoming more widely used in a diversity of advanced applications, such as flight simulators, machine tools and micro-positioning devices. To a great extent, most attention on these devices centers on the six degree-of-freedom (dof) parallel mechanism originally proposed by Gough [20], but now commonly known as the Stewart Platform [43]. This platform, depicted in Figure 1.3.b, has been shown in many works to have very good performance in many applications, consisting of a balance between objectives of workspace, dexterity and stiffness. Alternative 6-dof architectures have also been studied, for example by Merlet and Gosselin [32], Nahon *et al.* [33] and Tahmashebi and Tsai [46], and have demonstrated good performance. However, many applications do not require a full six degrees of freedom from the moving platform.

### 1.2.2 Reduced degree-of-freedom designs

Reduced degree-of-freedom (*i.e.* dof < 6) architectures have the advantage of needing fewer actuators, thereby reducing the total cost of the device and making the controls

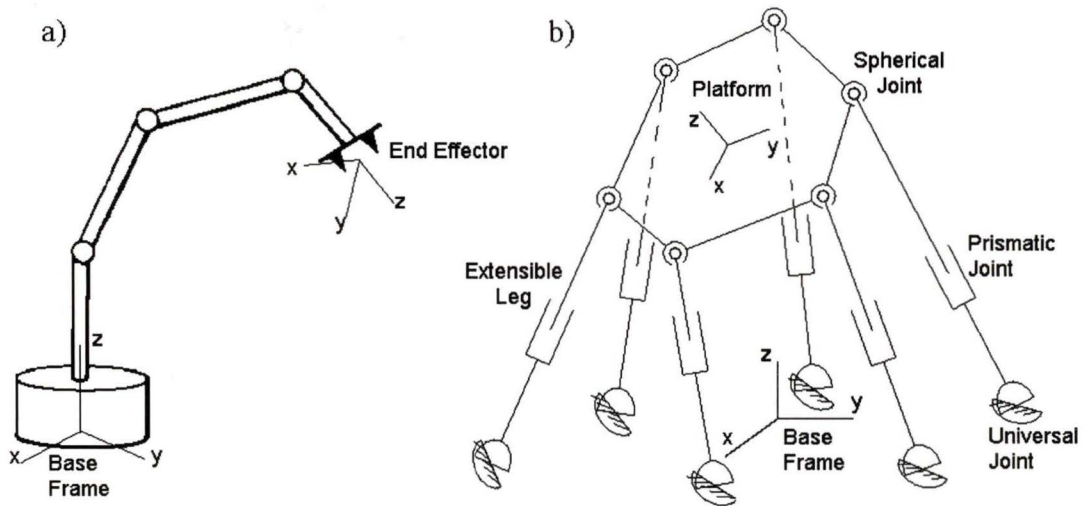


Figure 1.3: Manipulator topologies: a) serial kinematic chain and b) parallel kinematic chain (the basic layout of the Gough-Stewart platform).

much simpler. For example, the work of Pouliot *et al.* [40], studied certain three-dof parallel architectures for low-cost flight simulator motion platform applications. Their performance was found to be comparable to that of the Gough (Stewart) platform. Several other three-dof parallel mechanisms can also be found in the literature (see for instance [27], [48]).

The architecture analyzed in this work is depicted in Figure 1.4 and is described in detail in the next section. The architecture was originally proposed by B. Buckham for use as a moving platform for the secondary mirror of a Cassegrain telescope [6], [7] and was called the *HVRam*. This mechanism has the ability to perform 3-dof motion and is well suited to the tipping/tilting (2-dof orientation, pointing) and focusing (1-dof translation) of the telescope's secondary mirror.

While producing the above mentioned motions, this mechanism also generates

small constrained motions in the three remaining motion directions. These motions are termed *parasitic* and are necessary for the device to move. A thorough analysis of the inverse displacement problem and the associated parasitic motions is presented in Chapter 2 and is used as a basis for the study presented in this work.

Chapter 3 reports on the dexterity analysis for the introduced three dof parallel mechanism. The variations of the dexterity measure *vs.* several parameters are analyzed. A new definition of the *dexterous workspace* is also given in Chapter 3 where a workspace analysis is undertaken by observing the variations of the workspace volume with respect to several architectural parameters.

### 1.2.3 Architecture optimization

Examples in the literature of parallel manipulator optimization include finding optimal architectural parameter values for concerns of dexterity (*e.g.*, Pittens and Podhorodeski [37], Pouliot [39], Stoughton and Arai [44], Zanganeh and Angeles [49]) and for the size and quality of the workspace (*e.g.*, Gosselin and Angeles [18], Pouliot *et al.* [40]). For the introduced three-dof device, architectural parameter values can be determined to minimize objective functions related to the afore-mentioned parasitic motions or the dexterity.

Optimal selection of architectural parameter values to minimize translational parasitic motion and to optimize dexterity are considered in Chapter 4. Relevant design parameters are identified, objective functions related to translational parasitic motion and to the dexterity measure are defined, and a nonlinear optimization technique is applied to isolate optimal architectural (design) parameter values.

### 1.2.4 Static force analysis

The static force analysis covered in Chapter 5 deals basically with the problem of obtaining the actuator forces when a generalized force is applied at the tool (or end effector), *i.e.*, the inverse force problem is solved.

The same principles of conservation of power (often referred to as “virtual work” [3]) used in serial manipulators [31] can be used to derive an Inverse Force Solution (IFS) for a parallel manipulator. One problem of this derivation is that it does not give any information on any of the structural forces or torques.

An alternative method to obtain an IFS is to model the forces that each branch of the parallel mechanism can apply. This approach relies on the concepts of basic mechanics and allows actuator forces (torques) and structural forces (torques) to be obtained. Basic concepts of screw theory [22] are applied in Section 5.3 to obtain such an IFS.

## 1.3 Description of the mechanism

### 1.3.1 Kinematic layout

The mechanism analyzed in the present work has 3 actuated prismatic (P) joints, having displacements parallel to the base plane and relative angles  $\alpha$  and  $\beta$  as measured from the first ( $X$ -direction) actuator as illustrated in Figure 1.4. The orientation of this base plane will be referred to as horizontal. The distal end of each actuator is attached to the lower end of a constant-length leg by a passive (non-actuated) revolute (R) joint whose axis of rotation is perpendicular to the direction of the actuator and parallel to the horizontal base plane. The other end of each leg is fixed to the

moving platform with a passive spherical (S) joint. Thus, the base is attached to the moving platform by three identical PRS linkages. The spherical joints also have relative angles  $\alpha$  and  $\beta$  measured from the  $X$ -direction of the frame located at the center of the platform.

The HVRam mechanism can be viewed as a 3-dof version of the 6-dof mechanism proposed by Tahmashebi and Tsai [46] and by Ben-Horin and Shoham [4], obtained by constraining the actuators to move radially from a point on the base plane.

The HVRam mechanism is a three-degree-of-freedom (dof) parallel manipulator, as can be shown by applying the general mobility criterion [22]:

$$M = 6(n - g - 1) + \sum_{i=1}^g f_i \quad (1.1)$$

where  $M$  is the dof of the mechanism,  $n$  is the number of bodies in the mechanism,  $g$  is the number of joints and  $f_i$  is the number of degrees of freedom of the  $i$ -th joint. For the present mechanism, we have  $n = 8$ ,  $g = 9$ ,  $f_i = 3$  for the spherical joints, and  $f_i = 1$  for the prismatic and revolute joints. Thus, we obtain:

$$M = 6(8 - 9 - 1) + (3 + 3 + 3 + 1 + 1 + 1 + 1 + 1 + 1) = 3 \quad (1.2)$$

The three motion degrees of freedom achievable (approximately) by this device are rotation about two perpendicular axes intersecting at the mobile platform center and defining a horizontal plane, and a vertical translational motion. In telescope parlance, these are known as the tip/tilt/focus motion degrees of freedom. In fact, motion in tip and tilt induces a small amount of translational motion perpendicular to the respective axis of rotation (for individual rotations) and a rotation around the vertical direction. This has an unwanted “decentering” effect on the payload.

Besides the fact that the HVRam is a three dof mechanism, one of the biggest advantages of it is that the actuators are mounted at the base (they are fixed at

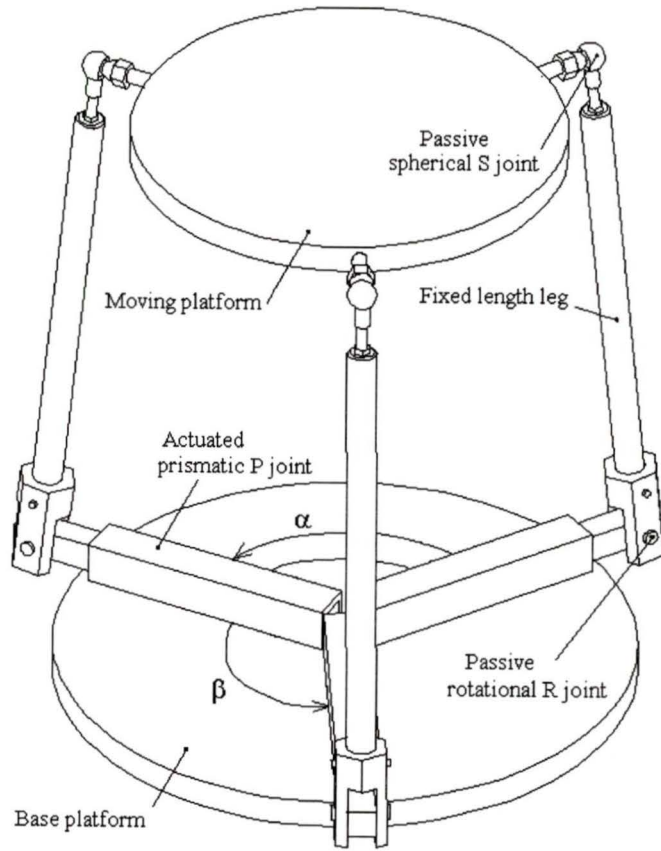


Figure 1.4: Proposed architecture: the HVRam mechanism.

the base plane) reducing the overall inertia of the mechanism adding more payload capabilities. This is an important observation since one of the requirements of the focusing device is to avoid inducing vibrations on the structure of the telescope.

### 1.3.2 Potential applications

Other potential applications, besides the telescope focusing device, requiring larger (macro) task displacements can be easily imagined. One of them could be pointing and elevating a cutting tool in machining and micro-machining (see communications of [43]), where a workpiece table (also known as the hardened bed ways) moving in two linear directions, namely  $x$  and  $y$ , would add the remaining degrees of freedom needed for the task.

Another application, where parallel mechanisms find broad application, is vehicle motion simulation (see for instance [1], [4], [43], [48]). Reduced dof mechanisms (less than six) have been demonstrated to have similar performance to the Gough (Stewart) platform in particular motion simulations ([33], [40], [48]).

In this work two applications (or cases) are analyzed. One focuses on the telescope application mentioned earlier (namely the *micro case*) and the other one deals with a more general case where the manipulator will be in a configuration with greater mobility (namely the *macro case*) as will be seen in Chapters 2 and 3.

### 1.3.3 Exploiting the mechanical advantage near an all-branch-singular configuration

One of the requirements which was desired in the telescope application was for the mechanism to have a high degree of precision (on the order of a few nanometers)

while using relatively conventional actuators. In order to achieve this, the device can be operated close to the all-branch singular configuration reached when the three legs become vertical. In this configuration, a relatively large actuator displacement will yield only a small motion of the top platform, *i.e.*, the mechanical advantage inherent in the configuration can be exploited ([24], [47]).

# Chapter 2

## Kinematic analysis

### 2.1 Inverse kinematics

#### 2.1.1 Inverse Displacement Solution (IDS)

The *inverse displacement problem* consists of determining the displacement of the actuated variables for a known position and orientation of the end-effector. For the considered three dof device this can be represented by

$$\mathbf{s} = \mathbf{f}(\mathbf{x}) \quad (2.1)$$

where  $\mathbf{s} = [s_1, s_2, s_3]^T$  represents the set of the three actuated joint variables and  $\mathbf{x} = [x, y, z, \psi, \theta, \phi]^T$  represents the set of Cartesian variables which specify the position and orientation of the upper platform.

The Cartesian variables are expressed as components with respect to the orientation of an inertial base frame fixed to the base platform. The coordinate axes of the inertial frame are denoted by  $OXYZ$  while those of the moving frame are denoted by  $O'X'Y'Z'$  (see Figure 2.1). In order to simplify the kinematic model, the

$X$ -axis of the inertial frame is aligned with one of the three actuators. The  $Y$ -axis also lies in the plane of the base platform while the  $Z$ -axis is normal to this plane and points upward, thereby forming a right-handed orthogonal frame. The origin of this frame is located at the intersection of the three actuators. The  $X'Y'$ -plane of the moving frame is aligned with the top platform with the origin at the center of the platform. The  $X'$ -axis points towards attachment point  $A_1$  (this being the location of the spherical joint joining leg one to the top platform). The  $Z'$ -axis completes a right-handed coordinate system and points upward when the upper platform is in its home position. As shown in Figure 2.1:

$\mathbf{p} = [x, y, z]^T$  is the vector from  $O$ , the origin of the inertial base frame to,  $O'$ , the origin of the moving frame

$\mathbf{r}_i = [r_{ix}, r_{iy}, r_{iz}]^T$  is the vector from  $O$  to the  $i$ -th upper attachment  $A_i$

$\mathbf{a}_i = [a_{ix}, a_{iy}, a_{iz}]^T$  is the vector from  $O'$  of the moving (platform) frame to  $A_i$

$\mathbf{l}_i = [l_{ix}, l_{iy}, l_{iz}]^T$  is the vector from the lower attachment point  $S_i$  to  $A_i$  of the  $i$ -th leg. It should be noted that  $\|\mathbf{l}_i\|$  is constant for each leg.

$\mathbf{s}_i = [s_{ix}, s_{iy}, s_{iz}]^T$  is the vector from  $O$  to  $S_i$ . Note that  $\|\mathbf{s}_i\| = s_i$  is the length of the  $i$ -th actuator.

The components of  $\mathbf{p}$ ,  $\mathbf{r}_i$ ,  $\mathbf{a}_i$ ,  $\mathbf{l}_i$  and  $\mathbf{s}_i$  must all be expressed in the same frame. The orientation of the base (inertial) frame is used as this reference orientation. The components of the vectors  $\mathbf{a}_i$  are constant when expressed in the moving frame. Let  $\mathbf{a}'_i = [a'_{ix}, a'_{iy}, a'_{iz}]^T$  be the vector from the origin of the moving frame to the upper attachment point, expressed as components in the moving frame. The three

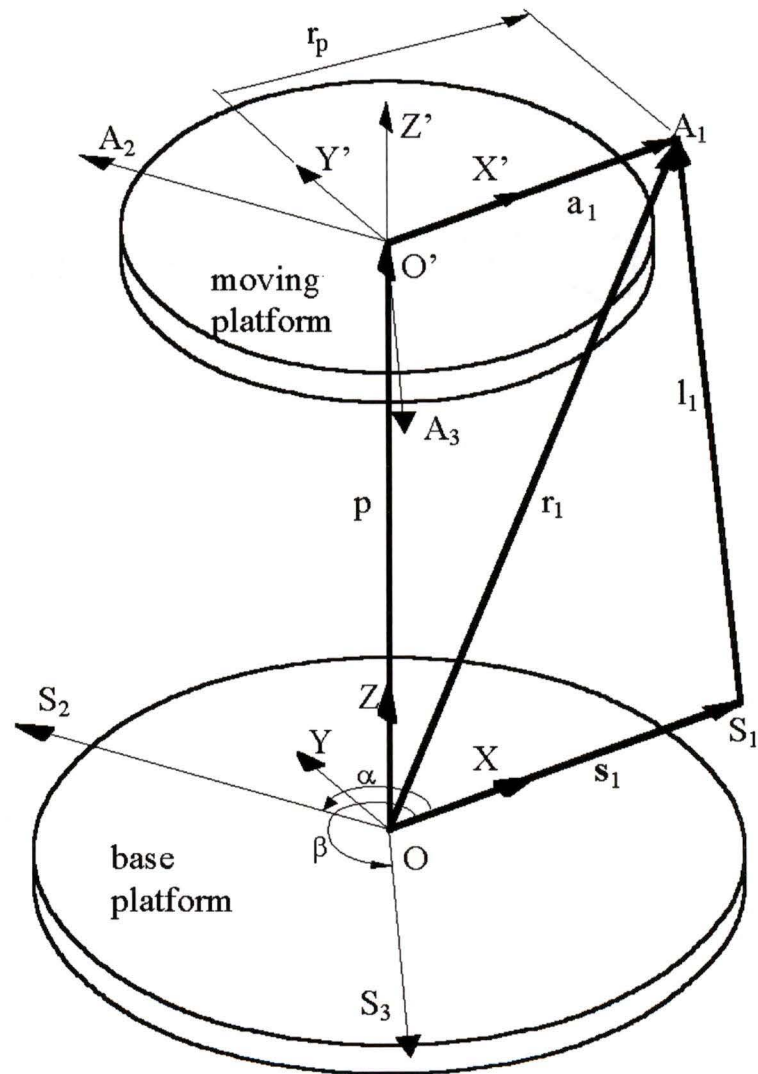


Figure 2.1: Vector representation one kinematic chain (leg).

components of  $\mathbf{r}_i = \mathbf{p} + \mathbf{a}_i$  can be obtained as follows:

$$\begin{aligned} r_{ix} &= x + T_{11}a'_{ix} + T_{12}a'_{iy} + T_{13}a'_{iz} \\ r_{iy} &= y + T_{21}a'_{ix} + T_{22}a'_{iy} + T_{23}a'_{iz} \\ r_{iz} &= z + T_{31}a'_{ix} + T_{32}a'_{iy} + T_{33}a'_{iz} \end{aligned} \quad (2.2)$$

where  $T_{ij}$  ( $i, j = 1, 2, 3$ ) are the elements of a rotation matrix,  $\mathbf{T}$ , describing the orientation of the moving frame with respect to the inertial reference frame.

In this work, an inertial frame referenced vertical displacement,  $z$ , is used to specify the elevation of a reference point (the origin  $O'$ ) on the payload with respect to the base platform. Similarly, inertial direction referenced desired (task) tip and tilt angles,  $\psi$  and  $\theta$ , are used to specify the desired payload orientation (pointing direction). Therefore a rotation representation consistent with the task requirements is defined as follows: *i*) rotation by an angle  $\phi$  about the inertial  $Z$ -direction followed by *ii*) rotation by an angle  $\psi$  about the inertial  $X$ -direction followed by *iii*) rotation by an angle  $\theta$  about the inertial  $Y$ -direction. This yields the rotation matrix:

$$\begin{aligned} \mathbf{T} &= \mathbf{T}_{ZXY} = \mathbf{R}_Y(\theta)\mathbf{R}_X(\psi)\mathbf{R}_Z(\phi) \\ &= \begin{bmatrix} c_\theta c_\phi + s_\psi s_\theta s_\phi & -c_\theta s_\phi + s_\psi s_\theta c_\phi & c_\psi s_\theta \\ c_\psi s_\phi & c_\psi c_\phi & -s_\psi \\ -s_\theta c_\phi + s_\psi c_\theta s_\phi & s_\theta s_\phi + s_\psi c_\theta c_\phi & c_\psi c_\theta \end{bmatrix} \end{aligned} \quad (2.3)$$

where  $c_*$  and  $s_*$  correspond to  $\cos(*)$  and  $\sin(*)$ , respectively. For the chosen representation the first rotation is about the inertial  $Z$ -direction with the mirror horizontal. This corresponds to a rotation about the axis of symmetry of the mirror. The fact that the rotation  $\phi$  is always about the axis of symmetry can also be seen by noting that an identical rotation matrix is obtained for the Euler angle representation: *i*) rotation by  $\theta$  about the original  $Y$ -direction followed by *ii*) rotation by  $\psi$  about the new

$X$ -direction followed by *iii*) rotation by  $\phi$  about the resulting “new new”  $Z$ -direction. This final  $Z$ -direction is aligned with the  $Z'$  axis, *i.e.*, it is in the surface normal of the mirror.

By noting that  $\mathbf{l}_i = \mathbf{r}_i - \mathbf{s}_i$ , the square of the length of the  $i$ -th leg can be expressed as

$$l_i^2 = (r_{ix} - s_{ix})^2 + (r_{iy} - s_{iy})^2 + (r_{iz} - s_{iz})^2 \quad (2.4)$$

where, from Figure 2.1, the vectors  $\mathbf{s}_i$  can be expressed as a function of the length of the  $i$ -th actuator,  $s_i$ , and the angles  $\alpha$  and  $\beta$  on the  $OXY$  plane measured from the  $X$  axis to the direction of the  $i$ -th actuator (*i.e.* the angles between  $\mathbf{s}_1$  and  $\mathbf{s}_2$  and between  $\mathbf{s}_1$  and  $\mathbf{s}_3$ , respectively), yielding:

$$\mathbf{s}_1 = \begin{bmatrix} s_1 \\ 0 \\ 0 \end{bmatrix}, \quad \mathbf{s}_2 = \begin{bmatrix} s_2 C_\alpha \\ s_2 S_\alpha \\ 0 \end{bmatrix}, \quad \mathbf{s}_3 = \begin{bmatrix} s_3 C_\beta \\ s_3 S_\beta \\ 0 \end{bmatrix} \quad (2.5)$$

The same process can be used to express the coordinates of  $\mathbf{a}'_i$  in the moving frame as functions of the radius of the moving platform  $r_p$  and the angles  $\alpha$  and  $\beta$ , that is:

$$\begin{aligned} \mathbf{a}'_1 &= \begin{bmatrix} a'_{1x} \\ a'_{1y} \\ a'_{1z} \end{bmatrix} = \begin{bmatrix} r_p \\ 0 \\ 0 \end{bmatrix} \\ \mathbf{a}'_2 &= \begin{bmatrix} a'_{2x} \\ a'_{2y} \\ a'_{2z} \end{bmatrix} = \begin{bmatrix} r_p C_\alpha \\ r_p S_\alpha \\ 0 \end{bmatrix} \\ \mathbf{a}'_3 &= \begin{bmatrix} a'_{3x} \\ a'_{3y} \\ a'_{3z} \end{bmatrix} = \begin{bmatrix} r_p C_\beta \\ r_p S_\beta \\ 0 \end{bmatrix} \end{aligned} \quad (2.6)$$

Finally, combining equations (2.4) and (2.5),  $s_i$  can be obtained as:

$$\begin{aligned}
 s_1 &= r_{1x} \pm \sqrt{l_1^2 - r_{1y}^2 - r_{1z}^2} \\
 s_2 &= r_{2x}c_\alpha + r_{2y}s_\alpha \pm \sqrt{l_2^2 - (r_{2x}s_\alpha - r_{2y}c_\alpha)^2 - r_{2z}^2} \\
 s_3 &= r_{3x}c_\beta + r_{3y}s_\beta \pm \sqrt{l_3^2 - (r_{3x}s_\beta - r_{3y}c_\beta)^2 - r_{3z}^2}
 \end{aligned} \tag{2.7}$$

Solution of equations (2.2) for  $\mathbf{r}_i$ ,  $i = 1, 2, 3$ , followed by substitution into equations (2.7) results in the solution for  $s_i$ ,  $i = 1, 2, 3$ , *i.e.*, the solution to the inverse displacement problem. It should be noted that there exist two solutions for each actuator, thereby yielding a total of 8 possible combinations of actuator extensions for a given platform position and orientation. In the present work, the positive square root has always been selected to yield a solution where the legs tend to be inclined inward from bottom to top.

### 2.1.2 Constraint equations

The motion of the payload platform is constrained to lie in a three dof subspace of the six dof space of general spatial motion. The desired pointing direction and location of the payload are specified in terms of  $\psi$  and  $\theta$  and the desired platform center elevation,  $z$ . In order to achieve the desired pointing direction, the payload will undergo a small pan  $\phi$  angle in addition to tip  $\psi$  and tilt  $\theta$  angles.

The mechanism being analyzed here is a spatial mechanism, so that specifying the position and orientation of the upper platform with respect to the reference frame, requires at least 6 variables to be specified. These six variables have been chosen as the elements of  $\mathbf{x} = [x, y, z, \psi, \theta, \phi]^T$  (*i.e.* the three Cartesian coordinates of a given point on the platform and the three angles, all with respect to the inertial

axes directions). As shown earlier, the HVRam mechanism is a three-dof parallel mechanism, which implies that only three variables can be specified independently. Constraint equations which relate the other three elements of  $\mathbf{x}$  with these specified variables must be determined.

The choice of which Cartesian variables are considered to be constrained and which are unconstrained is based on the requirements of the mechanism described in the introduction. The three desired motions of the mechanism are the translation in the  $Z$  direction, and the rotations about the  $X$  and  $Y$  axes directions (angles  $\psi$  and  $\theta$ ), leaving the translations along  $X$  and  $Y$  and the rotation about the  $Z$  direction (angle  $\phi$ ) as the constrained variables. Since the HVRam is a three-degree-of-freedom mechanism it is possible to obtain three constraint equations that will give the constrained variables ( $x$ ,  $y$  and  $\phi$ ) as functions of the unconstrained variables ( $z$ ,  $\psi$  and  $\theta$ ).

Analyzing the mechanism, it is possible to see that the upper attachment point  $A_i$  (the spherical joint) can only move in a plane generated by the vectors  $\mathbf{s}_i$  and  $\mathbf{l}_i$  (i.e. the  $i$ -th actuator and the  $i$ -th leg). Therefore the following three equations can be generated which represent the constraints for each leg:

$$r_{1y} = y + T_{21}r_p = 0 \quad (2.8)$$

$$r_{2y} = r_{2x} \tan(\alpha) \quad (2.9)$$

$$r_{3y} = r_{3x} \tan(\beta) \quad (2.10)$$

with for example,

$$r_{2x} = x + T_{11}a'_{2x} + T_{12}a'_{2y} \quad (2.11)$$

$$= x + T_{11}r_p c_\alpha + T_{12}r_p s_\alpha$$

$$r_{2y} = y + T_{21}a'_{2x} + T_{22}a'_{2y} \quad (2.12)$$

$$= y + T_{21}r_p c_\alpha + T_{22}r_p s_\alpha$$

Substituting the last 2 equations into equation (2.9) and obtaining the same relations for the third leg the following system of equations is obtained:

$$y = -T_{21}r_p \quad (2.13)$$

$$y + T_{21}r_p c_\alpha + T_{22}r_p s_\alpha = \tan(\alpha) [x + T_{11}r_p c_\alpha + T_{12}r_p s_\alpha] \quad (2.14)$$

$$y + T_{21}r_p c_\beta + T_{22}r_p s_\beta = \tan(\beta) [x + T_{11}r_p c_\beta + T_{12}r_p s_\beta] \quad (2.15)$$

Substituting equation (2.13) into equation (2.14):

$$x = -T_{11}r_p c_\alpha - T_{12}r_p s_\alpha + \frac{r_p}{\tan(\alpha)} [T_{21}(c_\alpha - 1) + T_{22}s_\alpha] \quad (2.16)$$

Substituting equations (2.13) and (2.16) into equation (2.14) and replacing the elements of the rotation matrix  $\mathbf{T}$  with the corresponding expressions in equation (2.3), we find:

$$\phi = \tan^{-1} \left( \frac{-R}{S} \right) \quad (2.17)$$

where:

$$R = Ac_\psi(1 - c_\theta) - Bs_\psi c_\theta + Cs_\psi$$

$$S = As_\psi(1 - c_\theta) - Bc_\psi + Cc_\psi c_\theta$$

with

$$\begin{aligned} A &= c_\alpha - c_\beta \\ B &= s_\alpha - s_\beta \\ C &= \frac{c_\beta - 1}{\tan(\beta)} - \frac{c_\alpha - 1}{\tan(\alpha)} \end{aligned}$$

It should be noted that  $A$ ,  $B$  and  $C$  are constants while  $R$  and  $S$  are functions of the unconstrained (specified) variables  $\psi$  and  $\theta$  only. Finally substituting equation (2.17) into equations (2.13) and (2.16) yields:

$$\begin{aligned} x &= -r_p(c_\theta c_\phi + s_\psi s_\theta s_\phi)c_\alpha - r_p(-c_\theta s_\phi + s_\psi s_\theta c_\phi)s_\alpha \\ &\quad + \frac{r_p}{\tan(\alpha)}(c_\psi s_\phi(c_\alpha - 1) + c_\psi c_\phi s_\alpha) \end{aligned} \quad (2.18)$$

$$y = -c_\psi s_\phi r_p \quad (2.19)$$

It is interesting to note that there is no dependency on  $z$  in any of the equations defining the constrained variables.

### 2.1.3 Inverse Velocity Solution (IVS)

The Inverse Velocity Solution (IVS) must be solved when the velocity of the actuators is required given the Cartesian velocities of the actuator. This can be solved by taking the time derivative of equation (2.1) to obtain following equation:

$$\dot{\mathbf{s}} = \mathbf{J}\dot{\mathbf{x}} \quad (2.20)$$

where  $\dot{\mathbf{s}} \in \mathfrak{R}^3$  represents the joint velocities,  $\mathbf{J} = \left[ \frac{\partial \mathbf{S}}{\partial \mathbf{x}} \right]$  is the Jacobian matrix and  $\dot{\mathbf{x}} \in \mathfrak{R}^6$ . The first three elements of  $\dot{\mathbf{x}}$  are the translational velocities of the reference point on the upper platform, while the last three elements are the time derivatives of

the angles representing the orientation of the platform. The matrix  $\mathbf{J} \in \mathfrak{R}^{3 \times 6}$  is the conventional Jacobian matrix formulated as follows:

$$\mathbf{J} = \begin{bmatrix} \frac{\partial s_1}{\partial x} & \frac{\partial s_1}{\partial y} & \frac{\partial s_1}{\partial z} & \frac{\partial s_1}{\partial \psi} & \frac{\partial s_1}{\partial \theta} & \frac{\partial s_1}{\partial \phi} \\ \frac{\partial s_2}{\partial x} & \frac{\partial s_2}{\partial y} & \frac{\partial s_2}{\partial z} & \frac{\partial s_2}{\partial \psi} & \frac{\partial s_2}{\partial \theta} & \frac{\partial s_2}{\partial \phi} \\ \frac{\partial s_3}{\partial x} & \frac{\partial s_3}{\partial y} & \frac{\partial s_3}{\partial z} & \frac{\partial s_3}{\partial \psi} & \frac{\partial s_3}{\partial \theta} & \frac{\partial s_3}{\partial \phi} \end{bmatrix} \quad (2.21)$$

This  $3 \times 6$  Jacobian matrix was computed symbolically using Maple V [11] and is included as Appendix A.

### 2.1.4 Coupling of the constraint equations to the Jacobian matrix

It is now necessary to couple the constraint equations to the kinematic model, thereby imposing the constraints on the model presented in equation (2.20). This is achieved with the following transformation:

$$\dot{\mathbf{x}} = \mathbf{P}\dot{\mathbf{x}}' \quad (2.22)$$

where  $\dot{\mathbf{x}} = [\dot{x}, \dot{y}, \dot{z}, \dot{\psi}, \dot{\theta}, \dot{\phi}]^T$ ,  $\dot{\mathbf{x}}' = [\dot{z}, \dot{\psi}, \dot{\theta}]^T$  and  $\mathbf{P}$  is a  $6 \times 3$  Jacobian matrix obtained from the three constraint equations (2.17), (2.18) and (2.19):

$$\mathbf{P} = \begin{bmatrix} \frac{\partial x}{\partial z} & \frac{\partial x}{\partial \psi} & \frac{\partial x}{\partial \theta} \\ \frac{\partial y}{\partial z} & \frac{\partial y}{\partial \psi} & \frac{\partial y}{\partial \theta} \\ 1 & 0 & 0 \\ 0 & 1 & 0 \\ 0 & 0 & 1 \\ \frac{\partial \phi}{\partial z} & \frac{\partial \phi}{\partial \psi} & \frac{\partial \phi}{\partial \theta} \end{bmatrix} \quad (2.23)$$

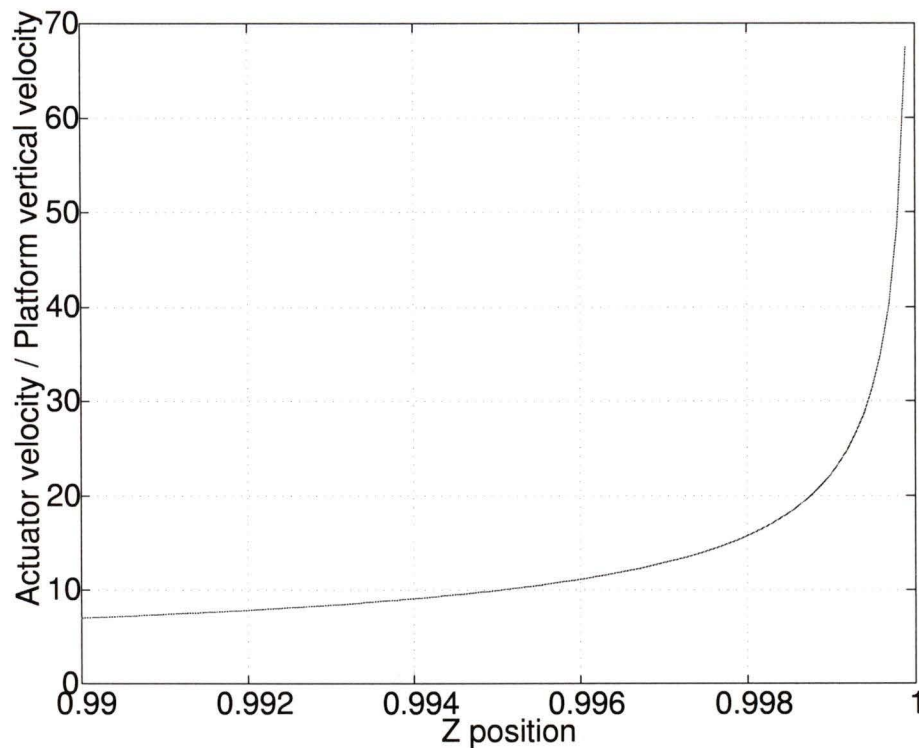


Figure 2.2: Ratio of actuator to platform velocity *vs.*  $z$  position of the upper platform ( $\psi = \theta = 0$ ,  $l_i = 1$  and  $r_p = 1$ ).

Note that rows 3 through 5 form an identity matrix because the three unconstrained variables are independent of each other. This  $6 \times 3$  Jacobian matrix was computed symbolically using Maple V and is included as Appendix B. Now substituting equation (2.22) into equation (2.20) yields:

$$\dot{\mathbf{s}} = \mathbf{J}'\dot{\mathbf{x}}' \quad (2.24)$$

where  $\mathbf{J}' = \mathbf{J}\mathbf{P}$  is the  $3 \times 3$  Jacobian matrix which includes the effect of the mechanical constraints on the mechanism.  $\mathbf{J}'$  will be called the constrained Jacobian matrix.

The constrained Jacobian matrix can now be used to demonstrate the desirable

mechanical advantage properties between the platform and actuator velocities near the all-branch singular configuration discussed in Section 1.3.3. Figure 2.2 shows the ratio of the velocity of actuator 1 to the vertical velocity of the platform, for values of  $z$  between 0.99 and 0.9999. Due to the symmetry of the mechanism, the other two actuator velocities are identical for strictly vertical platform motion. For this plot, the leg length and upper platform radius were taken to be 1 unit. As becomes apparent from this figure, small motions of the platform will require large actuator displacements, when the legs are nearly vertical. This would allow the use of relatively conventional actuator technology (e.g. electrical ballscrew actuators as opposed to piezoelectric) to perform nano-positioning of the mirror.

## 2.2 Forward kinematics

The *forward kinematics problem* consists of finding the set of Cartesian variables corresponding to a prescribed set of joint variables. This problem is more complicated than the inverse kinematic problem because (a) for parallel manipulators it often has no closed form solution and so requires the use of iterative numerical methods for its solution, and (b) it admits multiple solutions.

One approach which is computationally efficient, though has the disadvantage of only finding a single solution is that given by Dieudonne *et al.* [14]. It consists in applying a Newton-Raphson technique to find the solution to the set of nonlinear algebraic equations given by

$$\mathbf{s} - \mathbf{f}(\mathbf{x}) = \mathbf{0} \tag{2.25}$$

As part of this solution, the Jacobian matrix (equation (2.21)) of the system of equa-

tions must be calculated to allow the iterative resolution of the corrections for the values of  $\mathbf{x}$ .

A common approach to solve the computational cost problem and the non-uniqueness problem is by adding redundant sensors [35] on some of the unactuated joints to ensure a unique analytical solution. Another approach involves adding an extra kinematic chain with a simple kinematic layout and all joints sensed attached from the center of the base platform to the center of the moving platform (see for instance [2], [36]). Solving the forward kinematic problem for the additional chain (a serial manipulator forward kinematics problem), allows a unique solution to the forward displacement problem.

## 2.3 Parasitic motion

### 2.3.1 Definitions

The solution procedure to find values for the constrained variables  $x$ ,  $y$  and  $\phi$  from values for known unconstrained variables  $\psi$ ,  $\theta$  and  $z$  would entail first using equation (2.17) to solve for  $\phi$ ; and then using equations (2.18) and (2.19) to solve for  $x$  and  $y$ . Motion along the  $X$  and  $Y$  axes are deemed *parasitic motions* as a result of  $\psi$  and  $\theta$ . These parasitic motions must be kept very small to avoid distortion of the image. Displacements computed using the constraint equations (2.18) and (2.19) for a range of angles  $\psi$  and  $\theta$  and given  $z$ ,  $l_i$  and  $r_p$  values are shown in Figure 2.4. Note that rotation  $\phi$  has no effect on the image quality since the mirror is axi-symmetrical about its surface normal (the direction of the  $\phi$  rotation).

### 2.3.2 Algorithm

The variation of the parasitic motions with respect to the unconstrained variables ( $z$ ,  $\psi$  and  $\theta$ ) were obtained using the algorithm described here and illustrated in Figure 2.3. These behaviours can be seen as mappings of the parasitic motions.

First the  $z$  coordinate is fixed to a particular height and the angles  $\psi$  and  $\theta$  are initialized to a lower limit. Then the constrained variables are computed and stored. Next, the  $\theta$  coordinate is incremented by a specified  $\Delta\theta$  and the constrained variables are recalculated and this process continues until  $\theta$  reaches the upper limit (upper\_theta). When this happens it is reset to its lower value and  $\psi$  is increased by  $\Delta\psi$  and the process is repeated until  $\psi$  reaches its upper limit (upper\_psi). Once the process is finished the results are plotted as three dimensional surfaces, for example those seen in Figure 2.4.

### 2.3.3 Example results

The telescope (micro) application requires a range in tip and tilt angles ( $\psi$  and  $\theta$ , respectively) of  $\pm 0.0004$  radians. Figure 2.4 shows the behaviour of the parasitic motions in that range with a fixed coordinate  $z$  equal to 0.999 m. In order to normalize the dimensions of the mechanism the platform radius ( $r_p$ ) and the leg lengths ( $l_i$ , for  $i = 1, 2, 3$ ) were set to one metre. Table 2.1 depicts the values used for the micro and macro cases. The parasitic motions for the micro case were featured in Figure 2.4. The corresponding parasitic motions for the macro case are depicted in Figure 2.5.

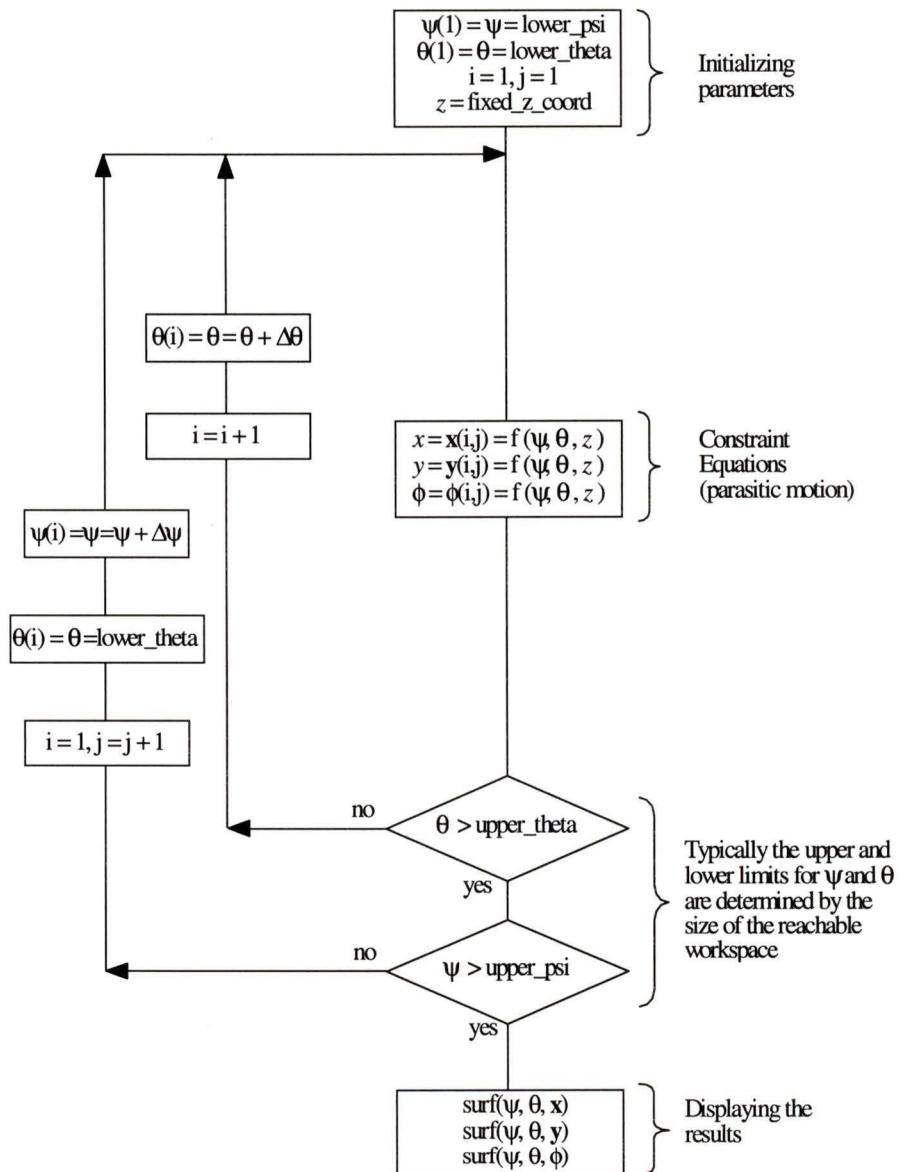


Figure 2.3: Flow diagram of the algorithm to obtain the parasitic motions mappings *vs.*  $\psi$  and  $\theta$ .

Variable	Micro case (telescope application)	Macro case
$z$ [m]	0.999	$1/\sqrt{2}$
$\psi$ and $\theta$ [rad]	$[-0.0004, 0.0004]$	$[-0.2, 0.2]$
$r_p$ [m]	1	1
$l_i$ ( $i = 1, 2, 3$ ) [m]	1	1
$\alpha = -\beta$	$120^\circ$	$120^\circ$

Table 2.1: Variable values for the micro and macro examples.

### 2.3.4 Behaviour of the parasitic motions

It is interesting to notice that there is no dependency on  $z$  or  $l_i$  in any of the equations defining the constrained variables (equations (2.17) to (2.19)). The  $z$  and  $l_i$  independencies can be confirmed by a geometrical approach. Each one of the three ball joints has to lie in a plane perpendicular to the base plane, and generated by the line of action of its prismatic actuator and the direction of its fixed length leg. For a particular  $z, \psi, \theta$  pose of the top platform there is just one way to place the platform so the center of the ball joints are each contained in their corresponding planes. Once the platform is located at that particular pose it can be moved vertically (along the  $Z$  axis) to any  $z$  position and the  $x, y, \psi, \theta$  and  $\phi$  pose displacement components of the platform will remain the same (explaining the parasitic motion  $z$  position independence). Now instead of changing the  $z$  position, one can change the leg length ( $l_i$ ) without changing the pose. Changing the leg length will change the actuator length (*i.e.*, the inverse displacement solution), but the  $x$  and  $y$  parasitic motions will remain the same.

Furthermore, these parasitic translational ( $x$  and  $y$ ) motions vary linearly with respect to  $r_p$  as seen in equations (2.18) and (2.19), respectively. And the rotational parasitic motion, angle  $\phi$ , is completely independent of  $r_p$  (equation (2.17)).

These independencies and linear dependencies will be investigated in more detail when optimization of geometric parameters to minimize parasitic motions is considered (Chapter 4).

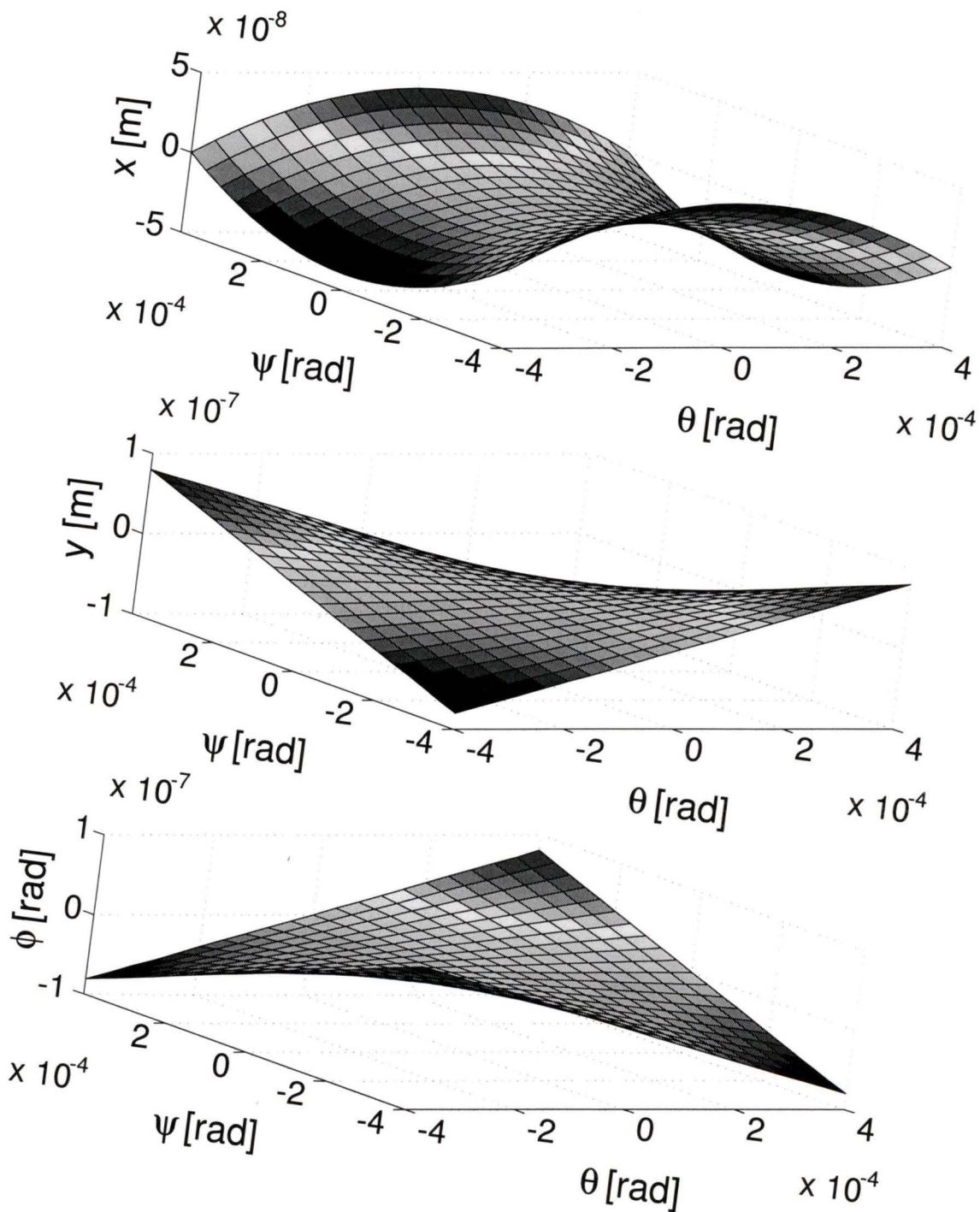


Figure 2.4: Parasitic motions for the MICRO case, (a) along  $X$ -axis and (b) along  $Y$ -axis (c) around  $Z$ -axis, at  $z = 0.999$ ,  $\alpha = -\beta = 120^\circ$ ,  $l_i = 1$  and  $r_p = 1$ .

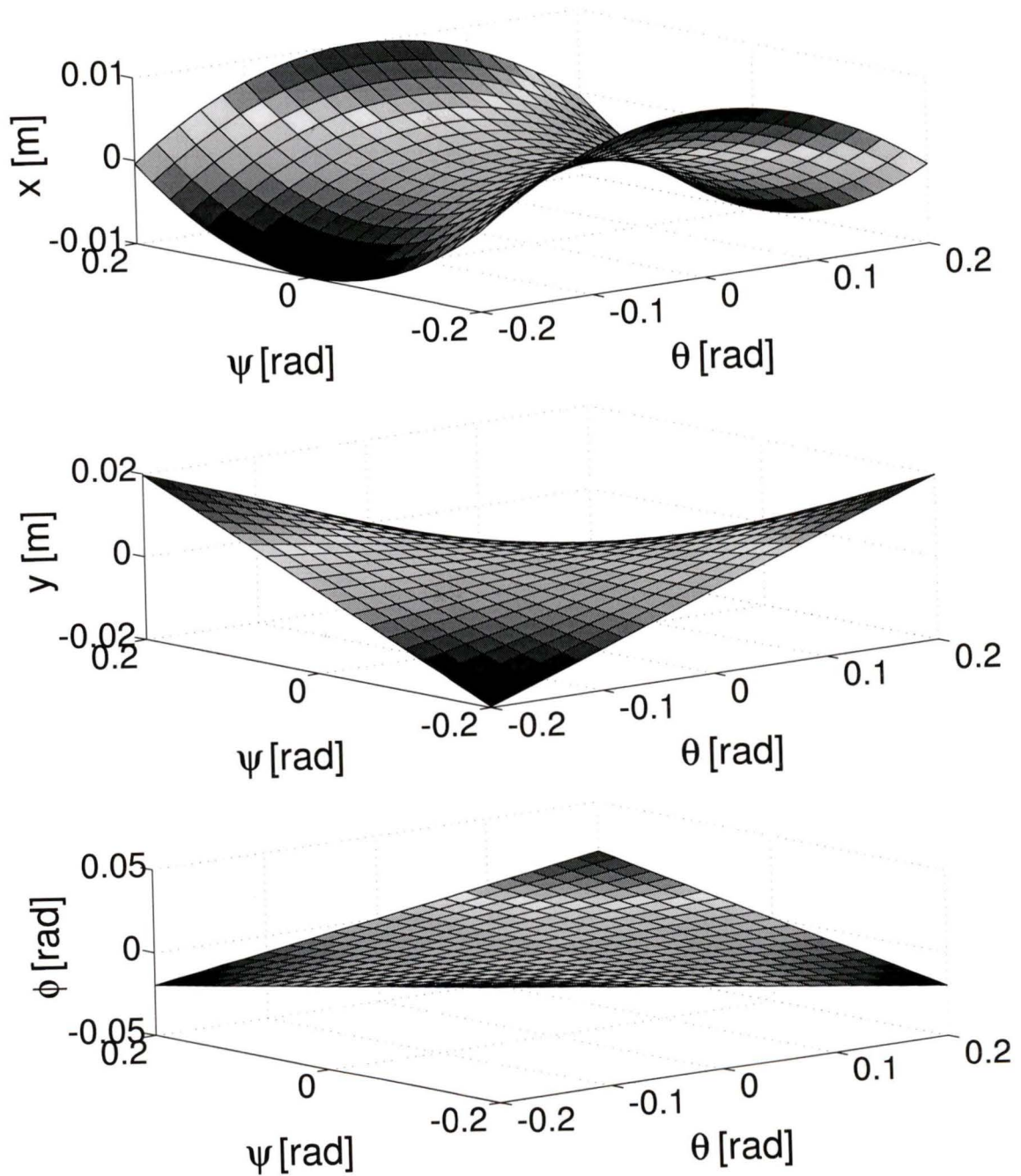


Figure 2.5: Parasitic motions for the MACRO case, (a) along  $X$ -axis and (b) along  $Y$ -axis (c) around  $Z$ -axis, at  $z = 1/\sqrt{2}$ ,  $\alpha = -\beta = 120^\circ$ ,  $l_i = 1$  and  $r_p = 1$ .

# Chapter 3

## Dexterity analysis

### 3.1 Definitions

The condition number  $\kappa$  of  $\mathbf{J}'$  (equation (2.24)) is a measure of the dexterity of the platform [25], [37]. An efficient way to compute  $\kappa$  is in terms of the singular values of the matrix  $\mathbf{J}'$  [25], [37], [45]:

$$\text{cond}(\mathbf{J}') = \kappa = \frac{\sigma_{\max}}{\sigma_{\min}} \quad (3.1)$$

where  $\sigma_{\max}$  and  $\sigma_{\min}$  are the maximum and minimum singular values, respectively.

The optimum value of the condition number is unity and occurs when  $\sigma_{\min} = \sigma_{\max}$ . A matrix is said to be well conditioned when  $\kappa$  is small and ill conditioned when  $\kappa$  is large. A well conditioned Jacobian matrix gives a more uniform set of possible velocities. Figure 3.3 shows the behaviour of the condition number with respect to the angles  $\psi$  and  $\theta$ . The best condition number is obtained when the top platform is parallel to the base platform. The condition number changes much more quickly when the top platform gets closer to the singularity at  $z = 1$ . It should be noted

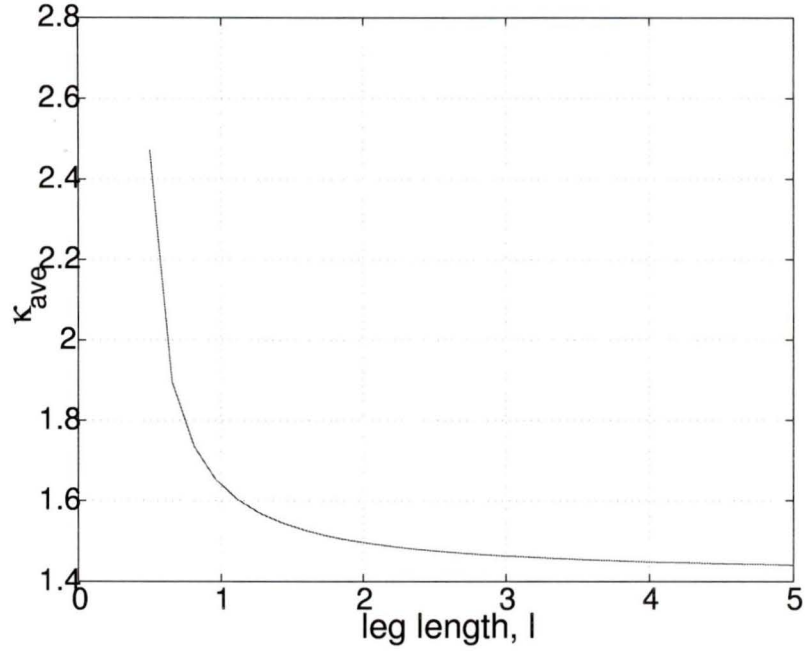


Figure 3.1: Condition number ( $\kappa$ ) vs.  $l_i$ , with  $z = 0.999 \cdot l_i$ ,  $r_p = 1$  and  $\alpha = -\beta = 120^\circ$ .

that the condition number will be affected by the choice of the reference point on the platform. For the platform under study, the center of the secondary mirror is located at the center of the upper platform, and it is the most relevant point to consider. Changes in the units used will also alter the condition number obtained, but do not alter the qualitative results shown in this chapter.

## 3.2 $\psi$ and $\theta$ mappings

### 3.2.1 Algorithm

To get a better understanding of the variation of the condition number  $\kappa$ , mappings of  $\kappa$  with respect to the unconstrained variables ( $z$ ,  $\psi$  and  $\theta$ ) were obtained following the algorithm described here and illustrated in Figure 3.2.

First, the  $z$  coordinate is fixed at a particular height and the angles  $\psi$  and  $\theta$  are initialized to a lower limit. Then, the constrained variables are computed and used with the unconstrained variables as inputs for the Jacobian matrix ( $\mathbf{J}$ ) and the constraint matrix ( $\mathbf{P}$ ). By multiplying these matrices, the constrained Jacobian matrix is obtained ( $\mathbf{J}' = \mathbf{JP}$ ). The condition number ( $\kappa$ ) of this matrix is then obtained and stored. Next, the  $\theta$  coordinate is incremented by a predetermined  $\Delta\theta$  and the constraint variables ( $x$ ,  $y$  and  $\phi$ ) and the matrices  $\mathbf{J}$ ,  $\mathbf{P}$  and  $\mathbf{J}'$  are recalculated together with the condition number. This process continues until  $\theta$  reaches the upper limit (upper\_theta). When this happens  $\theta$  is reset to its lower value and  $\psi$  is increased by  $\Delta\psi$  repeating the process until  $\psi$  reaches its upper limit (upper\_psi). Once the process is finished the results are plotted as a three dimensional surface which can be seen in Figure 3.3 for two  $z$  values.

### 3.2.2 Example results

Figure 3.3 shows that the condition number mappings with respect to  $\psi$  and  $\theta$  have a minimum at  $\psi = \theta = 0$ . Furthermore, the variation of the condition number mappings with respect to the  $z$  positions can be seen in the same figure, where it is evident that the condition number varies at a greater rate when the  $z$  position is

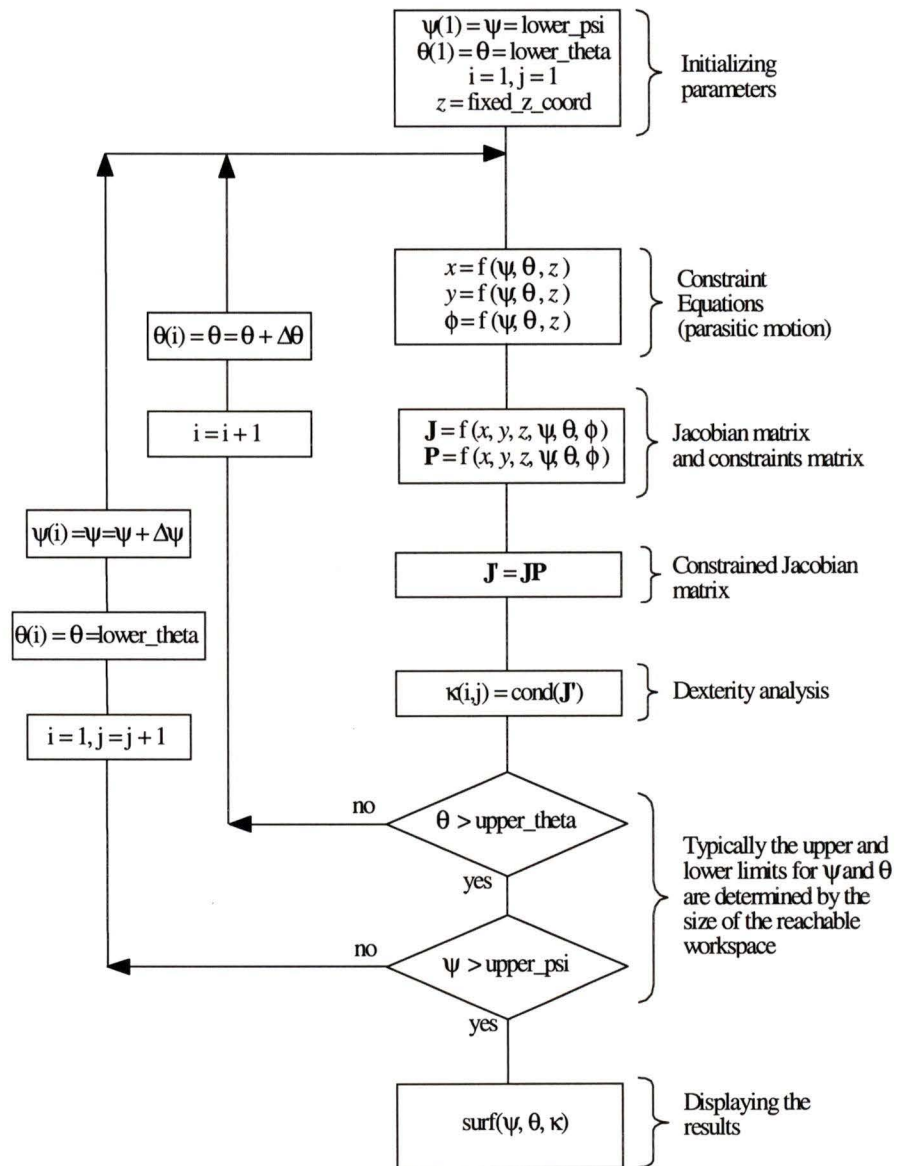


Figure 3.2: Mappings of the condition number *vs.*  $\psi$  and  $\theta$ .

incremented from 0.998 to 0.999 m.

It is also interesting to notice that the value of the  $\kappa$  is the same when  $\psi = \theta = 0$ , no matter what the  $z$  position is.

### 3.3 Frame and scale dependency

It is known that the condition number of a Jacobian matrix is frame and scale (unit) dependent. One must pick, as the reference point for the moving frame, the most significant point of the payload.

Some authors, like Zanganeh and Angeles [49], have dealt with the scale dependency problem by using a scale that will produce an isotropic architecture (*i.e.* the one that produces a condition number equal to one) in one particular configuration.

In the present case, the center of the moving payload (*i.e.* the center of the secondary mirror) was used. In this work, the choice of units, metres for distances and radians for rotations, lead to an evenly-weighted constrained Jacobian matrix, *i.e.* all the nine entries in the constrained Jacobian matrix have same orders of magnitude in most of the analyzed workspace. Since the results showed similar qualitative results regardless of weighting and since minimum  $\kappa$  values of less than 2 were obtained, this weighting was considered adequate for the research considered.

### 3.4 Behaviour of $\text{cond}(\mathbf{J}')$

From Figures 1.4 and 2.1 it is possible to see that the architectural layout can be defined by only four design parameters: the angles  $\alpha$  and  $\beta$  between legs, the fixed length leg  $l_i$  (same for all three legs) and the moving platform radius  $r_p$ .

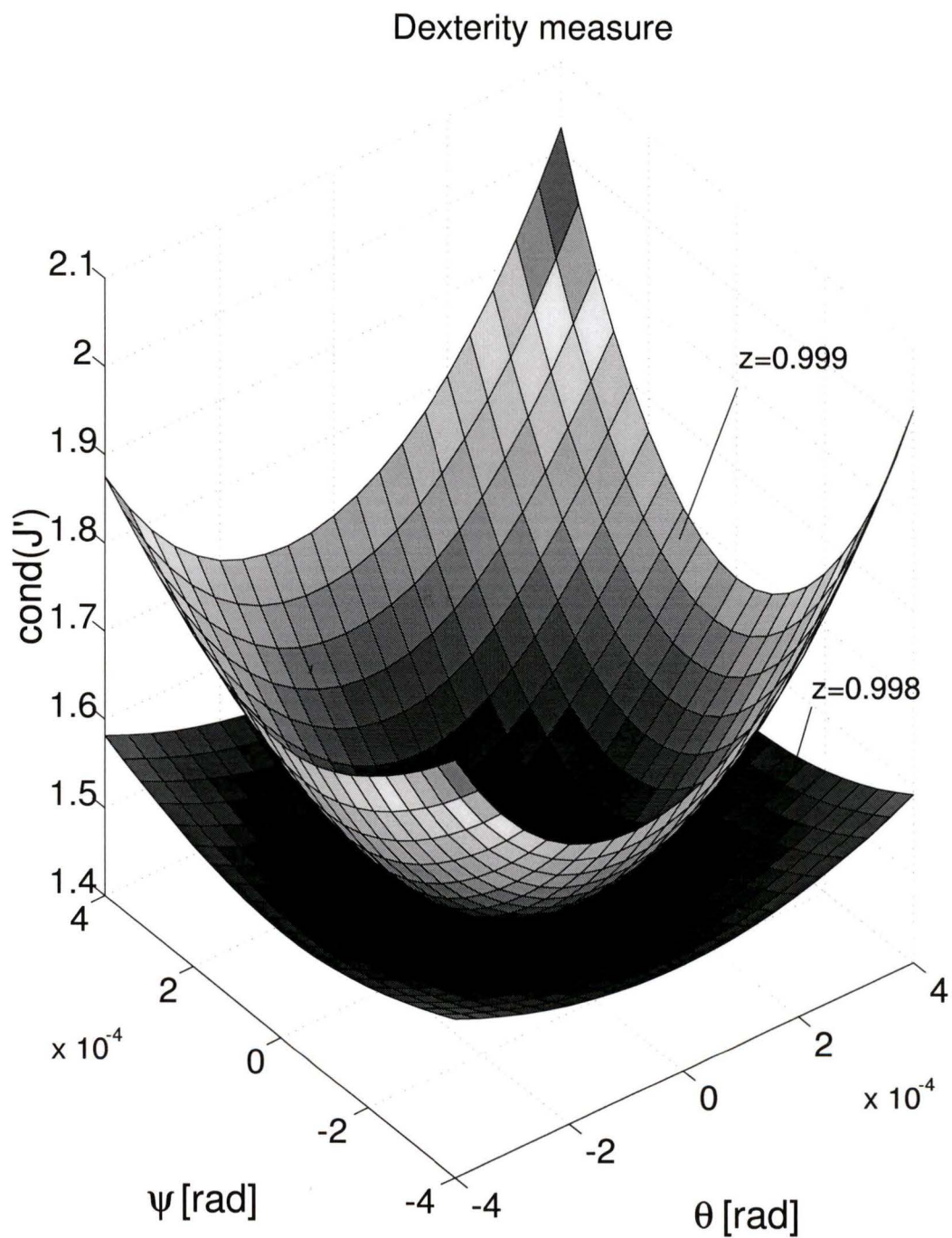


Figure 3.3: Condition number for two different  $Z$  positions.

A systematic study of the influence of each variable on the condition number  $\kappa$  showed dependency on all of the potential design variables. However, the dexterity measure decreases, *i.e.* improves, monotonically when  $l_i$  is increased and the rest of the parameters are kept constant as seen in Figure 3.1. Thus it is irrelevant to use  $l_i$  as an optimization parameter, since ultimately  $l_i$  will be limited by the application. The remaining architectural parameters, *i.e.*,  $\alpha$ ,  $\beta$  and  $r_p$ , are the relevant design variables for dexterity optimizations.

## 3.5 Dexterous workspace

This section reports a workspace analysis for the introduced three dof parallel mechanism [8]. Examples in the literature of reachable and dexterous workspace for parallel manipulators include finding optimal architectural parameter values for concerns of the size and quality of the workspace (*e.g.*, [18], [40]). In the present work, the effect on the workspace of variations in the architectural parameters is studied.

### 3.5.1 Definitions

The *reachable workspace* of a manipulator is the volume defined by the maximum reach of the manipulator (usually as a result of the physical limits on the passive or actuated joints). In the general case, the workspace is six dimensional (three translations  $-x, y, z$ - and three rotations  $-\psi, \theta, \phi$ ) and for that reason it is difficult to depict visually. In most cases the workspace is represented as three dimensional slices of the six dimensional volume, *i.e.*, maintaining three of the six dimensions fixed (see for instance [17]).

A variant of the workspace can be found in the literature called the *dexterous*

*workspace*. In most cases, the dexterous workspace is defined as the set of points where the gripper of a manipulator can reach while at the same time it can be oriented in a certain predetermined range(s) [26]. Note that all the possible dexterous workspaces are contained within the reachable workspace.

In this work, an alternative definition of the dexterous workspace is defined as the workspace that fulfills particular dexterity conditions, *e.g.*, the dexterity measure (such as the condition number of the constrained Jacobian matrix  $\mathbf{J}'$ ) being smaller than or equal to a particular predetermined limit<sup>1</sup>. This limit will keep the manipulator away from any singular configuration (where the parallel mechanism instantaneously gains one or more uncontrollable degrees of freedom) since at those conditions, the condition number approaches infinity. The dexterous workspace will always be smaller than the reachable workspace since the reachable workspace contains all the possible dexterous workspaces.

Since the mechanism analyzed in this work is a 3-dof mechanism, the workspace is defined as a three dimensional space, particularly in the three dimensions  $z$ ,  $\psi$  and  $\theta$ . The remaining three coordinates ( $x$ ,  $y$  and  $\phi$ ) can be expressed as a function of  $z$ ,  $\psi$  and  $\theta$  and no information is lost when plotting the three dimensional workspace volumes.

The architecture of the mechanism will have a big influence on the size, shape and symmetry of the workspace since the constrained Jacobian matrix is a function of all of the architectural (design) parameters, *i.e.*,  $\alpha$ ,  $\beta$ ,  $l_i$  and  $r_p$ . In this work, we are interested in the variation of the workspace with these parameters. This interest

---

<sup>1</sup>We decided to call it *dexterous workspace* since the dexterity measure limits the boundary of the available *dexterous points*.

imposes the need for an algorithm that can obtain the dexterous workspace for a given set of parameters.

### 3.5.2 Algorithm

In order to evaluate the dexterous workspace of our mechanism, a numerical procedure implemented in Matlab was developed. In this approach, the dexterity of the mechanism is evaluated at discrete points throughout its workspace. The procedure used to obtain the workspace plots is illustrated in Figure 3.4 and is described in this section.

The procedure starts by fixing the  $z$  position equal to  $z_{start}$ . Then, a radial search is made, where  $\psi$  and  $\theta$  each start from zero. A variable step size ( $\Delta_{angle}$ ), along a line with a particular angle ( $\varepsilon$ ) with respect to the horizontal axis ( $\psi$ ) as illustrated in Figure 3.5 is considered (*i.e.* the search is made in cylindrical coordinates [44]). The search is based on a bisection method [16]. The value of  $\Delta_{angle}$  is first set to an initial value ( $\Delta_{ang-start}$ ), then progressively increased, and the condition number of the constrained Jacobian matrix ( $\mathbf{J}'$ ) is evaluated at each step. When the (prescribed) maximum allowed condition number ( $cond_{max}$ ) is exceeded the angles  $\psi$  and  $\theta$  are decreased by  $\Delta\psi = \Delta_{angle} \sin(\varepsilon)$  and  $\Delta\theta = \Delta_{angle} \cos(\varepsilon)$ , respectively and the step size  $\Delta_{angle}$  is divided by two and the search keeps going. When  $\Delta_{angle}$  is smaller than a specified tolerance the value of  $\psi$  and  $\theta$  is recorded as a point on the boundary of the dexterous workspace. Then the angle  $\varepsilon$  is incremented by  $\Delta\varepsilon$  ( $\Delta\varepsilon = 2\pi/n_{meridians}$ ), the  $\Delta_{angle}$  is reset to  $\Delta_{ang-start}$  and the search starts again in the new direction with  $\psi = \theta = 0$ . Once  $\varepsilon$  reaches  $2\pi$ , the  $z$  position is incremented by  $\Delta z$  ( $\Delta z = |z_{end} - z_{start}|/n_{slices}$ ) and the search over the  $\psi$ - $\theta$  plane starts again.

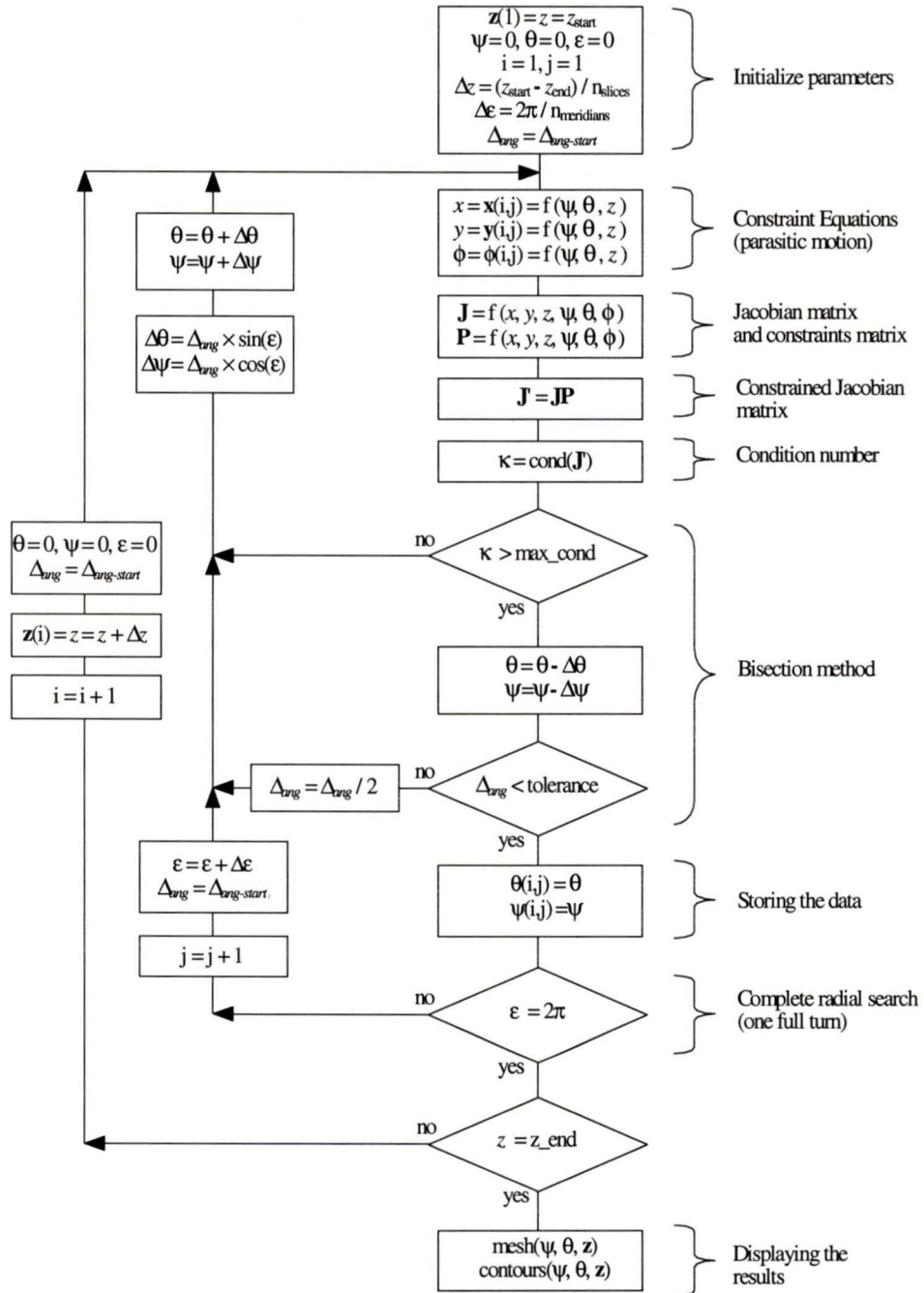


Figure 3.4: Flow diagram of the procedure used to obtain the workspace plots.

The sequence is repeated until the maximum  $z$  position is reached ( $z_{end}$ ).

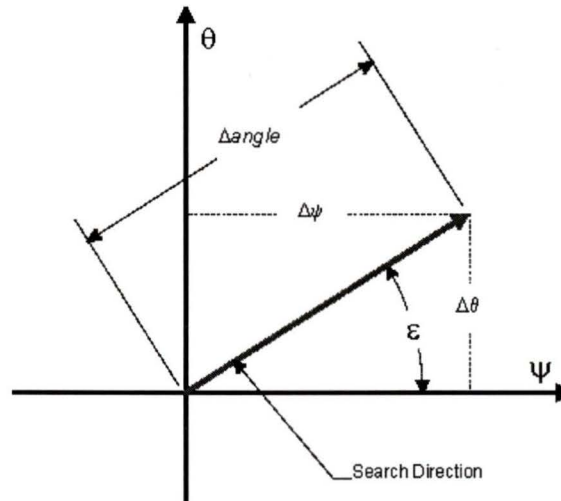


Figure 3.5: Search direction.

The inputs to the program are composed of the architectural parameters:

- the angle between legs:  $\alpha$  ( $= -\beta$ )
- the fixed leg lengths:  $l_i$  (for  $i = 1, 2, 3$ )
- the platform radius:  $r_p$

and the mappings parameters:

- the starting and ending heights:  $z_{start}$  and  $z_{end}$
- the maximum condition number allowed:  $cond_{max}$
- the number of slices in the  $Z$  direction:  $n_{slices}$
- the number of meridians:  $n_{meridians}$
- the bisection method tolerance:  $tolerance$

### 3.5.3 Examples

A sample of the workspace can be seen in Figure 3.6. In that figure one can see that, for the chosen parameters, the maximum cross sectional area of the workspace is reached at  $z = l_i/\sqrt{2}$ . At that particular height, the “horizontal” cross sections of the 3D mesh look close to circular (see Figure 3.7). Below that height ( $z < l_i/\sqrt{2}$ ) the workspace shrinks and starts to take on a triangular cross sectional shape. Finally, in the upper region ( $l_i/\sqrt{2} < z < l_i$ ), the cross sections become triangular which again can be seen in the top view of the contour plots shown in Figure 3.7.

To be able to compare results when one or more of the parameters is changed, the  $z$  position is presented as a percentage of the leg length ( $l_i$ ) since the maximum  $z$  position is equal to the leg length, and the minimum  $z$  position is considered to be equal to 0. No negative  $z$  position is reachable since the manipulator would have to cross through a singular configuration (all legs becoming horizontal) to reach them.

### 3.5.4 Discussion of results

The architectural parameters were varied within reasonable ranges. Figures 3.9 to 3.12 each present four images in which a particular architectural parameter is varied. The workspace from  $z = 0$  to  $z = 0.3 * l_i$  is not plotted in the aforementioned graphs (this section corresponds to the dark zone at the bottom of Figure 3.6), since that section of the workspace is computationally very expensive to calculate —one has to set a very small  $\Delta_{angle}$  to avoid crossing the singular configuration (when one or more legs is contained on the same plane as the top platform, see Figure 3.8) at those particular heights.

A very important characteristic of the workspace plots presented in this section

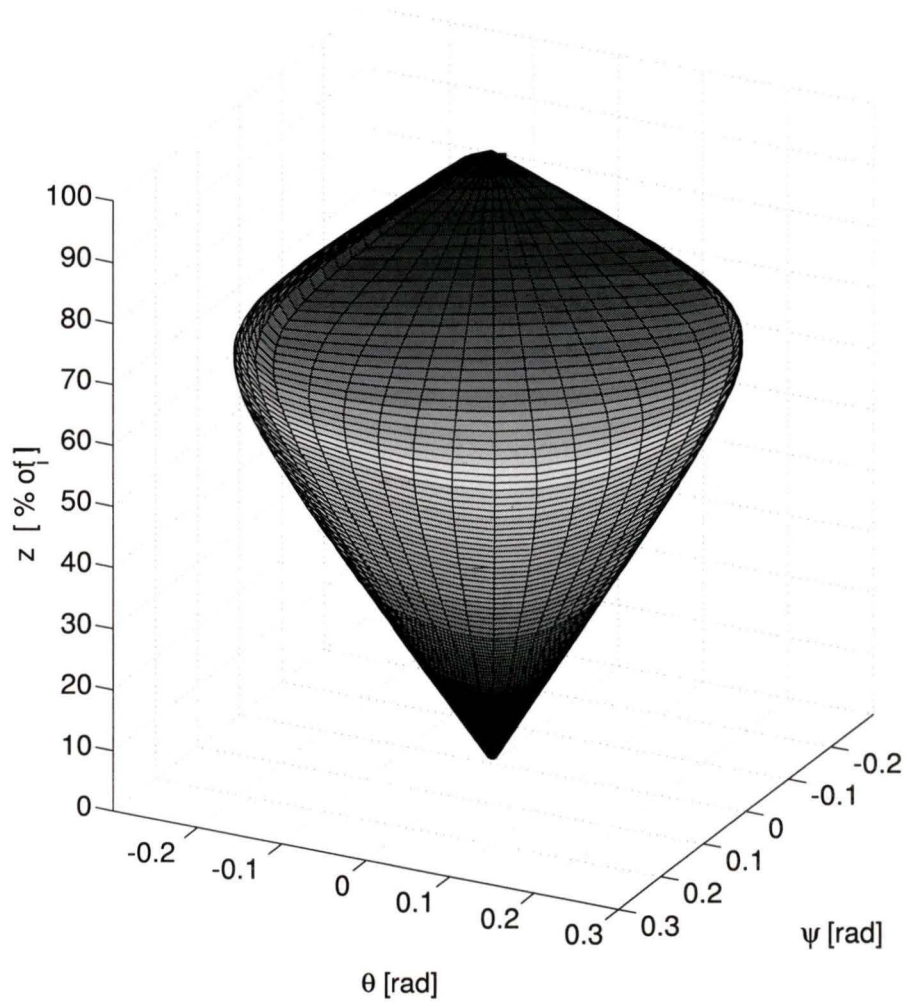


Figure 3.6: Workspace plots for  $r_p = 1$ ,  $\alpha = -\beta = 120^\circ$ ,  $l_i = 1$  ( $i = 1, 2, 3$ ) and  $cond_{\max} = 10$ . The  $z$  position is plotted as a percentage of the leg length ( $l_i$ ).

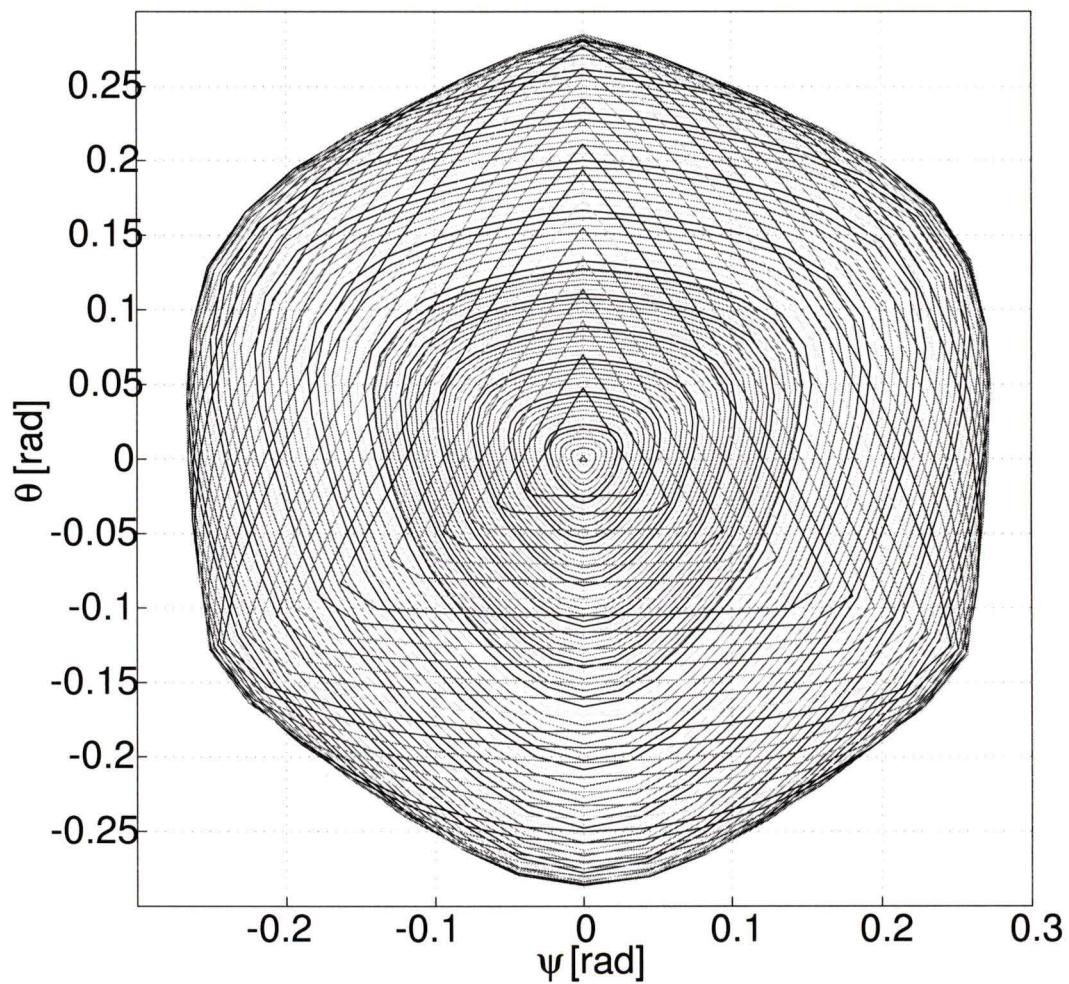


Figure 3.7: Contour plots of the workspace plots for  $r_p = 1$ ,  $\alpha = -\beta = 120^\circ$ ,  $l_i = 1$  ( $i = 1, 2, 3$ ) and  $cond_{\max} = 10$ .

is that they can be analyzed in two parts. The bottom section (approximately from  $z = 0$  to 60%) of the plots is limited by the proximity of the pose of the manipulator to force unconstrained configuration (when one or more of the directions of the fixed legs is contained in the top platform plane). The remaining top part of the plots is limited by the fact that the manipulator is reaching a branch singularity configuration (when the direction of the fixed length leg is normal to the base plane).

The following important effects can be deduced from Figures 3.9 to 3.12:

- The singularities (when one or more of the fixed length legs become aligned with the upper platform) are reached at larger  $\psi$  and  $\theta$  angles when the leg length  $l_i$  ( $i = 1, 2, 3$ ) is increased relative to  $r_p$  (see Figure 3.8), thereby increasing the workspace if  $r_p$  is decreased (with a maximum at  $r_p = 1/\sqrt{2}$  for  $l_i = 1$ ) or  $l_i$  is increased (see Figures 3.9 and 3.10, respectively).
- The workspace increases if the maximum condition number is increased (see Figure 3.11), since the workspace volume at a particular  $cond_{\max}$  must envelop that at a smaller  $cond_{\max}$ .
- The workspace appears to reach a maximum at  $z = 1/\sqrt{2}$  if  $r_p = 1$  and  $l_i = 1$  ( $i = 1, 2, 3$ ) (see Figure 3.6) no matter what value of  $cond_{\max}$  is used (see Figure 3.11).
- The maximum workspace is displaced to a larger  $z$  position if  $r_p$  is decreased and  $l_i$  ( $i = 1, 2, 3$ ) remains constant (see Figure 3.9).
- If  $l_i/\sqrt{2} < z < l_i$  the workspace has the shape of a tetrahedron, especially when  $r_p = 1$  (see Figure 3.7). As  $r_p$  is decreased ( $r_p < 1$ ) the shape of the tetrahedron becomes rounded (see Figure 3.9).

- It is possible to see in Figure 3.12 that the aspect ratios of the workspace (its relative size in the  $\psi$  and  $\theta$  directions) varies when the angle between the actuators is changed.

It is possible to notice that, since the condition number of the Jacobian matrix is scale (unit) dependent, all the architectural parameters will have an influence on the shape and size of the workspace, even when they are varied one with respect to the other. Despite this dependency it is still possible to depict the tendency of the dexterous workspace with respect to the variations of the architectural parameters.

### 3.6 Singular values analysis

The singular values ( $\sigma_i$ , for  $i = 1, 2, \dots, n$ ) are often used in robotics to represent the effort to move in different directions [34]. From an extensive analysis of the singular values the following remarks are made:

- the singular values increase when  $z$  gets closer to the upper limit ( $l_i$ ). However, the relation between the largest and the smallest remains the same when  $\psi = \theta = 0$  regardless of the  $z$  values, *i.e.* the condition number remains constant. This means that when the platform is closer to the upper limits the actuators have to make more effort to make the platform move. This is basically the reason why, for the telescope application, the platform is used near the upper boundary of the workspace.
- using metres and radians for measuring distances and angles, respectively, weights the singular values in such a way that the three singular values are close to one another within the analyzed workspace, *i.e.* the three singular values are of

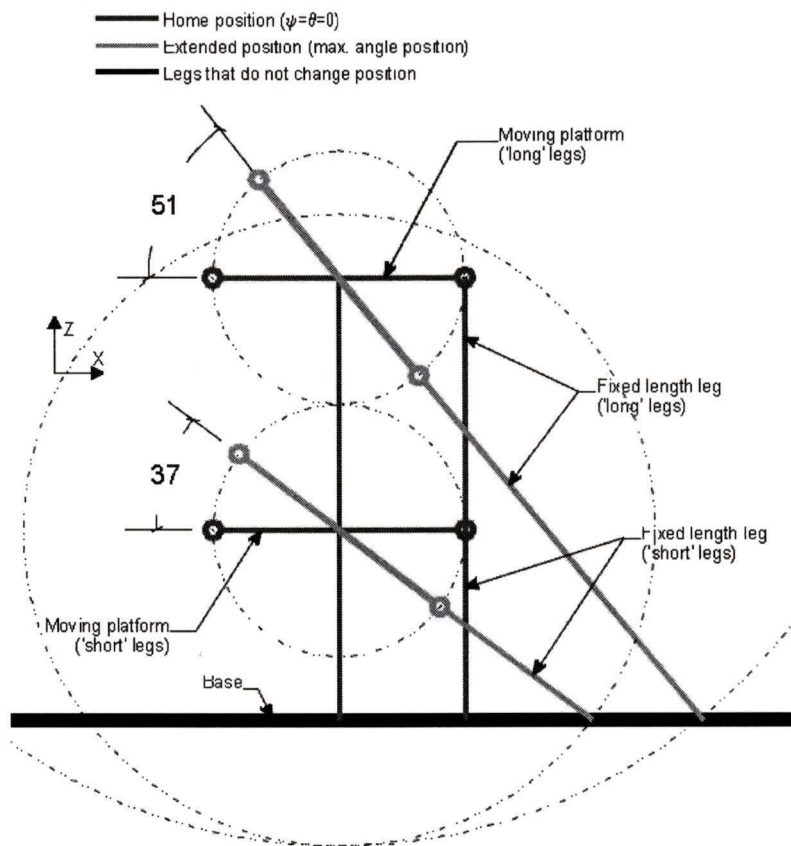


Figure 3.8: Maximum angles *vs.*  $l_i$ .

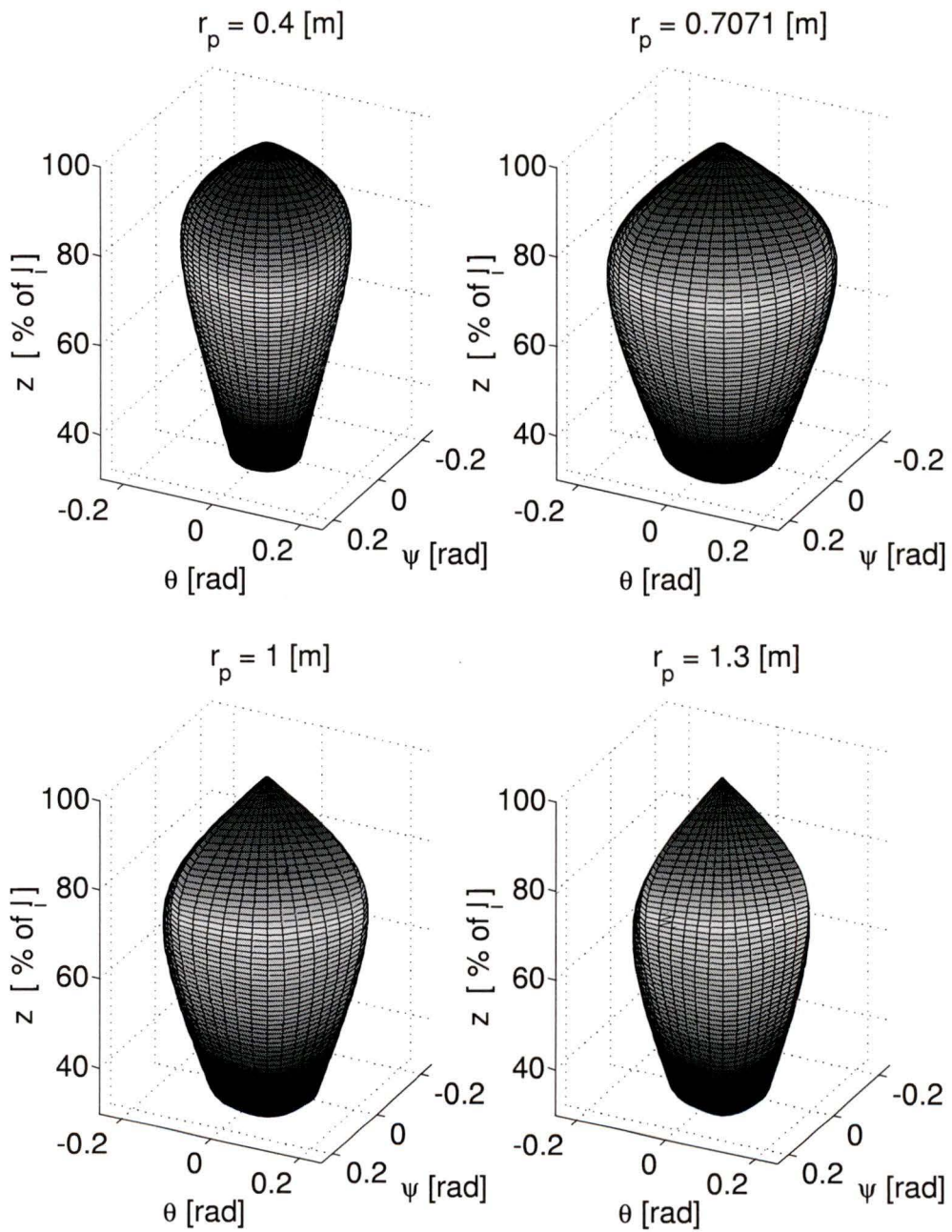


Figure 3.9: Comparison of the shape and size of the workspace when varying the platform radius ( $r_p$ ). The remaining parameters were set to:  $\alpha = -\beta = 120^\circ$ ,  $l_i = 1$  ( $i = 1, 2, 3$ ) and  $cond_{\max} = 5$ .

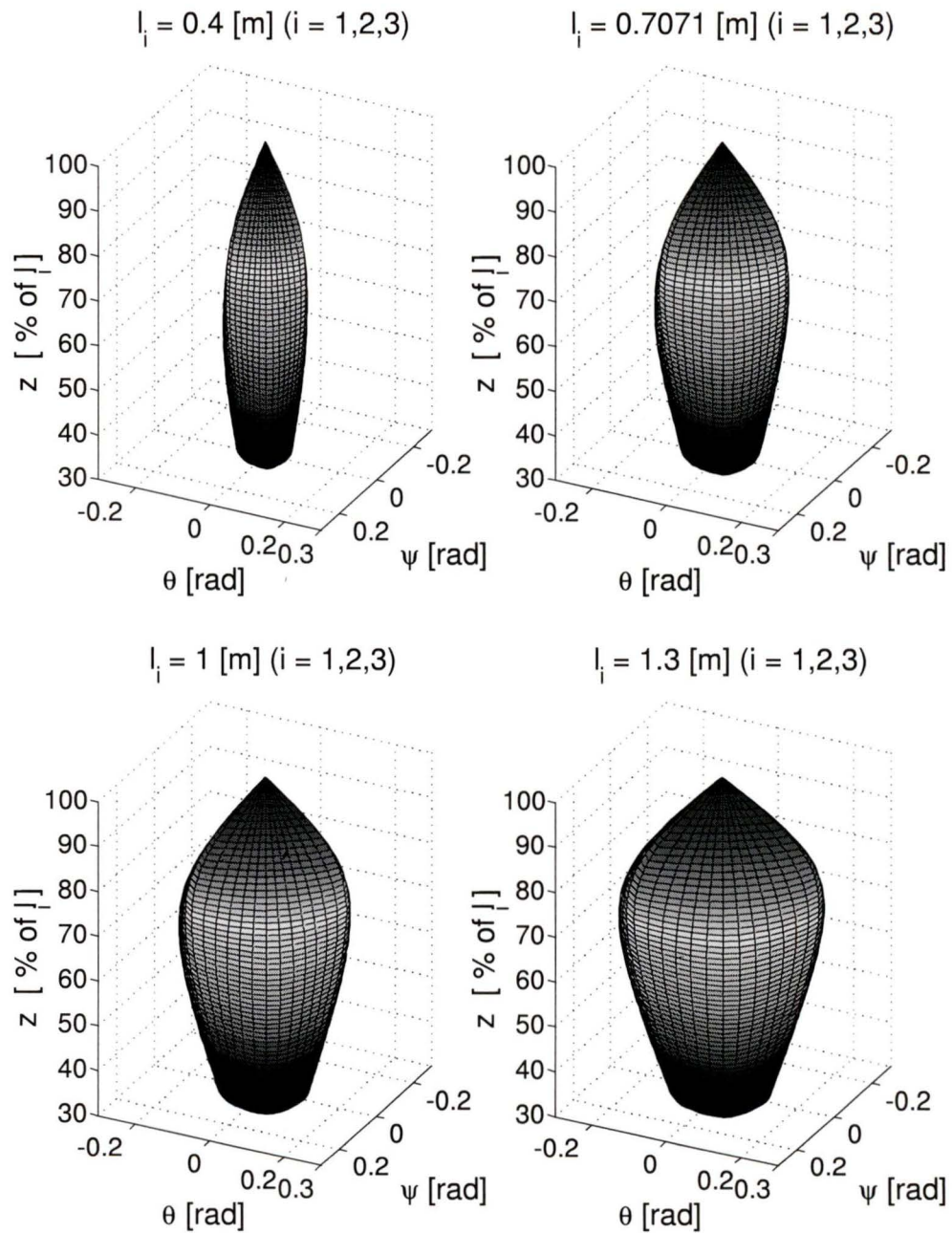


Figure 3.10: Comparison of the shape and size of the workspace when varying the leg length ( $l_i$ ). The remaining parameters were set to:  $\alpha = -\beta = 120^\circ$ ,  $r_p = 1$  and  $cond_{\max} = 5$ .

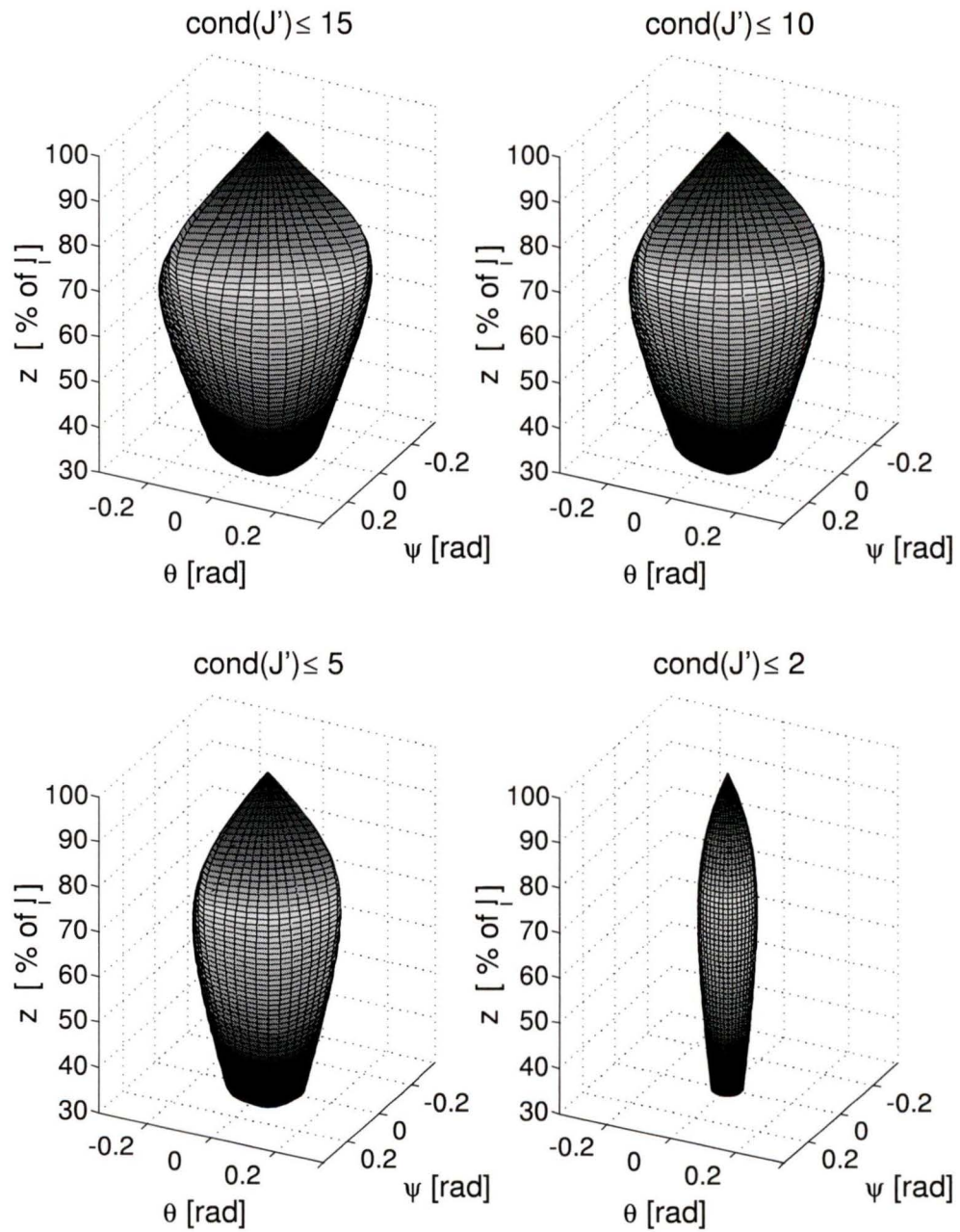


Figure 3.11: Comparison of the dexterous workspace for four different values of  $\text{cond}_{\max}$ .  $r_p = 1$ ,  $\alpha = -\beta = 120^\circ$  and  $l_i = 1$  ( $i = 1, 2, 3$ ).

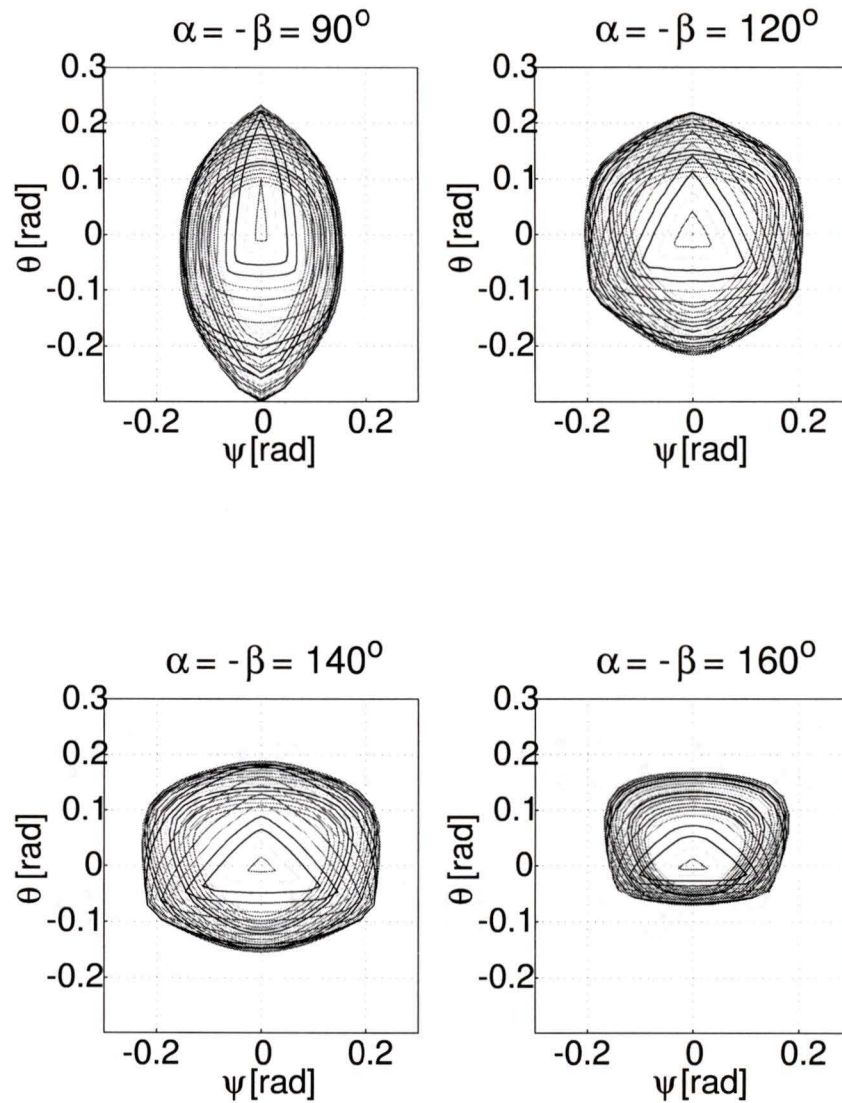


Figure 3.12: Contour plots of the comparison of the workspace for varying  $\alpha$  and  $\beta$ , for symmetrical configurations (*i.e.*  $\alpha = -\beta$ ).  $r_p = 1$ ,  $l_i = 1$  ( $i = 1, 2, 3$ ) and  $cond_{\max} = 5$ .

the same order of magnitude (the joint effort is similar to move in all three directions) in most of the workspace.

- two singular values are exactly equal when  $\psi = \theta = 0$ . They correspond to the tip/tilt rotations and, when the platform is horizontal, they are expected to be similar.
- the average of the singular values over the analyzed workspace increases with  $r_p$ . That is, the effort necessary to move the platform increases when the platform increases in radius, this can be confirmed with Figure 3.8.
- the curves that represent the singular values *vs.*  $r_p$  have a slope change around  $r_p = \sqrt{2}$ .

# Chapter 4

## Optimization

### 4.1 Goals of the optimization

When designing a mechanism for a particular application it is necessary to customize the design to best suit the task, *e.g.* find the platform radius that optimizes a particular mechanical characteristic such as dexterity (see for instance [9], [37]) or the size and quality of the workspace (see for instance [18]). In the present case, the principal goal is to optimize the architecture of the HVRam mechanism to make it suitable for the telescope application. We are interested in choosing the best architectural parameters that will give the best performance in terms of the kinematic performance variables discussed in Chapter 3.

### 4.2 Available variables

The layout of the introduced 3-DOF manipulator, and the pointing (2 dof orientation) and elevation tasks for which it is intended, confine the potential design variables to:

- $\{\alpha, \beta\}$ : the angles between the lines of action of the prismatic actuators 1 & 2 and 1 & 3, respectively
- $l_i$  for  $i = 1, 2, 3$ : the constant leg lengths
- $r_p$ : the mobile platform radius.

The above are illustrated in Figure 2.1 and represent a total of six potential parameters. Careful examination of the expressions derived for the  $x$  and  $y$  parasitic displacements (equations (2.18) and (2.19)) and consideration of the mechanics of the manipulator allows elimination of many of these parameters.

Equations (2.18) and (2.19) show that the  $x$  and  $y$  parasitic displacements are independent of the leg length  $l_i$ ,  $i = 1, 2, 3$ . Furthermore, these parasitic translational motions vary linearly with respect to  $r_p$ . Thus, by observation, in order to minimize parasitic motions,  $r_p$  should be as small as possible, considering practical design and implementation constraints. Therefore, for objectives involving minimum  $x$  and  $y$  parasitic motions  $l_i$  ( $i = 1, 2, 3$ ) and  $r_p$  need not be considered as design variables.

The only remaining parameters for the parasitic motion minimization are the angles,  $\alpha$  and  $\beta$ , between the lines of action of the prismatic actuators. These angles are the only relevant design variables (optimization variables) for objectives of parasitic motion minimization.

A systematic study of the influence of each variable on the condition number  $\kappa$  showed dependency on all of the potential design variables. However, the dexterity measure decreases, *i.e.* improves, monotonically when  $l_i$  is increased and the rest of the parameters are kept constant as seen in Figure 3.1. Thus it is irrelevant to use  $l_i$  as a design variable, since ultimately  $l_i$  will be limited by the application. The

remaining architectural parameters, *i.e.*,  $\alpha$ ,  $\beta$  and  $r_p$ , are the relevant design variables for dexterity optimizations.

## 4.3 Available functions

### 4.3.1 Parasitic Motion

For the telescope application, minimization of the magnitude of the parasitic motions would be desirable. That is, objectives could be based on the measure

$$\delta \equiv \delta(\psi, \theta, \alpha, \beta) = (x^2 + y^2)^{1/2} \quad (4.1)$$

The  $\phi$  rotation about the  $Z$  axis direction (the normal direction to the platform for the rotation representation of equation (2.3)) is neglected due to the fact that the secondary mirror of a telescope is axi-symmetrical, so that  $\phi$  rotations will not affect the image. Figure 4.1 illustrates the variation of  $\delta$  as a function of  $\psi$  and  $\theta$  for the example outlined in Table 2.1.

Minimization of the average over the intended tip/tilt work area ( $A_z$ ) at a particular  $z$  displacement can be set as an optimization objective. The reader must remember that the parasitic motions are all independent of  $z$  (equations (2.17) to (2.19)). Noting that  $\delta$  is a function of  $\alpha$  and  $\beta$ , yields the optimization goal of:

$$f^* = f(\{\alpha^*, \beta^*\}) = \min_{\alpha, \beta} [f(\alpha, \beta)] \quad (4.2)$$

where the \* superscript indicates values at the optimal point and

$$f \equiv \delta_{ave} = \frac{1}{A_z} \int_{A_z} \delta(\psi, \theta, \alpha, \beta) dA_z \quad (4.3)$$

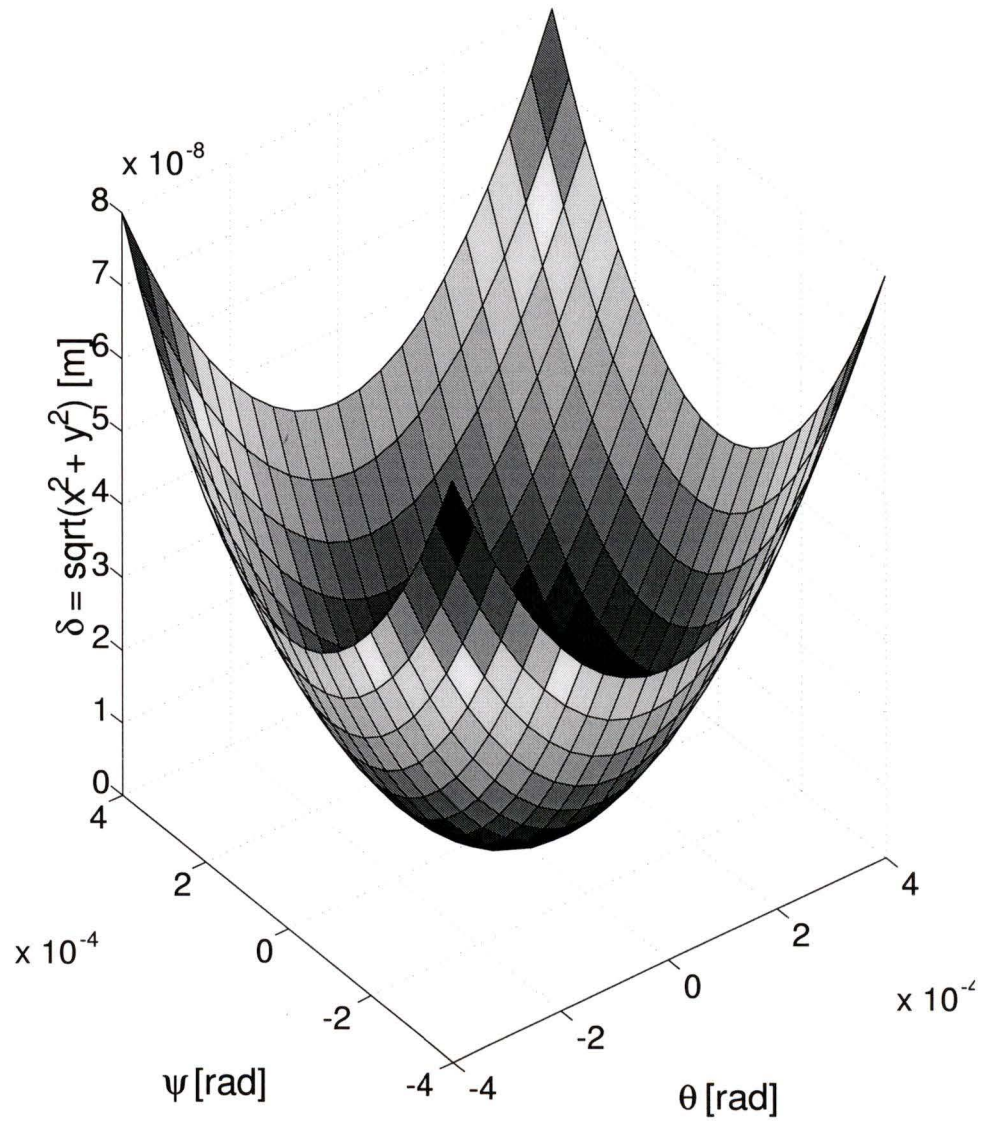


Figure 4.1: Total translational parasitic motion at  $z = 0.999$ ,  $\alpha = -\beta = 120^\circ$  and  $l_i = r_p = 1$ .

Utilizing an evenly spaced grid on  $\psi$  and  $\theta$  evaluation points to approximate the integral of equation (4.3) allows  $f$  to be expressed as:

$$\delta_{ave} \cong \frac{1}{nm} \sum_{\psi_i=\psi_1}^{\psi_n} \sum_{\theta_j=\theta_1}^{\theta_m} \delta(\psi_i, \theta_j, \alpha, \beta) \quad (4.4)$$

where  $m$  and  $n$  are the grid densities over  $\theta$  and  $\psi$ , respectively.

Minimizing the function in equation (4.4) is equivalent to minimizing equation (4.3) if the sample points  $\{\psi_i, \theta_j\}$  are dense enough and evenly distributed throughout the  $\{\psi, \theta\}$  work area. This will result in minimization of the average total magnitude of the parasitic motions.

An alternative to minimizing  $\delta_{ave}$  is to minimize the maximum value of  $\delta$ . The corresponding objective function in this case becomes

$$\begin{aligned} f &\equiv \delta_{mm} = \max_{A_z} (\delta(\psi, \theta, \alpha, \beta)) \\ &\cong \max_{\psi_i} \left( \max_{\theta_j} (\delta(\psi_i, \theta_j, \alpha, \beta)) \right) \end{aligned} \quad (4.5)$$

where  $\delta_{mm}$  after minimization corresponds to the mini-max value of  $\delta$ . The parasitic motions will not exceed  $\delta_{mm}$  for any  $\psi$  and  $\theta$  in the specified range.

Finally, depending on the intended application, minimization of the parasitic motion in a particular direction may be desired. Letting  $\rho$  be an angle representing the particular direction (measured in the horizontal plane with respect to the  $X$  direction) allows the definition of the measure

$$\delta_\rho = |x \cos \rho + y \sin \rho| \quad (4.6)$$

Substitution of  $\delta_\rho$  for  $\delta$  in equations (4.4) or (4.5) defines a suitable objective function for use in the minimization of the average or the maximum of  $\delta_\rho$ , respectively. For certain directions, *e.g.*,  $\rho = 0$  and  $\rho = \pi/2$ , consideration of the device geometry

allows knowledge of the corresponding  $\alpha^*$  and  $\beta^*$  values. These cases are very useful for testing the optimization routines.

### 4.3.2 Dexterity

To obtain the architecture with best dexterity over the analyzed workspace, the average of the condition number  $\kappa$  of the constrained Jacobian matrix, equation (2.24), can be used. Hence, by analogy with equation (4.4), the average of the condition number over the analyzed workspace can be obtained as follows:

$$f \equiv \kappa_{ave} \cong \frac{1}{nm} \sum_{\psi_i=\psi_1}^{\psi_n} \sum_{\theta_j=\theta_1}^{\theta_m} \kappa(\psi_i, \theta_j, \alpha, \beta) \quad (4.7)$$

In this case, for computational simplicity, the average of the condition number is made exclusively in a section of the workspace where  $z$  remains constant (despite the fact that  $\kappa$  is also a function  $z$ ).

In cases where it is desired to minimize the maximum condition number, it is possible to use an equation analogous to equation (4.5) to obtain the maximum condition number over the analyzed workspace ( $\kappa_{mm}$ ).

It is known that the condition number of a Jacobian matrix is frame and scale (unit) dependent. One must pick, as the reference point for the moving frame, the most significant point of the payload. In this case, the center of the moving payload (*i.e.* the center of the secondary mirror) was used. In this work, the choice of units, metres for distances and radians for rotations, lead to an evenly-weighted constrained Jacobian matrix, *i.e.* all the nine entries in the constrained Jacobian matrix have the same order of magnitude in most of the analyzed workspace.

## 4.4 Optimization methods and procedures

There exists a wide variety of optimization methods and procedures including analytical, graphical, experimental and numerical. Here, two methods were used, a graphical method that shows the behaviour of the analyzed properties when varying the architectural parameters and a numerical method to find the best solution to the given problem.

The quasi-Newton optimization algorithm of the Matlab Optimization Toolbox ([21]) was utilized to isolate optimal  $\alpha$ ,  $\beta$  and  $r_p$  values for the objective functions defined in the previous section. Quasi-Newton algorithms, however, do not ensure convergence to a global minimum for objectives with multiple minima. Search starts from many different initial variable values were therefore used to bolster confidence in the optimization results.

## 4.5 Graphical method results

The graphical method consisted of obtaining plots of the desired properties versus the design variables and visually inspecting them to locate the optimal points. This helps the designer to get close to the optimal solution, but has the disadvantages that only two variables can be used at a time and that it is computationally very expensive. In this section, surface plots, with respect to  $\alpha$  and  $\beta$ , of the  $x$  and average total parasitic motions ( $\delta_{ave}$ ) and the condition number ( $\kappa$ ) are shown. The algorithm used to obtain these plots is shown in Figure 4.2 and is described as follows.

The lower and upper limits of  $\alpha$  and  $\beta$  for the plots are first defined (typically  $90^\circ$  and  $-180^\circ$ , respectively) along with the fixed  $z$  coordinate where the  $\psi$ - $\theta$  grid

will be generated. Then mappings of all the parasitic motions  $x$ ,  $y$  and  $\phi$  (using the algorithm described in Section 2.3.2 and illustrated in Figure 2.3) and of the dexterity measure  $\kappa$  (using the algorithm described in Section 3.2.1 and illustrated in Figure 3.2) are obtained. Using equation (4.1) the total linear parasitic motion is obtained.

The results obtained in those procedures are then used to obtain the average over the workspace using equations (4.4) and (4.7) as well as the maximum using equation (4.5). These values are stored. The  $\alpha$  angle is incremented and the averages and maximums of the parasitic motions and dexterity are recalculated. The process continues until  $\alpha$  reaches its upper limit (typically  $180^\circ$ ). Then  $\alpha$  is reset to its lower limit and  $\beta$  is incremented. The process will continue until  $\beta$  has reached its upper limit (typically  $-90^\circ$ ).

Finally the results are plotted as three dimensional surfaces. A sample of the plots can be seen in Figures 4.3, 4.4 and 4.6. In order to locate the minimum point with greater accuracy, the results can also be plotted as two dimensional contour plots as seen in Figure 4.5.

Figures 4.4 to 4.6 show the behaviour of the averaged parameters *vs.*  $\alpha$  and  $\beta$  and it can be seen that the function are unimodal and symmetrical about  $\alpha = -\beta$  within the plotted range. The behaviour of the maximums, *i.e.*,  $x_{mm}$ ,  $\delta_{mm}$  and  $\kappa_{mm}$ , is similar to the averaged parameters.

Due to its computational cost the following sections will not involve the graphical method, the numerical optimization method will then be used.

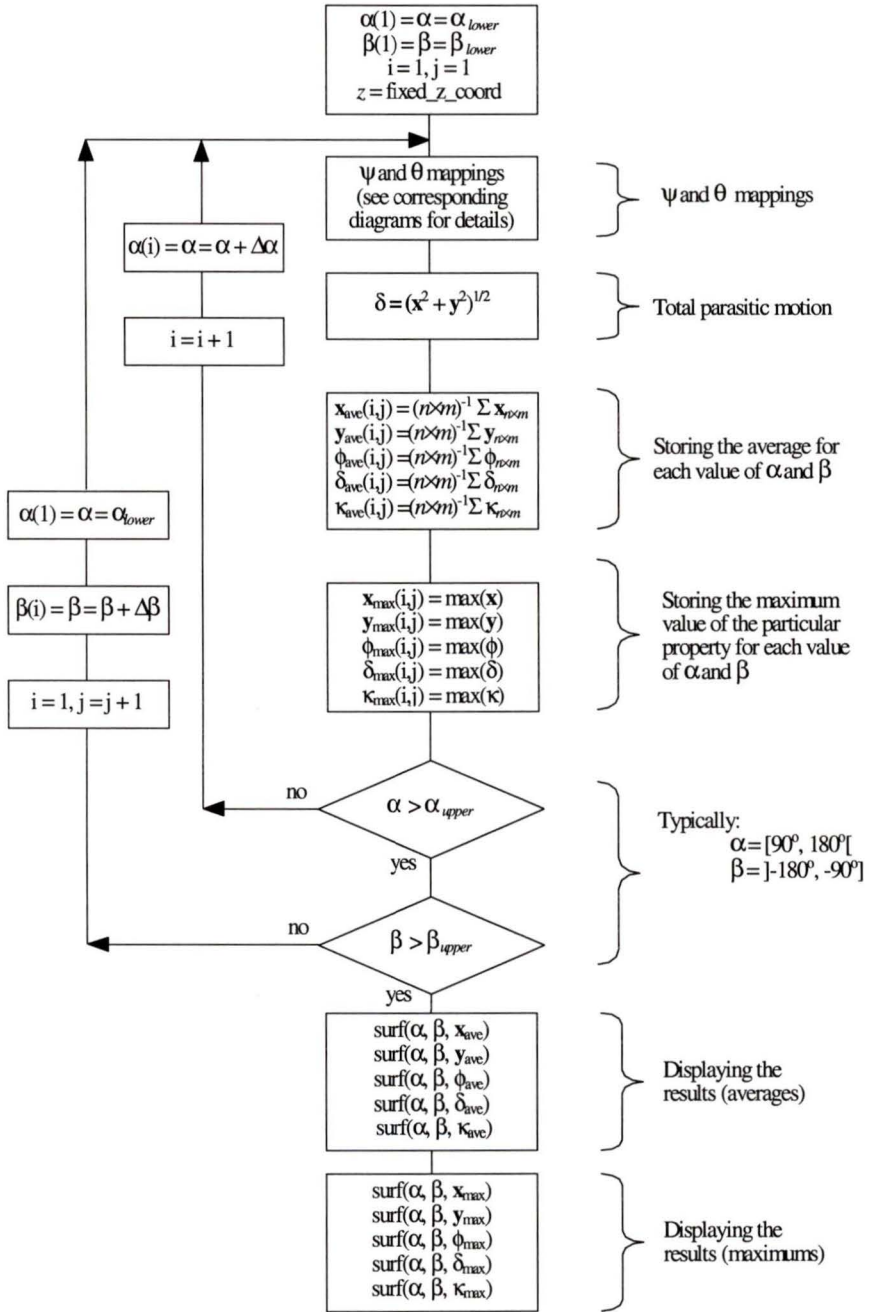


Figure 4.2: Flow diagram for the maps over the  $\alpha$ - $\beta$  plane.

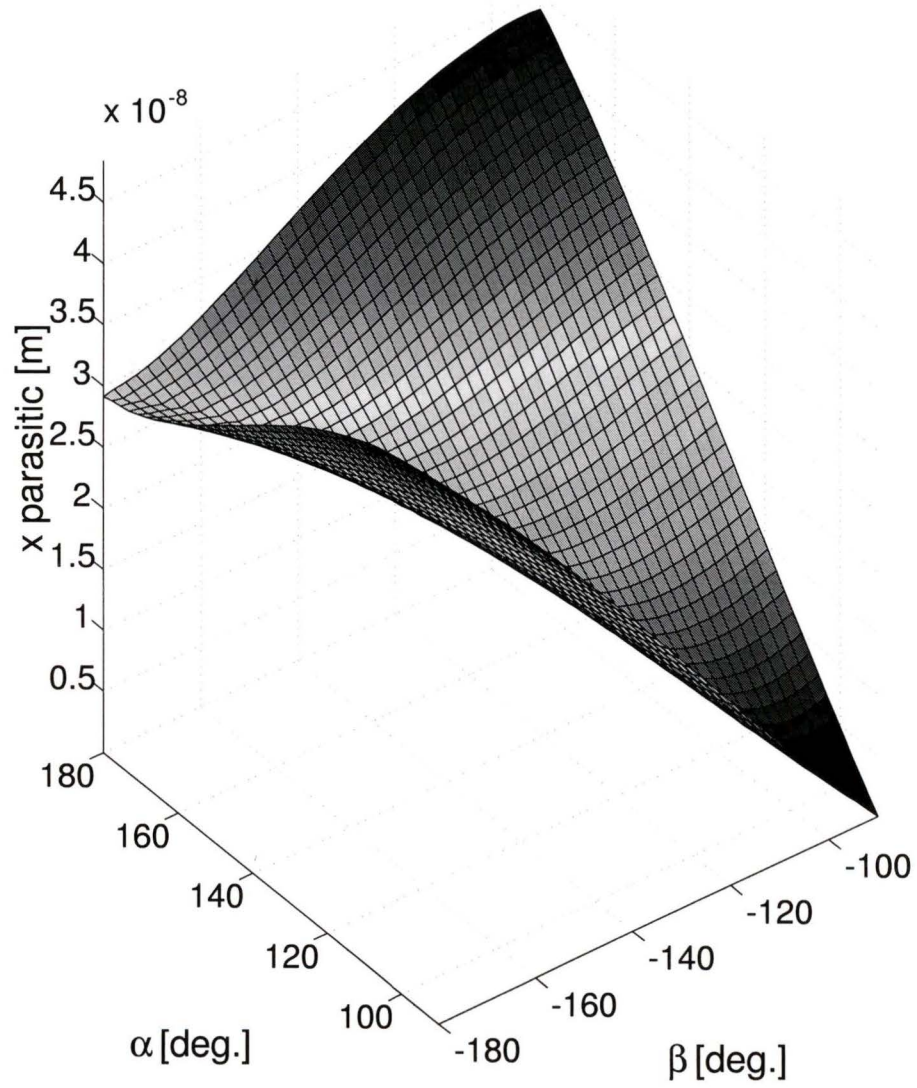


Figure 4.3: Average of the  $x$  parasitic motion ( $x_{ave}$ ) vs.  $\alpha$  and  $\beta$ .

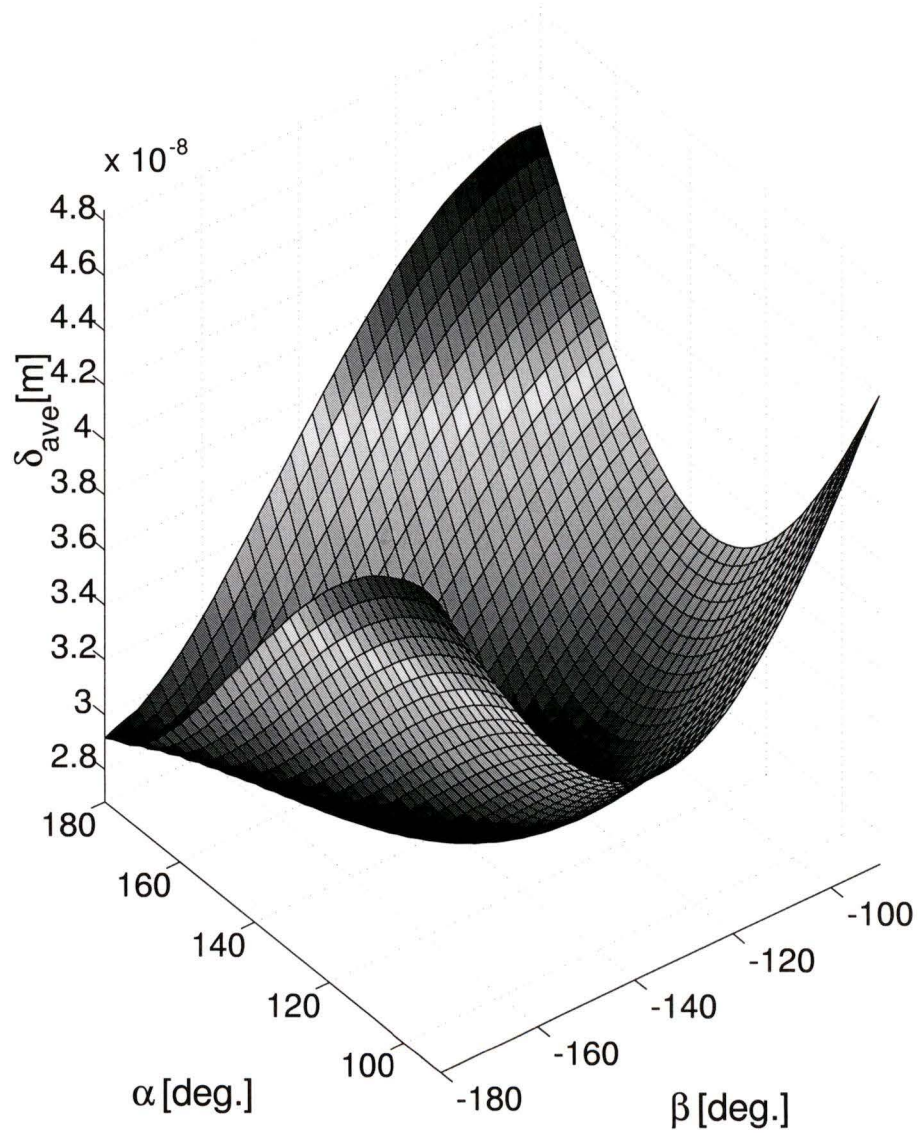


Figure 4.4: Average of the total translational parasitic motion ( $\delta_{ave}$ ) vs.  $\alpha$  and  $\beta$ .

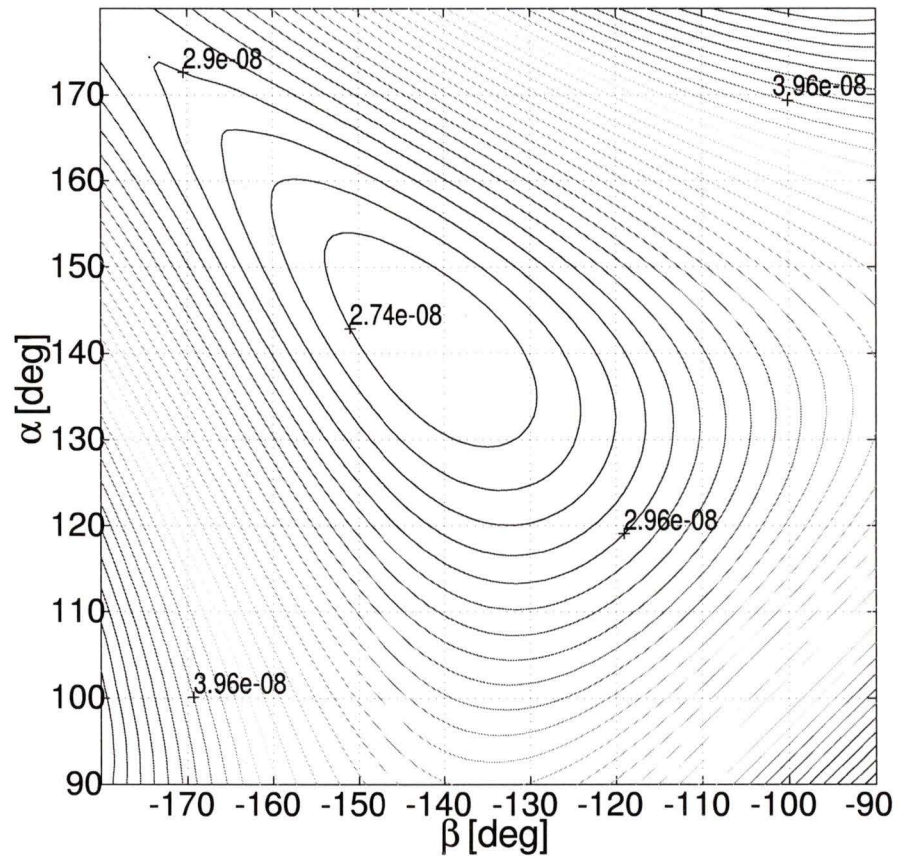


Figure 4.5: Contour plot of the average of the total parasitic motion ( $\delta_{ave}$ ) vs.  $\alpha$  and  $\beta$ .

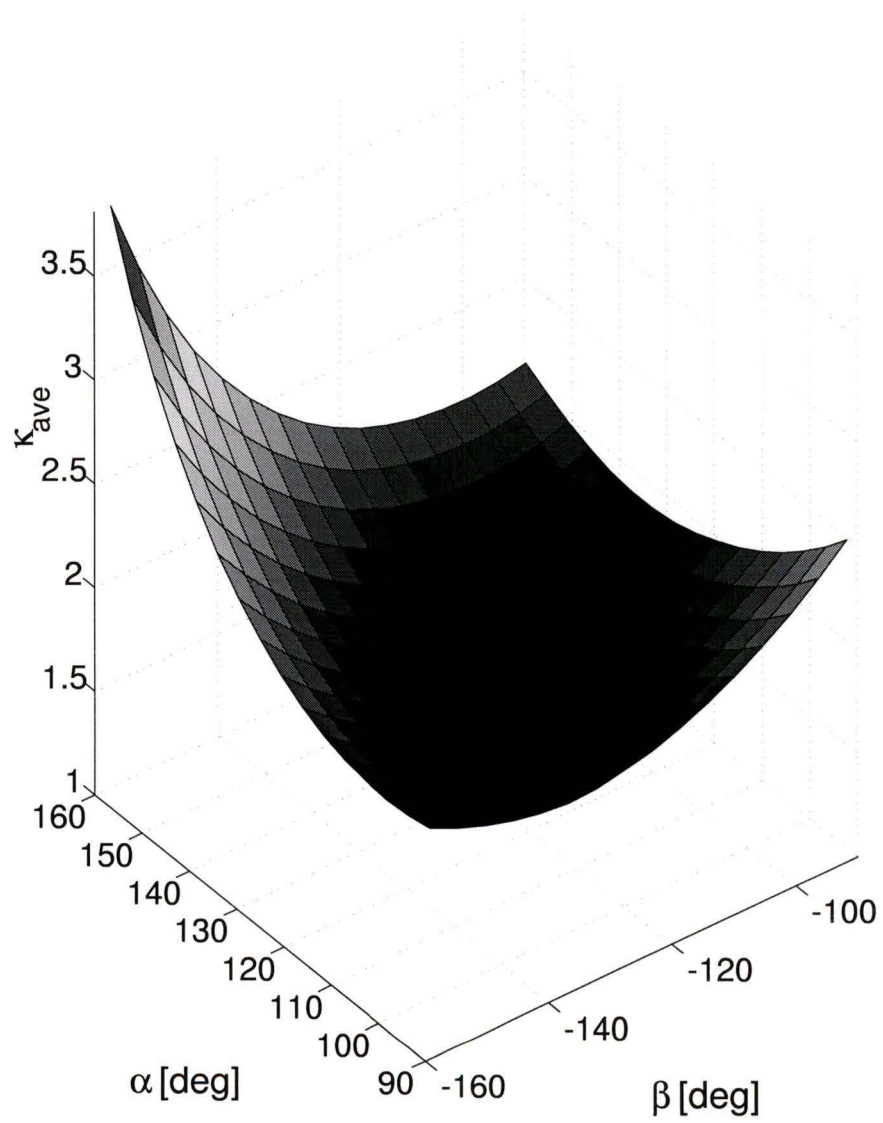


Figure 4.6: Dexterity measure,  $\kappa_{ave}$  vs.  $\alpha$  and  $\beta$ .

## 4.6 Numerical method results

### 4.6.1 Parasitic Motion

A  $21 \times 21$  grid of  $\psi$  and  $\theta$  values was used to approximate the integral inherent in the  $\delta_{ave}$  objective function of equation (4.4) and allow ample data for the isolation of the maximum total parasitic motion ( $\delta_{max}$ ) for the  $\delta_{mm}$  objective (equation (4.5)).

Table 2.1 summarizes the values of the  $z$  positions, leg lengths  $l_i$  and the platform radius  $r_p$  used for the analyzed example. As discussed previously, these values need not be considered design variables within the optimization of parasitic motion. However, reference values of these variables are relevant since they determine the reachable range of  $\psi$  and  $\theta$ . Using the values of  $z$ ,  $l_i$  and  $r_p$  shown in Table 2.1, the ranges of  $\psi$  and  $\theta$  (also reported in Table 2.1) were selected to represent close to the full available range of motion.

Optimization for objectives of minimizing specific direction, average and maximum parasitic motions were considered. Due to the extremely small magnitudes of the motions associated with the micro example, the values of the objective function were scaled by  $10^6$  within the corresponding optimizations and rescaled back for presentation in the results shown here.

#### Specific Direction Parasitic Motions

To serve as a test, a case of minimization of parasitic motion in a specific direction was considered. The example corresponds to  $\rho = 0^\circ$  where  $\rho$  is the specific direction.

For  $\rho = 0^\circ$ , we have  $\delta_\rho = x$ , and from Figure 2.1, it is apparent that the  $x$  parasitic motion is completely eliminated if  $\alpha = 90^\circ$  and  $\beta = -90^\circ$ . Substitution of  $c_\alpha = 0$  and

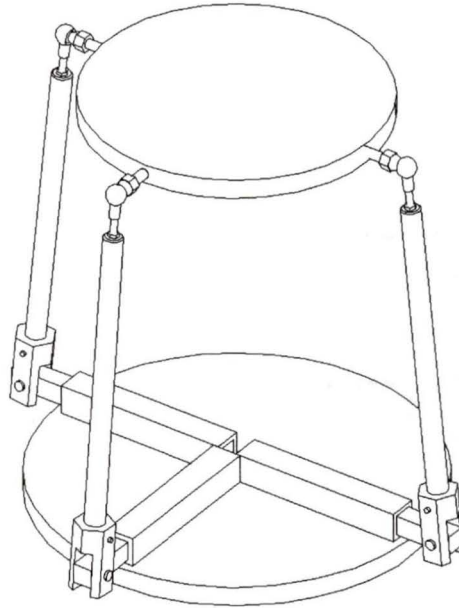


Figure 4.7: T configuration:  $\alpha = 90^\circ$  and  $\beta = -90^\circ$ .

$c_\beta = 0$  into equation (2.18) confirms this result. Figure 4.3 illustrates  $x_{ave}$  vs.  $\alpha$  and  $\beta$  and provides further confirmation that  $\alpha^* = 90^\circ$  and  $\beta^* = -90^\circ$ . Note, however, that  $y$  parasitic motions will still exist. Also note that the function is unimodal in the plotted region. Optimization cases for minimal  $x$  parasitic motion were considered. Several start point values were considered, all of which converged to  $\alpha^* = 90^\circ$  and  $\beta^* = -90^\circ$ , with  $f \approx 0$  m. These results agree with the expected values. Results for  $[\alpha, \beta]$  start points of  $[120, -120]$  and  $[150, -150]$  degrees are reported as cases 1 and 2 in Table 4.1. Figure 4.7 is a schematic of the architecture with  $\alpha = 90^\circ$  and  $\beta = -90^\circ$ .

Similar results were obtained for  $f \equiv \delta_{\rho_{ave}}$  and for  $f \equiv \delta_{\rho_{mm}}$ . Since the optimizations are converging to  $f^* = 0$ , this should be expected.

Case	obj.	vars.	start pt.	f(start) [ $\mu\text{m}$ ]	optimum vars.	f* [ $\mu\text{m}$ ]	steps
1	$x$	$[\alpha, \beta]$	[120, -120]	14.57	[90, -90]	$1.264 \times 10^{-16}$	64
2	$x$	$[\alpha, \beta]$	[150, -150]	25.23	[90, -90]	$1.264 \times 10^{-16}$	174
3	$\delta_{ave}$	$[\alpha, \beta]$	[120, -120]	29.33	[141.20, -141.20]	26.81	94
4	$\delta_{ave}$	$[\alpha, \beta]$	[90, -90]	43.90	[141.23, -141.23]	26.81	62
5	$\delta_{mm}$	$[\alpha, \beta]$	[150, -150]	69.28	[131.84, -131.78]	53.33	117
6	$\delta_{mm}$	$[\alpha, \beta]$	[120, -120]	80.00	[131.84, -131.79]	53.33	98

Table 4.1: Parasitic motion optimization (MICRO case).

Case	obj.	vars.	start pt.	f(start) [mm]	optimum vars.	f* [mm]	steps
1	$x$	$[\alpha, \beta]$	[120, -120]	3.640	[90, -90]	$1.345 \times 10^{-15}$	58
2	$x$	$[\alpha, \beta]$	[150, -150]	6.294	[90, -90]	$1.345 \times 10^{-15}$	59
3	$\delta_{ave}$	$[\alpha, \beta]$	[120, -120]	7.290	[140.96, -140.96]	6.675	36
4	$\delta_{ave}$	$[\alpha, \beta]$	[90, -90]	10.89	[140.98, -140.98]	6.675	74
5	$\delta_{mm}$	$[\alpha, \beta]$	[150, -150]	17.26	[131.64, -131.64]	13.25	126
6	$\delta_{mm}$	$[\alpha, \beta]$	[120, -120]	19.73	[131.64, -131.64]	13.25	120

Table 4.2: Parasitic motion optimization (MACRO case).

### Average Parasitic Motion, $\mathbf{f} = \delta_{ave}$

Optimizations of the average parasitic motion objective function given by equation (4.4) were considered. Again, various start values for  $\alpha$  and  $\beta$  were used. Results for two different start points are reported as cases 3 and 4 in Table 4.1, both converging to the same symmetrical configuration ( $\alpha^* = -\beta^* = 141.2^\circ$ ) with  $f^*$  on the order of 30 nanometers.

For the macro example, the searches consistently converged to symmetrical configurations ( $\alpha^* = \beta^* = 140.9^\circ$ ) with  $f^*$  on the order of 6.6 mm. Results for  $[\alpha, \beta]$  start points of [120, -120] and [90, -90] degrees are reported as cases 3 and 4 in Table 4.2.

Case	obj.	vars.	start pt. vars.	f(start)	optimum vars.	f*	steps
1	$\kappa_{ave}$	$[\alpha, \beta]$	[170, -170]	8.140	[120.1, -120.1]	1.639	22
2	$\kappa_{ave}$	$[\alpha, \beta]$	[90, -90]	2.550	[120.1, -120.1]	1.639	32
3	$\kappa_{ave}$	$[r_p]$	[1]	1.639	[1.278]	1.494	12
4	$\kappa_{ave}$	$[\alpha, \beta, r_p]$	[120, -120, 1]	1.639	[120, -120, 1.278]	1.494	67
5	$\kappa_{ave}$	$[\alpha, \beta, r_p]$	[120, -120, 3]	5.271	[120, -120, 1.278]	1.494	79
6	$\kappa_{mm}$	$[\alpha, \beta]$	[150, -150]	3.031	[127, -127]	2.001	68
7	$\kappa_{mm}$	$[\alpha, \beta]$	[90, -90]	2.851	[127, -127]	2.001	63
8	$\kappa_{mm}$	$[r_p]$	[1]	2.026	[1.006]	2.026	9
9	$\kappa_{mm}$	$[\alpha, \beta, r_p]$	[120, -120, 1]	2.026	[127, -127, 0.991]	2.001	63
10	$\kappa_{mm}$	$[\alpha, \beta, r_p]$	[120, -120, 3]	100.1	[127, -127, 0.991]	2.001	148

Table 4.3: Dexterity measure optimization (MICRO case).

### Mini-max Parasitic Motion, $f = \delta_{mm}$

Optimizations considering the mini-max parasitic motion objective function given by equation (4.5) were considered. Again different start values for  $\alpha$  and  $\beta$  were considered, all converging to  $\alpha^* = -\beta^* = 131.8^\circ$  with  $f^*$  on the order of 50 nanometers. Two cases are reported as cases 5 and 6 in Table 4.1.

Cases 5 and 6 in Table 4.2 report two optimization runs for the macro example, the considered searches consistently converged to  $\alpha^* = \beta^* = 131.6^\circ$  with  $f^*$  on the order of 10 mm.

As a check, the maximum  $\delta$  values (denoted  $\delta_{max}$ ) present in the parasitic motions corresponding to the architecture found for the  $\delta_{ave}$  objective can be compared with the  $\delta_{mm}$  found using the mini-max objective. The  $\delta_{max}$  for the micro example ( $f = \delta_{ave}$ ) is  $62.37 \times 10^{-9}$  m. The  $\delta_{max}$  for the macro example ( $f = \delta_{ave}$ ) is  $15.5 \times 10^{-3}$  m. These values are both 17% higher than the optimum  $\delta_{mm}$  values.

## 4.6.2 Dexterity

The same grid density ( $21 \times 21$ ) was used for the dexterity optimizations. It is possible to see in Figure 4.8 that  $\kappa_{ave}$  exhibits a minimum within the plotted range of  $r_p$  values. That is why the searches including  $r_p$  as a search variable were limited to  $0.5 \leq r_p \leq 3$ . These limits were arbitrarily fixed since giving some extra margin since the co-relation with the other optimization variables was unknown. Any variable which was fixed during a particular optimization was set at the value given in Table 2.1.

### Average of the Condition Number, $f = \kappa_{ave}$

Optimizations of the average of the condition number objective function given in equation (4.7) were considered next. Again, various start values for  $\alpha$  and  $\beta$  were used. For the example considered, the searches consistently converged to  $\alpha^* = -\beta^* = 120^\circ$  and two of these are reported as cases 1 and 2 in Table 4.3.

Case 3 presents an optimization using only  $r_p$  as search variable. For the given parameters, the minimum was found to be at  $r_p = 1.278$  m as seen in Figure 4.8.

Using  $\alpha$ ,  $\beta$  and  $r_p$  as search variables resulted in values reported as cases 4 and 5. In both cases, the minimum point is found to have symmetrical  $\alpha^*$  and  $\beta^*$  angles of  $120^\circ$  and  $-120^\circ$  respectively, with  $r_p = 1.278$  and  $\kappa_{ave} = 1.494$ . It can be noticed that all of the optimizations of  $\kappa_{ave}$  converged to the same optimal point independently of the search variables or starting points.

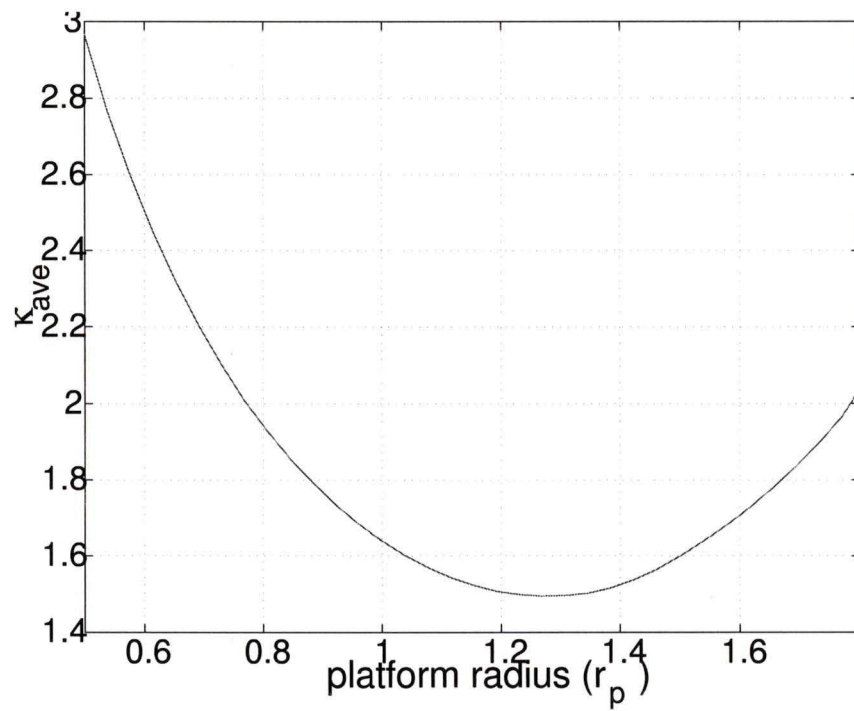


Figure 4.8: Condition number ( $\kappa$ ) vs.  $r_p$ , with  $z = 0.999 \cdot l_i$  and  $\alpha = -\beta = 120^\circ$ .

**Mini-max of the Condition Number,  $f = \kappa_{mm}$** 

Optimizations considering the maximum of the condition number objective function were considered. Of the various start values for  $\alpha$  and  $\beta$  that were used, Table 4.3 shows two:  $[150, -150]$  and  $[90, -90]$  degrees, reported as cases 6 and 7, respectively. Both of these cases converged to  $\alpha^* = -\beta^* = 127^\circ$  and  $\kappa_{mm} = 2.001$ . In case 8 of Table 4.3, only  $r_p$  was used as a search variable and the minimum was found to be at  $r_p^* = 1.006$  m, but when  $\alpha$ ,  $\beta$  and  $r_p$  were used as search variables (*e.g.* cases 9 and 10) the searches converged to a platform radius  $r_p^* = 0.991$  m with  $\alpha^* = -\beta^* = 127^\circ$ .

# Chapter 5

## Static Force Analysis

### 5.1 Definitions

A static force analysis constitutes a preliminary analysis of the structure of the mechanism. That is, obtaining equations that relate the actuator and/or the structural forces to a generalized force applied at the moving platform. This problem is usually called the *inverse force solution* and is expressed as follows:

$$\boldsymbol{\tau}_{n \times 1} = [\ast]_{n \times m} \mathbf{F}_{m \times 1} \quad (5.1)$$

where  $\boldsymbol{\tau} \in \mathfrak{R}^n$  is the vector of joint torques/moments,  $\mathbf{F} \in \mathfrak{R}^m$  is the generalized force applied to the moving platform and  $[\ast]_{n \times m}$  is a matrix operator that maps the generalized force into the actuator forces and is a function of the architecture and pose of the manipulator.

The *forward force solution* is defined as the solution of the problem of obtaining a *generalized force* vector (*i.e.* a force and a moment,  $\mathbf{F}_{ref_{6 \times 1}}$ ) knowing the actuated joint forces and/or moments. In the present case, the mechanism has only three

actuated prismatic joints. The remaining joints, shown in Figure 1.4, are passive. This means that this is a non-square problem, *i.e.* there are more elements in the generalized force vector than joint variables, or in mathematical terms:

$$\mathbf{F}_{ref_{6 \times 1}} = \begin{Bmatrix} \mathbf{f}_{3 \times 1} \\ \mathbf{m}_{0_{3 \times 1}} \end{Bmatrix} = [*]_{6 \times 3} \begin{Bmatrix} \tau_{1_1} \\ \tau_{1_2} \\ \tau_{1_3} \end{Bmatrix}_{3 \times 1} \quad (5.2)$$

where  $\mathbf{f}_{3 \times 1}$  corresponds to the force elements while  $\mathbf{m}_{0_{3 \times 1}}$  corresponds to the moment elements and  $[*]_{6 \times 3}$  is a six by three operator that maps the three actuator forces  $\tau_{1i}$  ( $i = 1, 2, 3$ ) to the generalized force. The first subindex in  $\tau$  refers to the joint number. In the case of the HVRam, the actuated prismatic joint is the joint number one.

## 5.2 Solution of the joint forces through power considerations

Now let us obtain the mapping operator mentioned in the previous section (equation (5.2)) through power considerations. Using conservation of power [3] (neglecting all friction forces) one obtains [31]:

$$\boldsymbol{\tau}^T \dot{\mathbf{s}} = \mathbf{F}^T (\mathbf{E} \dot{\mathbf{x}}) \quad (5.3)$$

where  $\boldsymbol{\tau} = [\tau_1, \tau_2, \tau_3]^T$  are the joint forces,  $\mathbf{F}$  is the generalized force applied at the centre of the moving platform and  $\mathbf{E}$  is a matrix that transforms the last three elements of  $\dot{\mathbf{x}}$  (namely  $\dot{\Theta} = [\dot{\psi}, \dot{\theta}, \dot{\phi}]^T$ ) to angular velocities expressed in a frame located at the centre of the moving platform but oriented as the inertial frame (namely

$\Omega = [\omega_x, \omega_y, \omega_z]^T$  [13].  $\mathbf{E}$  is expressed as follows:

$$\mathbf{E} = \begin{bmatrix} \mathbf{I}_{3 \times 3} & \mathbf{0}_{3 \times 3} \\ \mathbf{0}_{3 \times 3} & \mathbf{E}'_{3 \times 3} \end{bmatrix}$$

where

$$\mathbf{E}' = \begin{bmatrix} c_\theta & 0 & c_\psi s_\theta \\ 0 & 1 & -s_\psi \\ s_\theta & 0 & c_\psi c_\theta \end{bmatrix}$$

and is obtained from the fact that  $\Omega = \mathbf{E}'\dot{\Theta}$  and that the angular velocities  $\Omega$  can be solved for from [13]:

$$\dot{\mathbf{T}}\mathbf{T}^T = \begin{bmatrix} 0 & -\Omega_z & \Omega_y \\ \Omega_z & 0 & -\Omega_x \\ -\Omega_y & \Omega_x & 0 \end{bmatrix}$$

Substituting  $\dot{\mathbf{s}} = \mathbf{J}\dot{\mathbf{x}}$  (equation (2.20)) into equation (5.3) yields:

$$\boldsymbol{\tau}^T \mathbf{J}\dot{\mathbf{x}} = \mathbf{F}^T \mathbf{E}\dot{\mathbf{x}}$$

Substituting  $\dot{\mathbf{x}} = \mathbf{P}\dot{\mathbf{x}}'$  (equation (2.22)):

$$\boldsymbol{\tau}^T \mathbf{J}\mathbf{P}\dot{\mathbf{x}}' = \mathbf{F}^T \mathbf{E}\mathbf{P}\dot{\mathbf{x}}'$$

In order for this to be true for all  $\dot{\mathbf{x}}'$ :

$$\boldsymbol{\tau}^T \mathbf{J}\mathbf{P} = \mathbf{F}^T \mathbf{E}\mathbf{P}$$

which, when transposed, yields:

$$\mathbf{P}^T \mathbf{J}^T \boldsymbol{\tau} = \mathbf{P}^T \mathbf{E}^T \mathbf{F}$$

Solving the previous equation for the torques ( $\boldsymbol{\tau}$ ) yields:

$$\boldsymbol{\tau} = (\mathbf{P}^T \mathbf{J}^T)^{-1} \mathbf{P}^T \mathbf{E}^T \mathbf{F} = (\mathbf{J}^T)^{-1} \mathbf{P}^T \mathbf{E}^T \mathbf{F} \quad (5.4)$$

Equation (5.4) represents the *inverse force solution*, and applying it to the HVRam mechanism leads to the following considerations:

- $\boldsymbol{\tau}$  is a three dimensional vector containing the forces of the actuators 1, 2 and 3, respectively.
- the generalized force  $\mathbf{F}$  is a six dimensional vector formed by the applied force and applied moment with respect to the origin of the frame where  $\mathbf{F}$  is expressed.

### 5.3 Solution of the joint and structural forces via screw formulation

By introducing a *dummy* (structural) rotational joint aligned with each one of the prismatic joints, as shown in Figure 5.1 for one of the kinematic chains, the problem becomes a square problem (six actuators —3 prismatic and 3 rotational structural joints— and six components in the generalized force). This is not just an easy way to fix the non-square problem, but it will help in further studies to take into account the rotational stiffness of the prismatic joint needed for structural (stiffness) analysis. For this reason it will be called the structural joint and it can be modeled as a zero pitch screw  $\mathcal{S}_{st_i}$ , where  $i$  is the branch number going from 1 to 3. Figure 5.1 illustrates the dummy joint for a branch  $i$ .

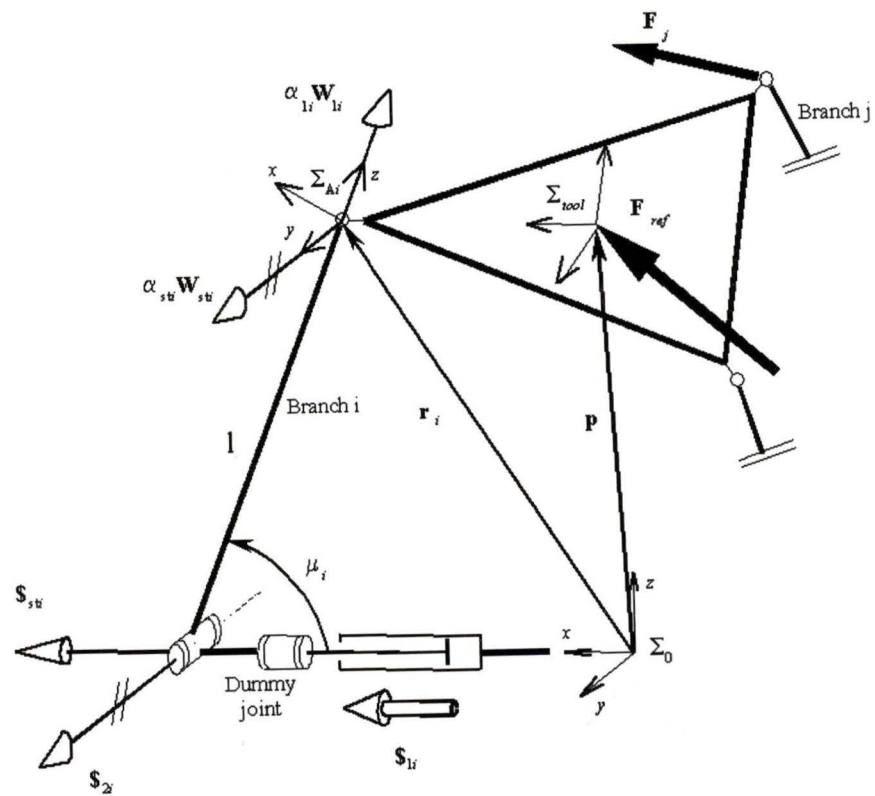


Figure 5.1: Frames, screws and forces represented for branch  $i$ .

Equation (5.2) then becomes:

$$\mathbf{F}_{ref_{6 \times 1}} = \begin{Bmatrix} \mathbf{f}_{3 \times 1} \\ \mathbf{m}_{o_{3 \times 1}} \end{Bmatrix} = [*]_{6 \times 6} \begin{Bmatrix} \tau_{1_1} \\ \tau_{st_1} \\ \tau_{1_2} \\ \tau_{st_2} \\ \tau_{1_3} \\ \tau_{st_3} \end{Bmatrix}_{6 \times 1} \quad (5.5)$$

where the operator  $[*]_{6 \times 6}$  is a linear operator.

The generalized force  $\mathbf{F}_{ref}$  must be equilibrated by intensities acting on the reciprocal screws. That is,

$$\mathbf{F}_{ref} + \sum_{i=1}^3 (\alpha_{1_i} \mathbf{W}_{1_i} + \alpha_{st_i} \mathbf{W}_{st_i}) = 0 \quad (5.6)$$

Note that  $\alpha_{1_i} \mathbf{W}_{1_i} + \alpha_{st_i} \mathbf{W}_{st_i} = \mathbf{F}_i$  is the force sustained by the  $i$ -th branch.. Therefore  $\mathbf{F}_{ref}$  can be expressed as

$$\mathbf{F}_{ref} = - \sum_{i=1}^3 (\alpha_{1_i} \mathbf{W}_{1_i} + \alpha_{st_i} \mathbf{W}_{st_i}) = - \sum_{i=1}^3 \mathbf{F}_i \quad (5.7)$$

where  $\mathbf{F}_i$  are the resultant generalized forces that can be sustained at points  $A_i$  (the centres of the spherical joints attached to the moving platform),  $\mathbf{W}_{1_i}$  corresponds to the screw coordinates of a unit *reciprocal screw*<sup>1</sup> associated with the prismatic joint<sup>2</sup> (joint 1) and  $\alpha_{1_i}$  is its corresponding wrench intensity (magnitude), and finally

---

<sup>1</sup>If a body is constrained to move about an instantaneous screw axis,  $\mathcal{S}$ , a wrench acting on a screw  $\mathcal{S}'$  can contribute nothing to the rate at which work is being done on the body. In such circumstance  $\mathcal{S}$  and  $\mathcal{S}'$  are said to be *reciprocal screws*. [22]

<sup>2</sup>An *associated reciprocal screw* to joint  $i$  is the one reciprocal to all joints in that kinematic chain but joint  $i$ .

$\mathbf{W}_{st_i}$  is the screw coordinates of a unit reciprocal screw associated with the structural rotational joint with  $\alpha_{st_i}$  being its wrench intensity.

Note that  $\mathbf{W}_{1_i}$  and  $\mathbf{W}_{st_i}$  must be zero pitch screws intersecting  $A_i$  in order to be reciprocal to the passive spherical joint at  $A_i$ . Also note that for a zero pitch screw to be reciprocal to another zero pitch screw the two screws must intersect. Furthermore note that for a zero pitch screw to be reciprocal to a prismatic joint (an infinite pitch screw) the directions of the two screws must be perpendicular [22]. Therefore,  $\mathbf{W}_{1_i}$  must intersect the common point of  $\mathcal{S}_{st_i}$  and  $\mathcal{S}_{2_i}$  (the intersection point of the dummy and second joint) and  $\mathbf{W}_{st_i}$  must be parallel to  $\mathcal{S}_{2_i}$  (thereby intersecting joint two at infinity and being normal to the prismatic joint ( $\mathcal{S}_{1_i}$ )). The above completely defines the properties of  $\mathbf{W}_{1_i}$  and  $\mathbf{W}_{st_i}$  and will allow their corresponding screw coordinates to be found.

It should be noticed that  $\mathbf{F}_i$  is a pure force applied at  $A_i$  since  $\mathbf{F}_i = \alpha_{1_i}\mathbf{W}_{1_i} + \alpha_{st_i}\mathbf{W}_{st_i}$  is a combination of two zero pitch screw quantities intersecting  $A_i$ . Physically this property is obvious since a spherical joint cannot transmit any moment (*if frictional forces are neglected*). Also it should be noticed that the properties of  $\mathbf{W}_{1_i}$  define the properties of the force that can be applied by chain  $i$  and  $\mathbf{W}_{st_i}$  define the properties of the forces that can be sustained by chain  $i$  (a pencil of forces centered at  $A_i$  lying in the plane defined by the directions of  $\mathbf{W}_{1_i}$  and  $\mathbf{W}_{st_i}$  [22]).

Rewriting (5.7) in matrix form yields

$$\mathbf{F}_{ref} = - \left[ \cdots \quad \mathbf{W}_{1_i} \quad \mathbf{W}_{st_i} \quad \cdots \right] \left\{ \begin{array}{c} \vdots \\ \alpha_{1_i} \\ \alpha_{st_i} \\ \vdots \end{array} \right\} \quad (5.8)$$

Let  $\mathbf{V}_{ref}$  be the screw quantity defining the velocity of the platform.

$$\mathbf{V}_{ref} = \left\{ \begin{array}{c} \boldsymbol{\omega} \\ \mathbf{V}_{oref} \end{array} \right\}_i = \sum_k \mathbb{S}_{k_i} \cdot \dot{q}_{k_i} \quad (5.9)$$

where  $\boldsymbol{\omega}$  is the angular velocity and  $\mathbf{V}_{oref}$  is the linear velocity of a point attached to the platform and coincident with the reference origin.  $\mathbb{S}_k$  is the normalized screw corresponding to joint  $k$ ,  $\dot{q}_{k_i}$  corresponds to joint rate of the same joint and  $k \in \{\text{kinematic and structural joints}\}$ . The  $i$  subindexes in equation (5.9) correspond to the branch number ( $i = 1, 2, 3$ ).

Defining  $\otimes$  as the reciprocal product operator of two screw quantities<sup>3</sup>, we find that the rate of work done by the actuated and the structural joint must be equal to the rate of work done by the sustained generalized force  $\mathbf{F}_i$ :

$$\mathbf{F}_i \otimes \mathbf{V}_{ref} = \tau_{1_i} \cdot \dot{q}_{1_i} + \tau_{st_i} \cdot \dot{q}_{st_i} \quad (5.10)$$

Substituting (5.7) and (5.9) into (5.10):

$$(\alpha_{1_i} \mathbf{W}_{1_i} + \alpha_{st_i} \mathbf{W}_{st_i}) \otimes \left( \sum_k \mathbb{S}_{k_i} \cdot \dot{q}_{k_i} \right) = \tau_{1_i} \cdot \dot{q}_{1_i} + \tau_{st_i} \cdot \dot{q}_{st_i} \quad (5.11)$$

Since  $\mathbf{F}_i$  only load the actuated and structural joints ( $\mathbb{S}_{1_i}$  and  $\mathbb{S}_{st_i}$ ), *i.e.*  $\mathbf{W}_{1_i}$  and  $\mathbf{W}_{st_i}$  are reciprocal to all of the passive joints, we have

$$\tau_{1_i} \cdot \dot{q}_{1_i} + \tau_{st_i} \cdot \dot{q}_{st_i} = (\alpha_{1_i} \mathbf{W}_{1_i} \otimes \mathbb{S}_{1_i} \cdot \dot{q}_{1_i}) + (\alpha_{st_i} \mathbf{W}_{st_i} \otimes \mathbb{S}_{st_i} \cdot \dot{q}_{st_i}) \quad (5.12)$$

---

<sup>3</sup>The reciprocal product ( $\otimes$ ) of two screw quantities  $\mathbf{S}_1 = \left\{ \begin{array}{c} \mathbf{s}_1 \\ \mathbf{s}_{o1} \end{array} \right\}$  and  $\mathbf{S}_2 = \left\{ \begin{array}{c} \mathbf{s}_2 \\ \mathbf{s}_{o2} \end{array} \right\}$  is a scalar product defined as follows:  $\mathbf{S}_1 \otimes \mathbf{S}_2 = \mathbf{s}_1 \cdot \mathbf{s}_{o2} + \mathbf{s}_{o1} \cdot \mathbf{s}_2$ . If  $\mathbf{S}_1$  represents a velocity of a body and  $\mathbf{S}_2$  a force system acting on a body,  $\mathbf{S}_1 \otimes \mathbf{S}_2$  quantifies the corresponding rate of work being done.

Rewriting in matrix form:

$$\left\{ \begin{array}{cc} \tau_{1i} & \tau_{st_i} \end{array} \right\}_i \left\{ \begin{array}{c} \dot{q}_1 \\ \dot{q}_{st_i} \end{array} \right\}_i = \left\{ \begin{array}{cc} \alpha_{1i} \mathbf{W}_{1i} \otimes \$_{1i} & \alpha_{st_i} \mathbf{W}_{st_i} \otimes \$_{st_i} \end{array} \right\}_i \left\{ \begin{array}{c} \dot{q}_1 \\ \dot{q}_{st_i} \end{array} \right\}_i \quad (5.13)$$

a property true for all  $\left\{ \begin{array}{c} \dot{q}_1 \\ \dot{q}_{st_i} \end{array} \right\}_i$ , this yields

$$\tau_{1i} = \alpha_{1i} \mathbf{W}_{1i} \otimes \$_{1i} = \mathbf{F}_i \otimes \$_{1i} \quad (5.14)$$

$$\tau_{st_i} = \alpha_{st_i} \mathbf{W}_{st_i} \otimes \$_{st_i} = \mathbf{F}_i \otimes \$_{st_i} \quad (5.15)$$

The *inverse force solution* requires solution of  $\alpha_{1i}$  and  $\alpha_{st_i}$  ( $i = 1, 2, 3$ ) from the linear system of equation (5.8) followed by resolution of the corresponding  $\tau_{1i}$  and  $\tau_{st_i}$  ( $i = 1, 2, 3$ ) values from equations (5.14) and (5.15), respectively.

### 5.3.1 Obtaining the associated reciprocal screws

It is necessary to obtain the screw coordinates for  $\mathbf{W}_{1i}$ ,  $\mathbf{W}_{st_i}$ ,  $\$_{1i}$  and  $\$_{st_i}$  for  $i = 1, 2, 3$ . As explained before  $\mathbf{W}_{1i}$  and  $\mathbf{W}_{st_i}$  are the reciprocal screws associated with  $\$_{1i}$  and  $\$_{st_i}$  respectively.

With an appropriate reference frame the expression for each screw is very simple [23]. To obtain the six elements of the reciprocal screws  $\mathbf{W}$  shown in Figure 5.1, a very appropriate frame is one located at the centre of the  $i$ -th spherical joint (*i.e.*  $A_i$ ) with its  $Y$ -axis aligned as  $\mathbf{W}_{st_i}$  and its  $Z$ -axis aligned with the direction of the leg (the direction of  $\mathbf{W}_{1i}$ ). This frame will be called  $\sum_{A_i}$ . The appropriate frame to get  $\$_{1i}$  and  $\$_{st_i}$  with respect to is one oriented as the inertial frame  $\sum_0$  (the inertial frame) and located at the center of the base platform as shown in Figure 5.1.

$\mathbf{W}_{1_i}$ ,  $\mathbf{W}_{st_i}$  and  $\mathcal{S}_{st_i}$  are zero pitch screws passing through the origin of their respective frames, which means that their last three elements are equal to zero. On the other hand  $\mathcal{S}_{1_i}$ , the screw representing the prismatic joint, is an infinite pitch screw having its first three elements equal to zero.

By analyzing Figures 2.1 and 5.1 the following are obtained (with respect to  $\Sigma_0$ ):

$${}^0\mathcal{S}_{1_i} = \left\{ \begin{array}{cccccc} 0 & 0 & 0 & \cos(\rho_i) & \sin(\rho_i) & 0 \end{array} \right\}^T \quad (5.16)$$

$${}^0\mathcal{S}_{st_i} = \left\{ \begin{array}{cccccc} \cos(\rho_i) & \sin(\rho_i) & 0 & 0 & 0 & 0 \end{array} \right\}^T \quad (5.17)$$

where  $\rho_i$  corresponds to the angle between the  $i$ -th prismatic actuator and the  $X$ -axis of the inertial frame ( $\Sigma_0$ ). In Figure 2.1 it can be seen that  $\rho_1 = 0$ ,  $\rho_2 = \alpha$  and  $\rho_3 = \beta$ .

The screws quantities  $\mathbf{W}_{1_i}$  and  $\mathbf{W}_{st_i}$  expressed in frame  $\Sigma_{A_i}$  become:

$${}^{A_i}\mathbf{W}_{1_i} = \left\{ \begin{array}{cccccc} 0 & 0 & 1 & 0 & 0 & 0 \end{array} \right\}^T \quad (5.18)$$

$${}^{A_i}\mathbf{W}_{st_i} = \left\{ \begin{array}{cccccc} 0 & 1 & 0 & 0 & 0 & 0 \end{array} \right\}^T \quad (5.19)$$

### 5.3.2 Expressing the screw quantities in the inertial frame

To be able to solve for  $\alpha_{1_i}$  and  $\alpha_{st_i}$  ( $i = 1, 2, 3$ ) for the linear system of equation (5.8) all of the above screw quantities and  $\mathbf{F}_{ref}$  must be expressed with respect to a common frame. If the inertial frame  $\Sigma_0$  is used (since it is being used as the reference for  $\mathbf{F}_{ref}$  and since  ${}^0\mathcal{S}_{1_i}$  and  ${}^0\mathcal{S}_{st_i}$  are already known) the following *screw transform* ( $\mathbf{T}_s$ ) can be used to map  ${}^{A_i}\mathbf{W}_i$  to  ${}^0\mathbf{W}_i$ :

$${}^0_{A_i}\mathbf{T}_{s_{A_i \rightarrow 0}} = \begin{bmatrix} {}^0_{A_i}\mathbf{R} & 0_{3 \times 3} \\ {}^0\tilde{\mathbf{r}}_{0 \rightarrow A_i} \cdot {}^0_{A_i}\mathbf{R} & {}^0_{A_i}\mathbf{R} \end{bmatrix} \quad (5.20)$$

where  $0_{3 \times 3}$  is a  $3 \times 3$  zero matrix,  ${}^0_{A_i} \mathbf{R}$  is the rotation matrix describing the orientation of frame  $\Sigma_{A_i}$  with respect to frame  $\Sigma_0$  and is defined as follows:

$${}^0_{A_i} \mathbf{R} = \begin{bmatrix} s_{\mu_i} c_{\rho_i} & -s_{\rho_i} & -c_{\mu_i} c_{\rho_i} \\ s_{\mu_i} s_{\rho_i} & c_{\rho_i} & -c_{\mu_i} s_{\rho_i} \\ c_{\mu_i} & 0 & s_{\mu_i} \end{bmatrix} \quad (5.21)$$

where  $c_*$  and  $s_*$  correspond to  $\cos(*)$  and  $\sin(*)$  respectively, and  $\mu_i$  is the angle from the horizontal plane to the  $i$ -th leg, measured in the plane formed by the  $i$ -th actuator and the  $i$ -th leg, as shown in Figure 5.1.

The element  ${}^0 \tilde{\mathbf{r}}_{0 \rightarrow A_i}$  in equation (5.20) is the skew symmetric matrix formed from vector  ${}^0 \mathbf{r}_{0 \rightarrow A_i}$  (the position vector from the origin of the inertial frame to the centre of the  $i$ -th ball joint, expressed in frame  $\Sigma_0$ ), *i.e.*,

$${}^0 \tilde{\mathbf{r}}_{0 \rightarrow A_i} = \begin{bmatrix} 0 & -{}^0 \mathbf{r}_{0 \rightarrow A_i}(z) & {}^0 \mathbf{r}_{0 \rightarrow A_i}(y) \\ {}^0 \mathbf{r}_{0 \rightarrow A_i}(z) & 0 & -{}^0 \mathbf{r}_{0 \rightarrow A_i}(x) \\ -{}^0 \mathbf{r}_{0 \rightarrow A_i}(y) & {}^0 \mathbf{r}_{0 \rightarrow A_i}(x) & 0 \end{bmatrix} \quad (5.22)$$

Let us define  $\mathbf{r}_i \equiv {}^0 \mathbf{r}_{0 \rightarrow A_i}$  for notational simplicity. As one can verify in Figure 2.1:

$$\mathbf{r}_i = \mathbf{p} + {}^0 \mathbf{a}_i = \mathbf{p} + {}^0_t \mathbf{R}^t \mathbf{a}_i \quad (5.23)$$

As discussed previously in Chapter 2 (and reported now for reader convenience) the vectors  ${}^t \mathbf{a}_i$  are defined in frame  $\Sigma_{tool}$  (a frame located at the center of the moving platform with the  $X$ -axis aligned with the  $A_i$  and  $Y$ -axis contained in the moving platform plane and with the  $Z$ -axis pointing upwards) as follows:

$${}^t \mathbf{a}_i = \begin{bmatrix} \cos(\rho_i) r_p \\ \sin(\rho_i) r_p \\ 0 \end{bmatrix} \quad (5.24)$$

where  $r_p$  is the moving platform radius.

The rotation matrix from  $\sum_{tool}$  to  $\sum_0$  is a general 3D rotation matrix and can be expressed as follows (as seen in Chapter 2):

$${}^0_t\mathbf{R} = \begin{bmatrix} c_\theta c_\phi + s_\psi s_\theta s_\phi & -c_\theta s_\phi + s_\psi s_\theta c_\phi & c_\psi s_\theta \\ c_\psi s_\phi & c_\psi c_\phi & -s_\psi \\ -s_\theta c_\phi + s_\psi c_\theta s_\phi & s_\theta s_\phi + s_\psi c_\theta c_\phi & c_\psi c_\theta \end{bmatrix} \quad (5.25)$$

where  $\psi$ ,  $\theta$  and  $\phi$  are the corresponding Euler angles of the top platform with respect to the inertial frame.

Substituting equations (5.24) and (5.25) into equation (5.23) yields:

$${}^0\mathbf{r}_{0 \rightarrow A_i} = \mathbf{r}_i = \begin{bmatrix} p_x + [{}^0_t R_{11} \cos(\rho_i) + {}^0_t R_{12} \sin(\rho_i)] r_p \\ p_y + [{}^0_t R_{21} \cos(\rho_i) + {}^0_t R_{22} \sin(\rho_i)] r_p \\ p_z + [{}^0_t R_{31} \cos(\rho_i) + {}^0_t R_{32} \sin(\rho_i)] r_p \end{bmatrix} \quad (5.26)$$

where  ${}^0_t R_{ij}$  is the  $ij$  element of the rotation matrix  ${}^0_t\mathbf{R}$ , and  $p_x$ ,  $p_y$  and  $p_z$  are the  $x$ ,  $y$  and  $z$  elements of the position vector  $\mathbf{p}$ , respectively.

Finally the  $\mu_i$  angles, required to obtain  ${}^0_{A_i}\mathbf{R}$  (equation (5.21)), can be obtained as follows:

$$\mu_i = \sin^{-1} \left( \frac{\mathbf{r}_i z}{l_i} \right) = \sin^{-1} \left( \frac{p_z + [{}^0_t R_{31} \cos(\rho_i) + {}^0_t R_{32} \sin(\rho_i)] r_p}{l_i} \right) \quad (5.27)$$

### 5.3.3 Solving the inverse force problem

The screw quantities expressed in  $\sum_{A_i}$  are the ones to be pre-multiplied by the screw transforms defined in equation (5.20). Considering that the original quantities (5.18) and (5.19) each have just one component, the final expressions are relatively simple.

For  ${}^{A_i}\mathbf{W}_{1_i}$  the result of

$${}^0\mathbf{W}_{1_i} = {}^0_{A_i}\mathbf{T}\mathbf{s}_{A_i \rightarrow 0} {}^{A_i}\mathbf{W}_{1_i} \quad (5.28)$$

will be given by the third column of the matrix  ${}^0_{A_i}\mathbf{T}\mathbf{s}_{A_i \rightarrow 0}$ . Similarly  ${}^0\mathbf{W}_{st_i}$  will correspond to the second column of the screw transform  ${}^0_{A_i}\mathbf{T}\mathbf{s}_{A_i \rightarrow 0}$ .

Having all the screw quantities expressed in the same frame, in this case the inertial frame, we can now resolve the corresponding wrench intensities,  $\alpha_{1_i}$  and  $\alpha_{st_i}$ , for a known force  $\mathbf{F}_{ref}$  to be substituted (solving the linear system of equations (5.8)). The corresponding joint and structural forces are then available from equations (5.14) and (5.15), respectively.

For a given set of actuator forces there will be a family of end-effector forces that can be sustained by the actuator and structural forces. The device can sustain a full six-system of forces but it is just capable of applying a three-system of forces. The three-system of forces that it can not apply will not cause actuator forces, *i.e.*, it is possible to sustain end-effector forces that do not load the actuators. These forces only load the structure of the mechanism, *e.g.* a pure moments around the  $Z$ -axis when the top platform is horizontal.

## 5.4 Solution of the joint and structural forces

### 5.4.1 Algorithm

In order to compare the results between the two methods mentioned in the previous sections, an algorithm that computes the inverse force solution through both methods was developed and is described here.

First an input point with the pose and architectural parameters is defined. The point is passed through the constraint equations to obtain the constrained variables  $x$ ,  $y$  and  $\phi$  and a force, in the tool frame, is defined. Then, following the process described in the previous sections, the actuated forces (and structural torques in the screw theory method) are obtained.

In the screw theory method, the directions of the reciprocal screws (expressed in frames  $\Sigma_{A_i}$ ) are first obtained. Then the reciprocal screws and the generalized force are expressed in frame  $\Sigma_0$  by multiplying them by  ${}^0_{A_i}\mathbf{T}_{s_{A_i \rightarrow 0}}$  and  ${}^0_t\mathbf{T}_{s_{t \rightarrow 0}}$ , respectively. The wrench intensities are then solved for by using the right hand side of equations (5.14) and (5.15) and then substituted back into the left hand side to obtain the actuator forces and the structural torques.

In the partial derivatives method, the Jacobian matrix  $\mathbf{J}$  (equation (2.20)) and the constraints matrix  $\mathbf{P}$  (equation (2.22)) are first computed. The generalized force is then expressed in frame  $\Sigma_0$  by multiplying it by  ${}^0_t\mathbf{T}_{s_{t \rightarrow 0}}$ . Finally equation (5.4) is used to obtain the three actuator forces.

The results obtained through the two methods are printed together for the user to inspect visually.

### 5.4.2 Sample results and comparison

Tables 5.1 and 5.2 show a comparison of the results obtained with the two different methods<sup>4</sup> when a general force is applied to the center of the moving platform when

---

<sup>4</sup>P corresponds to Partial derivatives method (Solution of the joint forces through power considerations) and S corresponds to the Screw theory method (Solution of the joint and structural forces via screw formulation).

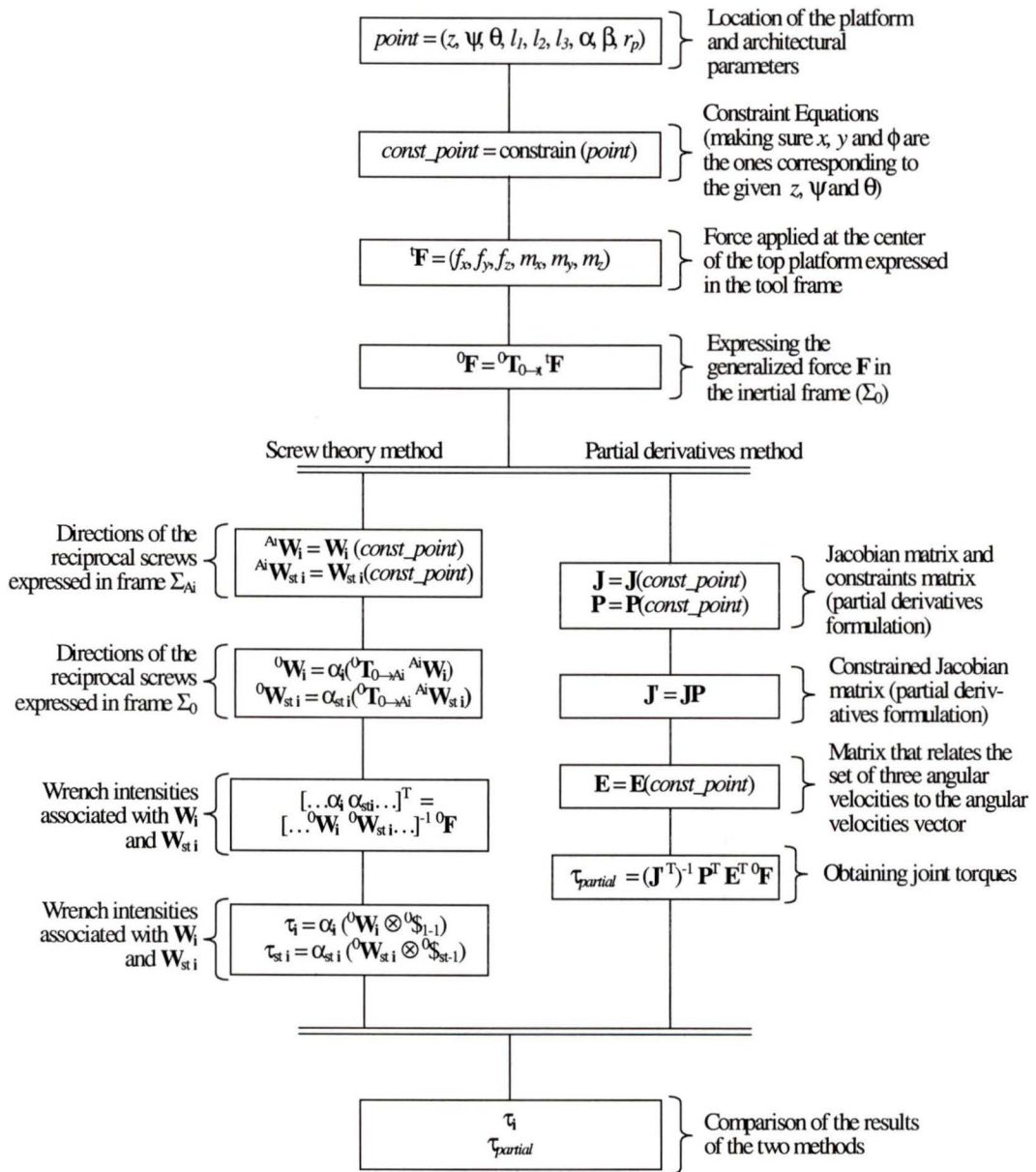


Figure 5.2: Flow diagram of the static force analysis

Applied Force	Method	$\tau_1$	$\tau_{st1}$	$\tau_2$	$\tau_{st2}$	$\tau_3$	$\tau_{st3}$
$\mathbf{F} = [0\ 0\ 0\ 0\ 0\ 0]^T$	P	0	N/A	0	N/A	0	N/A
	S	0	0	0	0	0	0
$\mathbf{F} = [1\ 0\ 0\ 0\ 0\ 0]^T$	P	0.000	N/A	0.000	N/A	0.000	N/A
	S	0.000	0.000	0.000	-0.577	0.000	0.577
$\mathbf{F} = [0\ 1\ 0\ 0\ 0\ 0]^T$	P	0.000	N/A	0.000	N/A	0.000	N/A
	S	0.000	0.666	0.000	-0.333	0.000	-0.333
$\mathbf{F} = [0\ 0\ 1\ 0\ 0\ 0]^T$	P	0.015	N/A	0.015	N/A	0.015	N/A
	S	0.015	0.000	0.015	0.000	0.015	0.000
$\mathbf{F} = [0\ 0\ 0\ 1\ 0\ 0]^T$	P	0.000	N/A	0.026	N/A	-0.026	N/A
	S	0.000	0.030	0.026	-0.015	-0.026	-0.015
$\mathbf{F} = [0\ 0\ 0\ 0\ 1\ 0]^T$	P	-0.030	N/A	0.015	N/A	0.015	N/A
	S	-0.030	0.000	0.015	0.026	0.015	-0.026
$\mathbf{F} = [0\ 0\ 0\ 0\ 0\ 1]^T$	P	0.000	N/A	0.000	N/A	0.000	N/A
	S	0.000	0.333	0.000	0.333	0.000	0.333

Table 5.1: Comparison of the static force solution for the two methods (MICRO case).

that platform is located at  $z = 0.999$  m and  $z = 1/\sqrt{2}$  m, respectively. In Tables 5.1 and 5.2 the forces are given in Newtons and the torques in N.m.

## 5.5 Stiffness analysis

A stiffness analysis of the mechanism can be performed by modeling the actuators as linear springs. Small displacements of the platform in the three Cartesian directions of motion ( $z$ ,  $\psi$  and  $\theta$ ) can be mapped into a corresponding vector of force and moments in those same directions by a *stiffness matrix* [19] which can be expressed as :

$$\mathbf{K} = k\mathbf{J}'^T\mathbf{J}' \quad (5.29)$$

where  $\mathbf{K} \in \mathfrak{R}^{3 \times 3}$  and  $k$  is a scalar that represents the stiffness of each actuator when modeled as a linear spring. Since  $k$  acts only as a scaling factor it is usually neglected [19]. The eigenvalues of  $\mathbf{K}$  (which will always be non-negative because  $\mathbf{K}$

Applied Force	Method	$\tau_1$	$\tau_{st1}$	$\tau_2$	$\tau_{st2}$	$\tau_3$	$\tau_{st3}$
$\mathbf{F} = [0\ 0\ 0\ 0\ 0\ 0]^T$	P	0	N/A	0	N/A	0	N/A
	S	0	0	0	0	0	0
$\mathbf{F} = [1\ 0\ 0\ 0\ 0\ 0]^T$	P	0.000	N/A	0.000	N/A	0.000	N/A
	S	0.000	0.000	0.000	-0.408	0.000	0.408
$\mathbf{F} = [0\ 1\ 0\ 0\ 0\ 0]^T$	P	0.000	N/A	0.000	N/A	0.000	N/A
	S	0.000	0.47133	0.000	-0.256	0.000	-0.236
$\mathbf{F} = [0\ 0\ 1\ 0\ 0\ 0]^T$	P	0.333	N/A	0.333	N/A	0.333	N/A
	S	0.333	0.000	0.333	0.000	0.333	0.000
$\mathbf{F} = [0\ 0\ 0\ 1\ 0\ 0]^T$	P	0.000	N/A	0.577	N/A	-0.577	N/A
	S	0.000	0.471	0.577	-0.236	-0.577	-0.236
$\mathbf{F} = [0\ 0\ 0\ 0\ 1\ 0]^T$	P	-0.667	N/A	0.333	N/A	0.333	N/A
	S	-0.667	0.000	0.333	0.408	0.333	-0.408
$\mathbf{F} = [0\ 0\ 0\ 0\ 0\ 1]^T$	P	0.000	N/A	0.000	N/A	0.000	N/A
	S	0.000	0.236	0.000	0.236	0.000	0.236

Table 5.2: Comparison of the static force solution for the two methods (MACRO case).

is a positive semidefinite matrix) give the stiffness in the principal directions, those being the eigenvectors [19]. Furthermore, the elements of the main diagonal of  $\mathbf{K}$  correspond to the stiffnesses  $k_z$ ,  $k_\psi$  and  $k_\theta$ , in the  $z$ ,  $\psi$  and  $\theta$  directions respectively. These can be physically interpreted as the stiffness of the mechanism in response to a force (or moment) applied at the moving platform, assuming that the actuators have a unit stiffness, and that all the compliance in the mechanism originates in the actuators. It is important to notice that the  $3 \times 3$  Jacobian matrix  $\mathbf{J}'$  only provides stiffness information along the directions corresponding to the unconstrained degrees of freedom of the platform. Although an alternative stiffness matrix of dimension  $6 \times 6$  could be formed using the conventional Jacobian matrix  $\mathbf{J}$ , this matrix would be rank-deficient and therefore yield incorrect results.

Figure 5.3 shows an example of the behaviour of the stiffness of the mechanism with variations in the  $z$ -position of the platform. The upper curve corresponds to

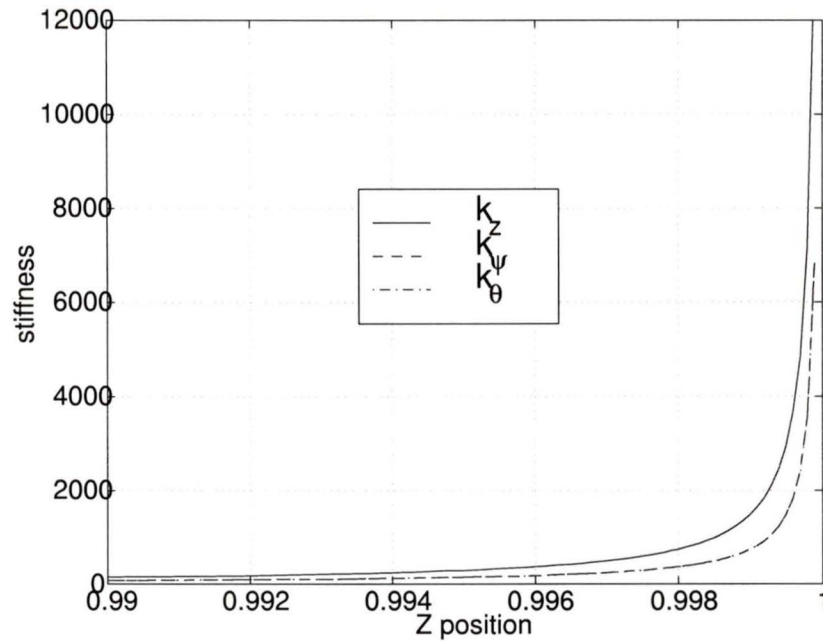


Figure 5.3: Variation of stiffness with  $z$  ( $\psi = \theta = 0$ ). The lower curve corresponds to  $k_\psi$  and  $k_\theta$  ( $k_\psi = k_\theta$  when  $\psi = \theta = 0$ ).

$k_z$ , while the lower curve represents  $k_\psi$  and  $k_\theta$  which are equal in this configuration. The three stiffness parameters tend to go to infinity when the legs become vertical ( $z = 1$ ). Figure 5.4 shows the behaviour of the stiffness parameters with respect to variations to the orientation of the platform, for  $z = 0.999$ . As  $z$  is reduced, these surfaces tend to flatten and shift to smaller values of stiffness.

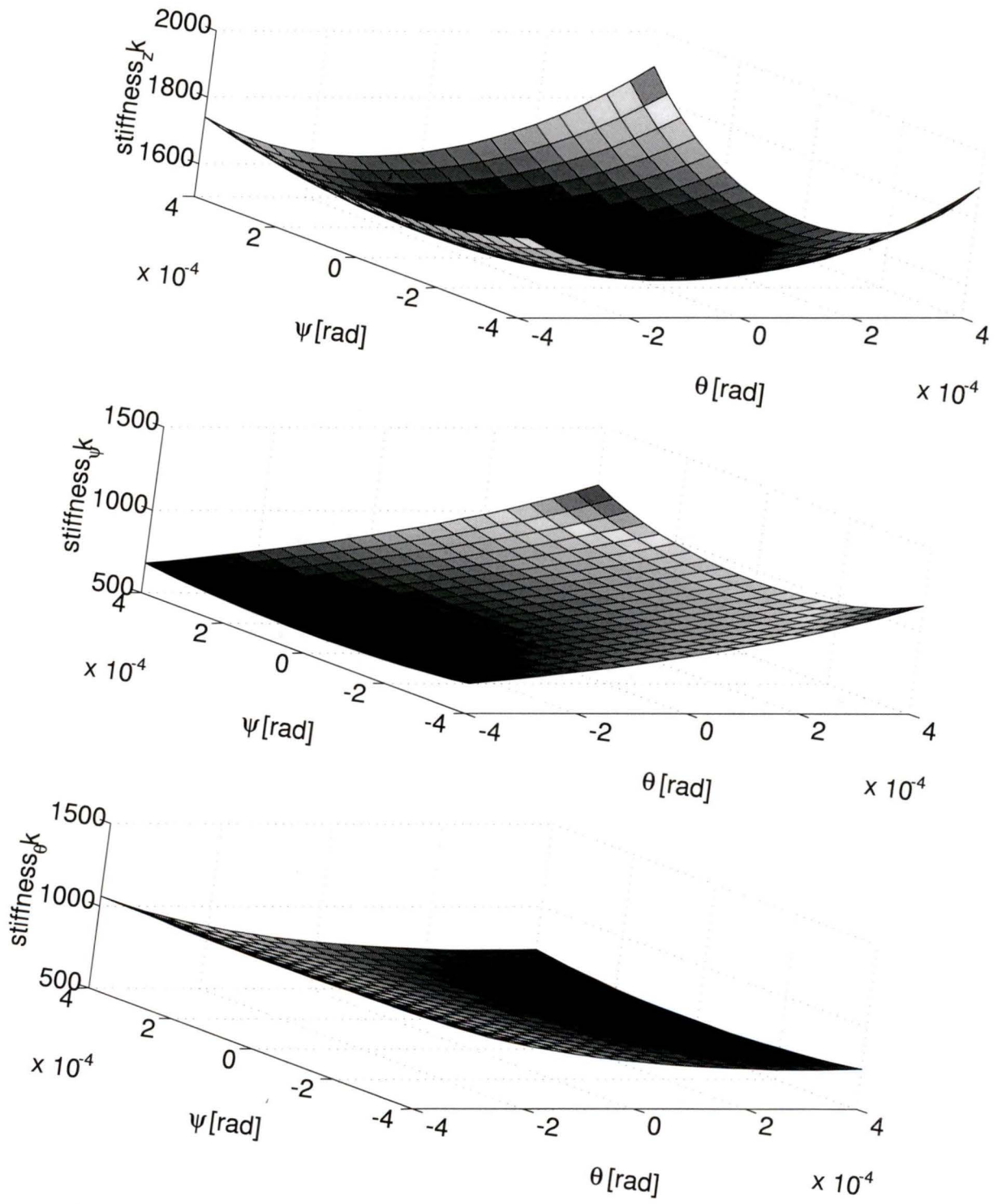


Figure 5.4: Stiffness maps ( $z = 0.999$ ) a)  $k_z$ , b)  $k_\psi$  and c)  $k_\theta$ .

# Chapter 6

## Conclusions

### 6.1 Kinematic analysis

A three-degree-of-freedom (dof) mechanism for telescope focussing applications has been described. The mechanism's architecture consists of three prismatic-revolute-spherical (PRS) serial linkages supporting a common payload platform, with the P joint of each serial linkage actuated and lying in a common base plane.

The mechanism was proposed as a device well suited to tasks requiring elevation perpendicular to the base platform (1 dof  $z$  translation) and pointing (2 dof orientation:  $[\psi, \theta]$ ) of a payload, particularly the secondary mirror of a Cassegrain type telescope. Due to the coupled nature of the linkages of the parallel mechanism, however, small constrained translational motions (termed  $x$  and  $y$  parasitic in this work) within a plane parallel to the base platform were seen to be necessary.

Solution of the forward and inverse kinematic problems were described, and a set of constraint equations was derived to describe the inter-relationship between the Cartesian coordinates of the platform. The kinematic properties of the mecha-

nism were investigated and shown to be good in the range of motion for which it is intended. A useful property of this mechanism, when operated near its ‘all-legs vertical’ singularity, is that it requires large actuator displacements for small platform motions. Although this would normally be considered a detriment, in the present application, it allows the use of conventional actuator technology when much more expensive actuators might normally be required.

## 6.2 Parasitic motion analysis

The constrained variables, defined when the constraint equations were presented, constitute the parasitic motions. The influence of the architectural parameters on the parasitic motions was analyzed. It was found that the parasitic motions are independent of the elevation ( $z$  position) of the top platform with respect to the base plane. It was also shown that the parasitic motions are independent of the leg length ( $l_i, i = 1, 2, 3$ ). A geometrical interpretation for these independencies was given.

The  $x$  and  $y$  parasitics were shown to be linearly dependent on the platform radius ( $r_p$ ). By contrast, the  $\phi$  motion was completely independent of most of the architectural parameters, *i.e.* the angle  $\phi$  only depends on the pose of the platform and the angles  $\alpha$  and  $\beta$  between the actuators.

## 6.3 Dexterity and Dexterous workspace analysis

Dexterity measures were discussed and a dexterity measure based on the condition number of the constrained Jacobian matrix (formed by the Jacobian matrix and the constraint matrix) was adopted.

The dexterous workspace was defined as a function of the dexterity measure of the manipulator. It was pointed out that the dexterous workspace is a subset of the reachable workspace. A comparison of the workspace was undertaken by obtaining different plots of the workspace varying the architectural parameters of the device. It was concluded that, since the condition number of the Jacobian matrix is scale dependent, all of the architectural parameters will have an effect on the shape and/or size of the workspace but the tendency can be illustrated by the present study. The leg length ( $l_i$ ) and the platform radius ( $r_p$ ) were shown to have a “scaling” effect (increasing  $l_i$  increases the workspace and decreasing  $r_p$ —down to  $1/\sqrt{2}$ —also increases the workspace) while the angle between the prismatic actuators ( $\alpha$  and  $\beta$ ) changed the horizontal cross-section aspect ratio.

## 6.4 Optimization

Optimization of relevant architectural parameters for the mechanism was discussed. Since the parasitic motions mentioned earlier could be detrimental, architectural (design) parameter values minimizing their magnitude were sought.

It was concluded that for the parasitic motion optimization,  $\alpha$  and  $\beta$  (the angles between the actuated prismatic joints) were the only relevant parameters. On the other hand, the dexterity measure over the workspace was found to be dependent on six design variables ( $\alpha, \beta, l_1, l_2, l_3, r_p$ ). The only relevant parameters, however, were concluded to be  $\alpha, \beta$  and  $r_p$  (the platform radius) since  $\kappa$  was found to decrease monotonically with increasing  $l_i$  (fixed leg length), and  $l_i$  would be limited by mechanical design considerations. Both functions were found to be unimodal within the studied range.

A nonlinear optimization method (quasi-Newton with Hessian update) was utilized to find optimal  $\alpha$  and  $\beta$  values for objectives of minimum direction-specific ( $\delta_\rho$ ), average ( $\delta_{ave}$ ) and mini-max ( $\delta_{mm}$ ) parasitic motions and average ( $\kappa_{ave}$ ) and mini-max ( $\kappa_{mm}$ ) of the condition number. Example featuring a micro and macro ranges of  $[\psi, \theta]$  motion,  $-0.0004 \leq \psi$  and  $\theta \leq 0.0004$  radians and  $-0.2 \leq \psi$  and  $\theta \leq 0.2$  radians respectively, were considered, with a  $21 \times 21$  grid of  $[\psi, \theta]$  values within these ranges.

The  $\alpha^*$  and  $\beta^*$  values, found for minimization of parasitic motion in a specific direction, agreed with values determined by geometric reasoning. This was concluded to be evidence that the developed algorithms were functioning properly. For  $\delta_{ave}$ ,  $\delta_{mm}$ ,  $\kappa_{ave}$  and  $\kappa_{mm}$  objectives,  $\alpha^*$  and  $\beta^*$  were seen to be symmetric.

## 6.5 Static force analysis

Based on conservation of power, an inverse force solution was obtained. The inverse force solution allows the designer to analyze what actuator forces/torques are required to sustain/apply a force at/to the tool.

A inverse force solution based on screw theory was formulated. This formulation allowed us to obtain some information on the structural forces/torques produced when a generalized force is applied at the moving platform as well as the required actuator forces/torques.

The two methods were then compared and it is concluded that the screw theory formulation provides more information while having a simpler geometrical interpretation. A more detailed formulation (through screw theory) would lead to a thorough structural analysis.

## 6.6 Future work

A more accurate method to approximate the average of the objective functions should be investigated. Some preliminary tests were made using a numerical integrator included in Matlab (*i.e.* quad8). The routine uses an adaptive recursive Newton Cotes 8 panel rule [15]. These results showed significant improvement in precision and speed.

The analysis of the HVRam mechanism for other applications, *e.g.* motion simulation devices, machine tools, *etc.* is also suggested. In a more general scope, the analysis of lower degree-of-freedom mechanisms would be useful since most existing research has concentrated on the analysis of six degree-of-freedom devices. However, as shown in this work, lower degree-of-freedom devices (less than six) can perform certain tasks with a less complicated kinematic layout.

In most applications the dynamics of the mechanism should be analyzed. Also, a finite element analysis (FEA) would be useful in order to obtain more detailed structural information for a final design of the mechanism.

# Appendix A

## Jacobian Matrix

The Jacobian matrix of the HVRam is expressed as follows:

$$\mathbf{J} = \left[ \frac{\partial \mathbf{S}}{\partial \mathbf{x}} \right] = \begin{bmatrix} \frac{\partial s_1}{\partial x} & \frac{\partial s_1}{\partial y} & \frac{\partial s_1}{\partial z} & \frac{\partial s_1}{\partial \psi} & \frac{\partial s_1}{\partial \theta} & \frac{\partial s_1}{\partial \phi} \\ \frac{\partial s_2}{\partial x} & \frac{\partial s_2}{\partial y} & \frac{\partial s_2}{\partial z} & \frac{\partial s_2}{\partial \psi} & \frac{\partial s_2}{\partial \theta} & \frac{\partial s_2}{\partial \phi} \\ \frac{\partial s_3}{\partial x} & \frac{\partial s_3}{\partial y} & \frac{\partial s_3}{\partial z} & \frac{\partial s_3}{\partial \psi} & \frac{\partial s_3}{\partial \theta} & \frac{\partial s_3}{\partial \phi} \end{bmatrix} = \begin{bmatrix} J_{11} & J_{12} & J_{13} & J_{14} & J_{15} & J_{16} \\ J_{21} & J_{22} & J_{23} & J_{24} & J_{25} & J_{26} \\ J_{31} & J_{32} & J_{33} & J_{34} & J_{35} & J_{36} \end{bmatrix}$$

where:

$$\begin{aligned} J_{11} &= 1 \\ J_{12} &= \frac{-r_{1y}}{m} \\ J_{13} &= \frac{-r_{1z}}{m} \\ J_{14} &= A_{1_1}^* - \frac{r_{1y}A_{2_1}^* + r_{1z}A_{3_1}^*}{m} \\ J_{15} &= B_{1_1}^* - \frac{r_{1z}B_{3_1}^*}{m} \\ J_{16} &= C_{1_1}^* - \frac{r_{1y}C_{2_1}^* + r_{1z}C_{3_1}^*}{m} \end{aligned}$$

$$\begin{aligned}
J_{21} &= \cos(\alpha) + \frac{-r_{2x} + u \cos(\alpha)}{n} \\
J_{22} &= \sin(\alpha) + \frac{-r_{2y} + u \sin(\alpha)}{n} \\
J_{23} &= \frac{-r_{2z}}{n} \\
J_{24} &= A_{12}^* \cos(\alpha) + A_{22}^* \sin(\alpha) \\
&\quad + \frac{-r_{2x}A_{12}^* - 2r_{2y}A_{22}^* - r_{2z}A_{32}^* + u(A_{12}^* \cos(\alpha) + A_{22}^* \sin(\alpha))}{n} \\
J_{25} &= B_{12}^* \cos(\alpha) - \frac{r_{2x}B_{12}^* r_{2z}B_{32}^* - uB_{12}^* \cos(\alpha)}{n} \\
J_{26} &= C_{12}^* \cos(\alpha) + C_{22}^* \sin(\alpha) \\
&\quad - \frac{r_{2x}C_{12}^* + r_{2y}C_{22}^* + r_{2z}C_{32}^* - u(C_{12}^* \cos(\alpha) + C_{22}^* \sin(\alpha))}{n} \\
J_{31} &= \cos(\beta) + \frac{-r_{3x} + t \cos(\beta)}{q} \\
J_{32} &= \sin(\beta) + \frac{-r_{3y} + t \sin(\beta)}{q} \\
J_{33} &= \frac{-r_{3z}}{q} \\
J_{34} &= A_{13}^* \cos(\beta) + A_{23}^* \sin(\beta) \\
&\quad + \frac{-r_{3x}A_{13}^* - 2r_{3y}A_{23}^* - r_{3z}A_{33}^* + t(A_{13}^* \cos(\beta) + A_{23}^* \sin(\beta))}{q} \\
J_{35} &= B_{13}^* \cos(\beta) + \frac{-r_{3x}B_{13}^* - r_{3z}B_{33}^* + B_{13}^* t \cos(\beta)}{q} \\
J_{36} &= C_{13}^* \cos(\beta) + C_{23}^* \sin(\beta) \\
&\quad + \frac{-r_{3x}C_{13}^* - 2r_{3y}C_{23}^* - r_{3z}C_{33}^* + t(C_{13}^* \cos(\beta) + C_{23}^* \sin(\beta))}{q}
\end{aligned}$$

and

$$\begin{aligned}
r_{ix} &= x + T_{11}a'_{ix} + T_{12}a'_{iy} + T_{13}a'_{iz} \\
r_{iy} &= y + T_{21}a'_{ix} + T_{22}a'_{iy} + T_{23}a'_{iz} \\
r_{iz} &= z + T_{31}a'_{ix} + T_{32}a'_{iy} + T_{33}a'_{iz}
\end{aligned}$$

$$\mathbf{a}'_i = \begin{bmatrix} a'_{ix} & a'_{iy} & a'_{iz} \end{bmatrix}^T$$

$$\mathbf{T} = \mathbf{T}_{ZXY} = \mathbf{R}_Y(\theta)\mathbf{R}_X(\psi)\mathbf{R}_Z(\phi) = \begin{bmatrix} c_\theta c_\phi + s_\psi s_\theta s_\phi & -c_\theta s_\phi + s_\psi s_\theta c_\phi & c_\psi s_\theta \\ c_\psi s_\phi & c_\psi c_\phi & -s_\psi \\ -s_\theta c_\phi + s_\psi c_\theta s_\phi & s_\theta s_\phi + s_\psi c_\theta c_\phi & c_\psi c_\theta \end{bmatrix}$$

$$\mathbf{A}_{j_i}^* = \mathbf{A}_j \cdot \mathbf{a}'_i; \quad \mathbf{B}_{j_i}^* = \mathbf{B}_j \cdot \mathbf{a}'_i; \quad \mathbf{C}_{j_i}^* = \mathbf{C}_j \cdot \mathbf{a}'_i$$

$$\mathbf{A}_1 = \begin{bmatrix} \frac{\partial}{\partial \psi} T_{11} & \frac{\partial}{\partial \psi} T_{12} & \frac{\partial}{\partial \psi} T_{13} \end{bmatrix} = \begin{bmatrix} s_\theta c_\psi s_\phi & s_\theta c_\psi c_\phi & -s_\theta s_\psi \end{bmatrix}$$

$$\mathbf{A}_2 = \begin{bmatrix} \frac{\partial}{\partial \psi} T_{21} & \frac{\partial}{\partial \psi} T_{22} & \frac{\partial}{\partial \psi} T_{23} \end{bmatrix} = \begin{bmatrix} -s_\psi s_\phi & -s_\psi c_\phi & -c_\psi \end{bmatrix}$$

$$\mathbf{A}_3 = \begin{bmatrix} \frac{\partial}{\partial \psi} T_{31} & \frac{\partial}{\partial \psi} T_{32} & \frac{\partial}{\partial \psi} T_{33} \end{bmatrix} = \begin{bmatrix} c_\theta c_\psi s_\phi & c_\theta c_\psi c_\phi & -c_\theta s_\psi \end{bmatrix}$$

$$\mathbf{B}_1 = \begin{bmatrix} \frac{\partial}{\partial \theta} T_{11} & \frac{\partial}{\partial \theta} T_{12} & \frac{\partial}{\partial \theta} T_{13} \end{bmatrix} = \begin{bmatrix} c_\theta s_\psi s_\phi - s_\theta c_\phi & c_\theta s_\psi c_\phi + s_\theta s_\phi & c_\theta c_\psi \end{bmatrix}$$

$$\mathbf{B}_2 = \begin{bmatrix} \frac{\partial}{\partial \theta} T_{21} & \frac{\partial}{\partial \theta} T_{22} & \frac{\partial}{\partial \theta} T_{23} \end{bmatrix} = \begin{bmatrix} 0 & 0 & 0 \end{bmatrix}$$

$$\mathbf{B}_3 = \begin{bmatrix} \frac{\partial}{\partial \theta} T_{31} & \frac{\partial}{\partial \theta} T_{32} & \frac{\partial}{\partial \theta} T_{33} \end{bmatrix} = \begin{bmatrix} -s_\theta s_\psi s_\phi - c_\theta c_\phi & -s_\theta s_\psi c_\phi + c_\theta s_\phi & -s_\theta c_\psi \end{bmatrix}$$

$$\mathbf{C}_1 = \begin{bmatrix} \frac{\partial}{\partial \phi} T_{11} & \frac{\partial}{\partial \phi} T_{12} & \frac{\partial}{\partial \phi} T_{13} \end{bmatrix} = \begin{bmatrix} s_\theta s_\psi c_\phi - c_\theta s_\phi & -s_\theta s_\psi s_\phi - c_\theta c_\phi & 0 \end{bmatrix}$$

$$\mathbf{C}_2 = \begin{bmatrix} \frac{\partial}{\partial \phi} T_{21} & \frac{\partial}{\partial \phi} T_{22} & \frac{\partial}{\partial \phi} T_{23} \end{bmatrix} = \begin{bmatrix} c_\psi s_\phi & -c_\psi c_\phi & 0 \end{bmatrix}$$

$$\mathbf{C}_3 = \begin{bmatrix} \frac{\partial}{\partial \phi} T_{31} & \frac{\partial}{\partial \phi} T_{32} & \frac{\partial}{\partial \phi} T_{33} \end{bmatrix} = \begin{bmatrix} c_\theta s_\psi c_\phi + s_\theta s_\phi & -c_\theta s_\psi s_\phi + s_\theta c_\phi & 0 \end{bmatrix}$$

$$m = (l_i^2 - r_{1y}^2 - r_{1z}^2)^{1/2}$$

$$n = (l_2^2 - r_{2x}^2 - r_{2y}^2 - r_{2z}^2 + u^2)^{1/2}$$

$$u = r_{2x} \cos(\alpha) + r_{2y} \sin(\alpha)$$

$$q = (l_3^2 - r_{3x}^2 - r_{3y}^2 - r_{3z}^2 + t^2)^{1/2}$$

$$t = r_{3x} \cos(\beta) + r_{3y} \sin(\beta)$$

## Appendix B

### Constraints Matrix

The constraints matrix is a Jacobian matrix obtained as follows:

$$\mathbf{P} = \begin{bmatrix} \frac{\partial x}{\partial z} & \frac{\partial x}{\partial \psi} & \frac{\partial x}{\partial \theta} \\ \frac{\partial y}{\partial z} & \frac{\partial y}{\partial \psi} & \frac{\partial y}{\partial \theta} \\ 1 & 0 & 0 \\ 0 & 1 & 0 \\ 0 & 0 & 1 \\ \frac{\partial \phi}{\partial z} & \frac{\partial \phi}{\partial \psi} & \frac{\partial \phi}{\partial \theta} \end{bmatrix} = \begin{bmatrix} 0 & P_{12} & P_{13} \\ 0 & P_{22} & P_{23} \\ 1 & 0 & 0 \\ 0 & 1 & 0 \\ 0 & 0 & 1 \\ 0 & P_{62} & P_{63} \end{bmatrix}$$

where:

$$P_{22} = \left( s_\psi K - M c_\psi + \frac{c_\psi K^2 M}{S^2} \right) \frac{r_p}{S^{1/2}}$$

$$P_{23} = \left( -N + \frac{K^2 N}{S^2} \right) \frac{c_\psi r_p}{S^{1/2}}$$

$$P_{62} = MS^{-1}$$

$$P_{63} = NS^{-1}$$

$$\begin{aligned}
P_{12} &= \left( \frac{c_\theta KM}{S^2} - s_\theta c_\psi (K + M) + \frac{s_\theta s_\psi K^2 M}{S^2} \right) \frac{r_p c_\beta}{S^{1/2}} \\
&\quad - \left( -c_\theta M + s_\theta c_\psi - \frac{s_\theta s_\psi KM}{S^2} + \frac{c_\theta K^2 M}{S^2} \right) \frac{r_p s_\beta}{S^{1/2}} \\
&\quad + \left( (Mc_\psi - s_\psi K) - \frac{c_\psi KM}{S^2} - \frac{s_\psi s_\beta}{(c_\beta - 1)} - \frac{c_\psi s_\beta KM}{(c_\beta - 1) S^2} \right) \frac{(c_\beta - 1) r_p}{S^{1/2} \tan(\beta)} \\
P_{13} &= \left( s_\theta - s_\theta s_\psi N - c_\theta s_\psi K + \frac{c_\theta KN}{S^2} + \frac{s_\theta s_\psi K^2 N}{S^2} \right) \frac{r_p c_\beta}{S^{1/2}} \\
&\quad - \left( c_\theta s_\psi - c_\theta N + s_\theta K - \frac{s_\theta s_\psi KN}{S^2} + \frac{c_\theta K^2 N}{S^2} \right) \frac{r_p s_\beta}{S^{1/2}} \\
&\quad + \left( 1 - \left( \frac{s_\beta}{(c_\beta - 1)} + 1 \right) \frac{K^2}{S^2} \right) \frac{N (c_\beta - 1) c_\psi r_p}{S^{1/2} \tan(\beta)}
\end{aligned}$$

and

$$A = c_\alpha - c_\beta$$

$$B = s_\alpha - s_\beta$$

$$C = \frac{c_\beta - 1}{\tan(\beta)} - \frac{c_\alpha - 1}{\tan(\alpha)}$$

$$Q = Ac_\theta - Ac_\psi + Bs_\psi s_\theta$$

$$R = As_\psi s_\theta + Bc_\psi - Cc_\theta$$

$$K = \frac{Q}{R}$$

$$S = 1 + K^2$$

$$T = (Ac_\psi s_\theta - Bs_\psi)$$

$$U = (As_\psi + Bc_\psi s_\theta)$$

$$V = (-As_\theta + Bs_\psi c_\theta)$$

$$W = (As_\psi c_\theta + Cs_\theta)$$

$$M = \frac{1}{R} (U - KT)$$

$$N = \frac{1}{R} (V - KW)$$

## References

- [1] S. K. Advani, M. A. Nahon, N. Haeck, and J. Albronda. Optimization of six-degrees-of-freedom motion systems for flight simulators. In *Proceedings of the 1997 AIAA Modeling and Simulation Technologies Conference*, pages 12–22, New Orleans, Louisiana, August 1997.
- [2] T. Arai, K. Cleary, T. Nakamura, H. Adachi, and K. Homma. Design, analysis and construction of a prototype parallel link manipulator. In *IEEE International Workshop on Intelligent Robots and Systems '90*, pages 205–211, Tsuchiura, Ibaraki, Japan, July 1990.
- [3] F. P. Beer and E. R. Johnston. *Vector Mechanics for Engineers, 5th ed.* McGraw-Hill Publishing Company, New York, 1988.
- [4] R. Ben-Horin and M. Shoham. Construction of a six-degrees-of-freedom parallel manipulator with three planarly actuated links. In *Proceedings of the ASME Mechanisms Conference*, Irvine, California, USA, 1996. ASME.
- [5] B. Buckham. Image correction at the secondary of reflecting telescopes. Technical report, Department of Mechanical Engineering, University of Victoria, October 1995. Term paper.
- [6] B. Buckham. The hvram: A parallel manipulator. Technical report, Department of Mechanical Engineering, University of Victoria, May 1996. Term paper.
- [7] J. A. Carretero, M. Nahon, C. M. Gosselin, and B. Buckham. Kinematic analysis of a three-dof parallel mechanism for telescope applications. In *Proceedings of the 1997 ASME Design Engineering Technical Conference*, Sacramento, California, September 1997.
- [8] J. A. Carretero, M. Nahon, and R. P. Podhorodeski. Workspace analysis of a three dof parallel manipulator. In *Proceedings of the 1998 IROS Conference*, Victoria, B. C., Canada, October 1998.

- [9] J. A. Carretero, R. P. Podhorodeski, and M. Nahon. Architecture optimization of a three dof parallel manipulator. In *Proceedings of the 1998 ASME Design Engineering Technical Conference*, Atlanta, Georgia, September 1998.
- [10] C. P. Cavedoni, A. J. Pickles, T. T. Young, W. Nakamura, L. L. Cowie, J. E. Graves, K. T. C. Jim, T. Keller, G. A. Lupino, M. J. Northcott, C. A. Roddier, A. Stockton, R. J. Wainscoat, and H. Yamada. The uh/ifa fast tip tilt secondary. In *Proceedings of the SPIE-Advanced Technology Optical Telescopes V*, volume 2199, pages 504–515, Kona, Hawaii, March 1994.
- [11] B. W. Char, K. O. Geddes, G. H. Gonnet, B. L. Leong, M. B. Monagan, and S. M. Watt. *Maple V Language Reference Manual*. Waterloo Maple Publishing, Waterloo, Ontario, Canada, 1991.
- [12] L. M. Close and D. W. McCarthy Jr. High-resolution imaging with tip-tilt cassegrain secondary. *Publications of the Astronomical Society of the Pacific*, 106(695):77–86, 1994.
- [13] J. J. Craig. *Introduction to Robotics: mechanics and control*. Addison-Wesley Publishing Co., Reading, Massachusetts, USA, 1986.
- [14] J. E. Dieudonne, R. V. Parrish, and R. R. Bardusch. An actuator extension transformation for a motion simulator and an inverse transformation applying newton-raphson's method. Technical Report TN-D 7067, NASA, 1972.
- [15] G. E. Forsythe, M. A. Malcolm, and C. B. Moler. *Computer Methods for Mathematical Computations*. Prentice-Hall, Inc., Englewood Cliffs, N. J., 1977.
- [16] P. E. Gill, W. Murray, and M. H. Wright. *Practical Optimization*. Academic Press, London, UK, 1981.
- [17] C. Gosselin. Determination of the workspace of 6-dof parallel manipulators. *ASME Journal of Mechanical Design*, 112:331–336, September 1990.
- [18] C. Gosselin and J. Angeles. The optimum kinematic design of planar three-degrees-of-freedom parallel manipulator. *ASME Journal of Mechanisms, Transmissions and Automation in Design*, 110(1):35–41, 1988.
- [19] C. M. Gosselin. Stiffness mappings for parallel manipulators. *IEEE Transactions on Robotics and Automation*, 6(3):377–382, June 1990.
- [20] V. E. Gough and S. G. Whitehall. Universal tyre test machine. In *9th. International Congress of F.I.S.I.T.A. (Fédération Internationale des Sociétés d'Ingénieurs des Techniques de l'Automobile)*, volume 117, pages 117–135, May 1962.

- [21] A. Grace. *Optimization Toolbox User's Guide*. The MathWorks, Inc., November 1992.
- [22] K. H. Hunt. *Kinematic Geometry of Mechanisms*. Oxford Science Publications, Oxford, UK, 1978.
- [23] K. H. Hunt. Robot kinematics - a compact analytical inverse solution for velocities. *Journal of Mechanisms, Transmissions and Automation Design*, 109:42–49, March 1987.
- [24] J. Kieffer and J. Lenarčič. On the exploitation of mechanical advantages near robot singularities. In *3rd International Workshop on Advances in Robot Kinematics*, pages 65–72, Ferrara, Italy, September 1992.
- [25] C. A. Klein and B. E. Blaho. Dexterity measures for the design and control of kinematically redundant manipulators. *The International Journal of Robotics Research*, 6(2):72–83, 1987.
- [26] A. Kumar and K. J. Waldron. The dexterous workspace. Number ASME paper 80-DET-108, 1980.
- [27] K. Lee and D. Shah. Kinematic analysis of a three-degree-of-freedom in-parallel actuated manipulator. *IEEE Journal of Robotics and Automation*, 4(3):354–360, 1988.
- [28] K. R. Lorell, J. N. Auburn, and G. J. Feher. Design and operation of the infrared chopping secondary mirror for the keck 10-meter telescope. In *Proceedings of the SPIE-Adaptive Optics in Astronomy*, volume 2201, pages 821–832, Kona, Hawaii, March 1994.
- [29] O. Ma. *Mechanical Analysis of Parallel Manipulators with Simulation, Design and Control Applications*. PhD thesis, Department of Mechanical Engineering, McGill University, Montréal, Québec, Canada, June 1991.
- [30] H. Marth, E. Pitz, R. R. Rohlof, S. Hippler, and K. Wagner. Five axis secondary for UKIRT. In *Proceedings of the SPIE-Advanced Technology Optical Telescopes V*, volume 2199, pages 516–522, Kona, Hawaii, March 1994.
- [31] C. Melchiorri. Static force analysis for general cooperating manipulators. In *Proceedings of the 1994 IEEE International Conference on Robotics and Automation*, pages 888–895, San Diego, California, USA, May 1994.
- [32] J.-P. Merlet and C. M. Gosselin. Nouvelle architecture pour un manipulateur parallèle à six degrés de liberté. *Mechanism and Machine Theory*, 26(1):77–90, 1990.

- [33] M. Nahon, R. Ricard, and C. M. Gosselin. A comparison of flight simulator motion-base architectures. In *CEAS Symposium on Simulation Technology*, October 1995.
- [34] Y. Nakamura. *Advanced robotics: redundancy and optimization*. Addison-Wesley Publishing Co., Reading, Massachusetts, USA, 1991.
- [35] L. Notash and R. P. Podhorodeski. Complete forward displacement solutions for a class of three-branch parallel manipulators. *Journal of Robotic Systems*, 11(6):471–485, 1994.
- [36] L. Notash and R. P. Podhorodeski. Forward displacement analysis and uncertainty configurations of parallel manipulators with a redundant branch. *Journal of Robotic Systems*, 13(9):587–601, 1996.
- [37] K. H. Pittens and R. P. Podhorodeski. A family of Stewart platforms with optimal dexterity. *Journal of Robotic System*, 10(4):463–479, 1993.
- [38] E. Pitz, R.-R. Rohloff, and H. Marth. UKIRT 5-axis tip-tilt secondary electromechanical and optical design. In *Proceedings of ICO-16 Satellite Conference on Active and Adaptive Optics*, Garching, Germany, 1993.
- [39] N. Pouliot. *Analyse, Optimisation et Conception de Mécanismes de Simulation de Mouvement à Trois Degrés de Liberté*. M. sc. thesis, Département de Génie Mécanique, Université Laval, Québec, Canada, May 1997.
- [40] N. A. Pouliot, M. A. Nahon, and C. M. Gosselin. Analysis and comparison of the motion simulation capabilities of three-degrees-of-freedom flight simulators. In *Proceedings of the 1996 AIAA Flight Simulation Technologies Conference*, pages 29–41, San Diego, California, USA, 1996.
- [41] D. R. Smith. Correction of errors in active surfaces. In *Proceedings of the ASME Mechanisms Conference*, volume DE-70, pages 29–34, Minneapolis, USA, 1994.
- [42] D. R. Smith and P. C. Parziale. The kinematics of active surfaces: hyper-redundant in-parallel manipulators. In *Proceedings of the ASME Mechanisms Conference*, Irvine, California, USA, 1996.
- [43] D. Stewart. A platform with six degrees of freedom. In *Proceedings of the Institute of Mechanical Engineering*, volume 180, pages 371–386, London, U.K., 1965.
- [44] R. S. Stoughton and T. Arai. A modified Stewart platform manipulator with improved dexterity. *IEEE Transactions on Robotics and Automation*, 9(2):166–173, April 1993.

- [45] G. Strang. *Linear algebra and its applications*. Academic Press Inc., New York, NY, USA, 1976.
- [46] F. Tahmashebi and L.-W. Tsai. On the stiffness of a novel six-degree-of-freedom parallel manipulator. *Journal of Robotic Systems*, 12(12):845–856, 1995.
- [47] S.-L. Wang and K. J. Waldron. A study of the singular configurations of serial manipulators. *ASME Journal of Mechanisms, Transmissions, and Automation in Design*, 109(1):14–20, March 1987.
- [48] P.-H. Yang, K. J. Waldron, and D. E. Orin. Kinematics of a three degree-of-freedom motion platform for a low-cost driving simulator. In *Proceedings of the 5th. International Symposium of Advances in Robot Kinematics*, 1996.
- [49] K. E. Zanganeh and J. Angeles. Kinematic isotropy and the optimum design of parallel manipulators. *The International Journal of Robotics Research*, 16(2):185–197, April 1997.

# Vita

**Surname:** Carretero G.

**Given Names:** Juan Antonio

**Place of Birth:** Mexico City, Mexico

**Date of Birth:** October 13<sup>th</sup>, 1971

## **Educational Institutions Attended:**

Licée Franco Mexicain	1985 to 1991
National University of Mexico (UNAM)	1991 to 1996
University of Victoria	1996 to 1998

## **Degrees Awarded:**

French Baccalauréat	Licée Franco Mexicain	1991
B.Eng. (Honours)	National University of Mexico (UNAM)	1996

## **Honours and Awards:**

Graduate Teaching Fellowship (University of Victoria)	1996-1998
Research Assistantship (University of Victoria)	1996-1998
Early Initiation to Research Award (UNAM)	1995
Mention Assez Bien (French Baccalauréat, Licée Franco Mexicain)	1991

## **Publications:**

J. A. Carretro González, “Estudio y diseño de un sistema de almacenamiento y recolección de piezas como parte de un sistema de manufactura flexible”, B. Eng. Thesis, Faculty of Engineering (UNAM), Mexico City, Mexico, 1996

J. A. Carretero, M. Nahon, C. M. Gosselin and B. Buckham, “Kinematic Analysis of a Three-DOF Parallel Mechanism for Telescope Applications”, In *Proceedings of the 1997 ASME Design Engineering Technical Conference*, Sacramento, California, USA

J. A. Carretero, R. P. Podhorodeski and M. Nahon, “Architecture optimization of a three dof parallel manipulator”, To appear in *Proceedings of the 1998 ASME Design Engineering Technical Conference*, Atlanta, Georgia, USA

J. A. Carretero, M. Nahon and R. P. Podhorodeski, “Workspace analysis of a three dof parallel manipulator”, To appear in *Proceedings of the 1998 IROS Conference*, Victoria, B.C., Canada

# Partial Copyright License

I hereby grant the right to lend my thesis to users of the University of Victoria Library, and to make single copies only for such users or in response to a request from the Library of any other university, or similar institution, on its behalf or for one of its users. I further agree that permission for extensive copying of this thesis for scholarly purposes may be granted by me or a member of the University designated by me. It is understood that copying or publication of this thesis for financial gain shall not be allowed without my written permission.

Title of Thesis:

Analysis of a three degree-of-freedom parallel mechanism

Author

Juan Antonio Carretero G.

August 12, 1998